Observation of double Gamow–Teller transition at high excitation energies by the (^{12}C, ^{12}Be(0^+_2)) reaction at 250 MeV/nucleon

by

Akane Sakaue

ABSTRACT

Double Gamow–Teller giant resonance (DGT giant resonance, DGTGR) is a novel mode of the nuclear excitation in which both the spin and isospin are flipped twice. The existence of the DGTGR has not been experimentally established since the first prediction in 1989. The observation of the DGTGR will open up the study of the two-phonon excitation in the domain of the spin-degrees of freedom are involved. In addition, the observation of the DGTGR is important as it will provide information about the nuclear matrix element of neutrino-less double β decay.

We employed the double charge exchange reaction of (^{12}C, ^{12}Be(0^+_2)) to explore the high-excitation energy region where the DGTGR is expected to lie. ^{12}Be(0^+_2) is an isomeric state which decays into the ground state by emitting an e^+e^- pair with the lifetime of 330 ns. This feature enables clear identification of the final state.

We performed the experiment using the (^{12}C, ^{12}Be(0^+_2)) reaction at 250 MeV/nucleon at Radioactive Isotope Beam Factory (RIBF) at RIKEN for ^{48}Ca target. In this experiment, the upstream part of an in-flight fragment separator of BigRIPS, from F0 to F5 focal plane, was used to analyze the momentum of the ejected particles. The following part from F5 focal plane to F8 focal plane was used for the separation of background particles and the detection of the γ-ray deriving from ^{12}Be(0^+_2) by NaI(Tl) scintillator array of DALI2. We obtained the double differential cross sections in 0°–1.9° with the energy resolution of 1.5 MeV. Forward peaking components were observed around 20 MeV and 35 MeV. The enhancement around 35 MeV might be attributed to other transitions than the DGT considering the expectation from the shell model calculation or the superposition of the single giant resonances. The enhancement around 20 MeV is likely to be attributed to the DGTGR. The integrated cross section over 0–34 MeV is 1.33 ± 0.12 μb/sr at 0°.

In order to quantitatively evaluate the contribution of the DGT, the multipole decomposition analysis was performed. The expected angular distributions were calculated by the distorted-wave Born approximation. The cross section of the extracted components whose angular distribution is analogous to the DGT transition is $0.50^{+0.35}_{-0.11}$ μb/sr at 0°. The excitation energy distribution of the DGT strength was deduced from the extracted cross sections. We obtained the following values from the deduced distribution in 0–34 MeV, the centroid energy as 23 ± 3 MeV, the width as 6 ± 1 MeV, and the sum of the strength as 28^{+22}_{-7} which is 22% of the sum rule value. This study demonstrated the possibility of the quantitative examination of the DGTGR by using the (^{12}C, ^{12}Be(0^+_2)) reaction.

Contents

List of Figures

List of Tables

Chapter 1

Introduction

1.1 Collective excitation in nucleus

An emergence of collective behaviors is an universal phenomenon in many body systems. Understanding its formation mechanism and extraction of general features are one of the essential topics in physics. Characteristics of the collective modes often reflect the bulk properties of the system, and information on interactions between its constituents can be extracted from microscopic analyses of the collective modes.

An atomic nucleus is one of the quantum many body systems and consists of nucleons. Their collective mode emerges as a response to the perturbation by an external stimulation, which is called giant resonance (GR) [11]. The GRs are observed as a bump in the excitation energy distribution of the cross section. The observations of GRs have been performed by photonuclear excitation, alpha inelastic excitation, and charge exchange reaction, etc. Observation of GRs in wide range of nuclei except for very light nuclei indicate that the emergence of GRs is regarded as a general property of nuclei.

GRs are often interpreted as nuclear oscillations with specific quantum numbers, such as orbital angular momentum L, spin S, and isospin T which is accompanied with the neutron ($T = +1/2$) and proton ($T = -1/2$). In other words, they are oscillations in the coordinate, spin, and isospin spaces. Thus it is usual to classify them in terms of the change of quantum numbers in the transition. The oscillation amplitudes are small enough so they can be regarded as a harmonic oscillation, and an excitation of phonon.

The observables of GRs, such as their central energies, widths, and amplitudes, reflect bulk properties of nuclei. One example is the relation between the incompressibility and the central energy of the isoscalar giant monopole resonance [12]. The appearance of two-peak structure in the isoscalar giant monopole resonance, on the other hand, is attributed to the deformation of the nucleus [13].

Microscopically GRs are understood as a superposition of many particle-hole (p-h) excitations. In this description, GRs corresponds to a coherent excitation caused by resid-

ual interaction [14].

The significant aspect of GRs is that they exhaust their total strengths. The isovector giant dipole resonance (IVGDR) is known to exhaust almost all the strengths of the Thomas–Reiche–Kuhn (TRK) sum rule for wide range of nuclei. The exhaustion of sum rule value is also microscopically reproduced with the random phase approximation (RPA) model [15]. The exception is the case of Gamow–Teller giant resonance (GTGR) as described in the following section.

1.2 Gamow–Teller GR

Among the nuclear excitations, the simplest mode which is induced by the spin- and isospin-dependent interaction is Gamow–Teller (GT) transitions. The GT transition is a nuclear process such that both the spin and isospin are changed without changing the orbital angular momentum ($\Delta S = 1$, $\Delta T = 1$, and $\Delta L = 0$). It is characterized by the $\mathrm{GT}^{\pm}$ operator of $\boldsymbol{\sigma}\tau_{\pm}$ where $\boldsymbol{\sigma}$ and $\tau_{\pm}$ are the spin and the isospin raising (τ_{+}) or lowering (τ_{-}) operator, respectively.

GT transition of nucleus was first identified in β decay. The allowed β decay coupled with the axial vector current is GT transition, while the vector current induces Fermi transition which is characterized by $\tau_{\pm}$ operator. The β decay is limited to the transition between ground states of the parent nucleus and the low-lying states in the daughter nucleus. GT transitions are also known to show collective excitation modes, GT giant resonances (GTGRs), at high excitation energies. Their centroid energies typically lie at 10 MeV in the excitation energy, so the β decay can not populate it. GTGRs have been observed by charge exchange reactions such as (p, n) or $(^3\mathrm{He}, t)$. The targets ranging from ^{6}Li to ^{208}Pb have been studied. The angular distributions of the cross sections have a peak at 0° which is characteristic to the $\Delta L = 0$ transitions.

Their observables have been provided significant information about the spin-isospin properties of nuclei and the relevant interactions. The driving force of the GTGR is residual spin-isospin interaction including short-range repulsion. The effective interaction in the spin-isospin channels V_{eff} is described as a sum of the one-pion and one-rho-meson exchange interactions and the Landau-Migdal (LM) interactions [16, 17]. LM interactions is mainly attributed to the short-range repulsion, and its strength g' is decomposed to g'_{NN}, $g'_{\mathrm{N}\Delta}$, and $g'_{\Delta\Delta}$ depending on its microscopic origins. These quantities have attracted interest of nuclear physicists because of its close connection to pion condensation which is expected to occur in a high density matter such as the interior of a neutron star. g' determines the susceptibility of the nuclear matter to the pion condensation [16]. The centroid energy of GTGR is correlated to the g' [18]. The extraction of g' is experimentally performed [19, 20, 21].

One of the remarkable features of GT transitions is the quenching of their transition

strengths from the model-independent sum rule. The sum rule known as Ikeda's sum rule is defined for GT transitions [22, 23]:

$$S(\sigma\tau_-) - S(\sigma\tau_+) = 3(N - Z) \tag{1.1}$$

where $S(\sigma\tau_\pm) = \sum B(\mathrm{GT}^\pm)$ is the GT transition strength $B(\mathrm{GT}^\pm)$ summed over the whole excitation energy in the final nucleus. On the other hand, $B(\mathrm{GT})$ is experimentally deduced as it is related to 0° cross section [24],

$$\frac{d\sigma}{d\Omega}(0^\circ) = \hat{\sigma}_{\mathrm{GT}} F(q,\omega) B(\mathrm{GT}), \tag{1.2}$$

where $\hat{\sigma}_{\mathrm{GT}}$ is the normalization factor of so-called "unit cross section" of GT transition. $F(q,\omega)$ describes the dependences on momentum q and energy ω transfers. $F(q,\omega)$ is defined to be unity at $(q,\omega) = (0,0)$. In the GTGRs, the observed strengths are only $\sim 60\%$ of the total strengths of the model-independent sum rule [25]. After a long debate, now it is understood to be due partly to excitations to p-h configurations beyond the model space, such as 2p-2h, and partly to excitations of non-nucleonic degrees of freedom, Δ [26, 27].

Charge exchange reactions using heavier nuclei are also used to excite GTGRs such as (^{7}Li, ^{7}Be) [28] or (^{12}N, ^{12}C) [29]. The advantage of the heavy-ion probe is the selectivity of the spin state [30].

1.3 Multi-phonon states in nuclei

From the phonon-excitation viewpoint of GRs, it is possible to extend the concept to include excitations of multiple phonon states. The two-phonon state corresponds to a GR state built on top of another GR [31]. The simple picture of multi-phonon states is based on the idea that each phonon behaves independently and the system is approximated to a harmonic oscillator. This approximation is closely related to the Brink–Axel hypothesis [32, 33] which claims that the properties of GRs such as the strengths or the relative energies are not affected by the detailed structure of the initial state but are determined by the bulk properties of the system.

Among the multi-phonon states, double GR states had been observed through the experimental studies at the Los Alamos Meson Physics Facility (LAMPF) using the double charge exchange (DCX) (π^+, π^-) and (π^-, π^+) reactions. Giant dipole resonance (GDR) built on isobaric analogue state (IAS) are observed in ^{56}Fe, ^{80}Se, and ^{208}Pb [34]. Consequently double isovector giant resonance were observed on ^{32}S [35] and ^{13}C, ^{27}Al, ^{59}Co, ^{40}Ca, and ^{93}Nb [1]. Figure 1.1 shows the excitation energy spectra obtained in the ^{93}Nb(π^+,π^-) reaction. Double IAS (DIAS), giant dipole resonance built on IAS (GDR⊗IAS), and double GDR (GDR⊗GDR) are observed. From the observations, it is natural to expect that the double giant resonances are also the general features of nuclei as well as the single giant resonances.

The energies of the two-phonon states observed in these studies were found to be approximately equal to the sum of the energies of two constituting phonons, while their widths are close to the quadratic sum of the individual widths [36, 31]. It supports the harmonic picture in which the individual phonons behave independently. However, the measured cross sections for double GDRs are considerably larger than those expected in the harmonic picture [37, 38]. The various theoretical interpretations of the anharmonicity exist such as phonon-phonon coupling or other second-order effects. They give an enhancement of the cross section in agreement with the observed ones, the conclusive origin is not clear due to the uncertainty in both the experimental data and the calculations [11].

Further information on harmonicity will be extracted from the three-phonon states The experimental study of three-phonon state in ^{40}Ca was performed with ^{40}Ca + ^{40}Ca reaction at 50 MeV/nucleon [39]. The further experimental information will be needed to conclude the harmonicity.

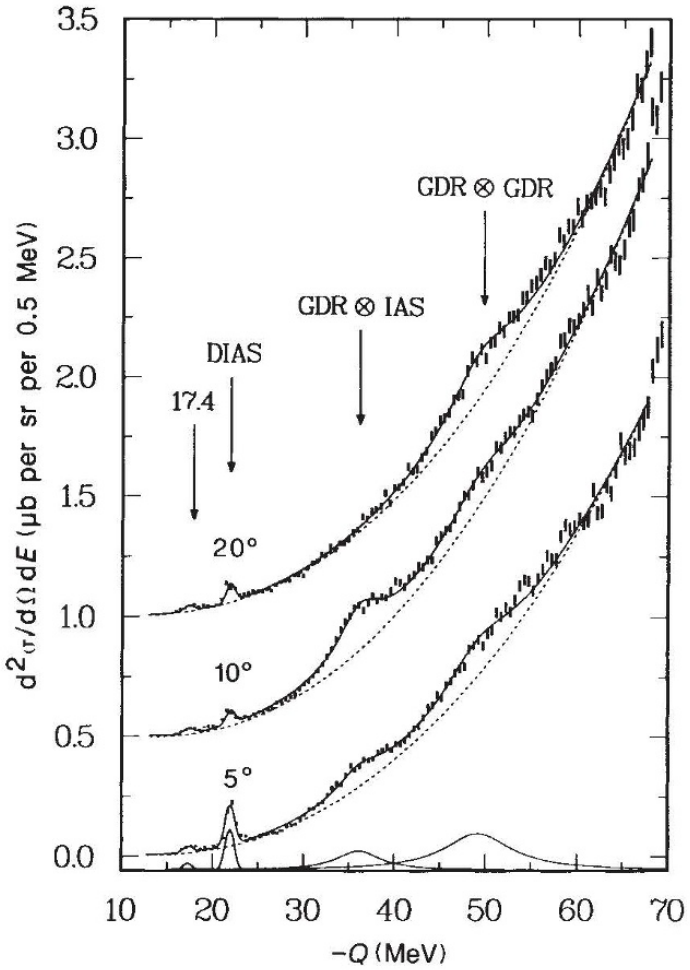

Figure 1.1: Double differential cross section for the (π^+, π^-) reaction on ^{93}Nb target at T_π = 295 MeV and $\theta_{\rm lab}$ = 5°, 10°, and 20° [1].

1.4 Double Gamow–Teller giant resonances

The experimentally established double giant resonances described above are currently limited to the non-spin related mode, $\Delta S = 0$. It is not obvious whether the harmonic picture hold or not in the giant resonances in spin-related modes, which is the oscillation in such a purely quantum mechanical coordinate of spin. Among the expected spin-related two-phonon states, double Gamow–Teller GR (double GTGR, DGTGR) is important for the general understanding of the nuclear collective excitations. It is a GTGR built on another GTGR and is characterized by the double GT (DGT) operator of $(\sigma\tau_{\pm})^2$. The existence of the DGTGR was first proposed in 1989 by Auerbach, Zamick, and Zheng [40]. Even after 30 years since the theoretical proposal, the DGTGR has not yet been observed successfully. The experimental observation can open a way to examine the harmonic picture in the domain of the spin-degree of freedom. It is interesting to examine whether the driving force of the GTGR, which contains the short-range repulsive force, behaves like a restoring force of an oscillator when the system is viewed macroscopically. The harmonic picture is not obvious also from the microscopic viewpoint, as the GT operator excites a larger number of states than non-spin operators and it would affects the formation of the collective mode. The inspection of the harmonicity would help the understanding the microscopic interaction and its formation of the collectivity.

Figure 1.2 shows the schematic diagram of the DGT transition in an example of ^{48}Ca as an initial state. The vertical axis expresses the excitation energy. The DGT transition is analogue to the double β decay similarly the correspondence of the single GT transition to β decay. Currently, the experimental information of the DGT transition is limited only to the double β decay data which occupies quite a tiny fraction of the total strength. Not only DGTGR, but any DGT transitions at higher than several MeV is essentially unknown experimentally. It is important to obtain the whole DGT response over the excitation energy region of from 0 to more than twice of a single GTR energy. Especially, it is interesting to see how the quenching of the transition strengths, observed in single GT transitions, emerges in the two-step process. The main component of DGTGR is expected to be a two successive GTGR transition formed by 1p-1h excitation in each step. It is natural to raise a question of whether the escaped components in the first step, that is, 2p-2h excitation or Δ-h excitation, come back in the second step or not. These various excitations including non-nucleonic degree of freedom should be involved in the DGT process, and DGTGR would emerge as a resultant of these interactions. The experimental information of how the DGT strengths are distributed in the final nucleus will the hint of this question.

DGTGR has been attracted interest of nuclear physicists as it has a close relation to neutrino-less double β decay ($0\nu\beta\beta$). The shell model calculations by Shimizu *et al.* [8] predict that the centroid energy and the width of the DGTGR are correlated with the nuclear matrix element (NME) of $0\nu\beta\beta$. The correlation arises through the paring interactions which both the centroid energy and NME are sensitive to. In a case of ^{48}Ca, the linear correlation between the centroid energy of DGTGR and the NME is demonstrated.

More generally, the correlation between DGT transition strengths and NMEs for nuclei with wide range of mass is pointed out. It opens a possibility of constraining the NME using the observed strength distribution of the DGTGR.

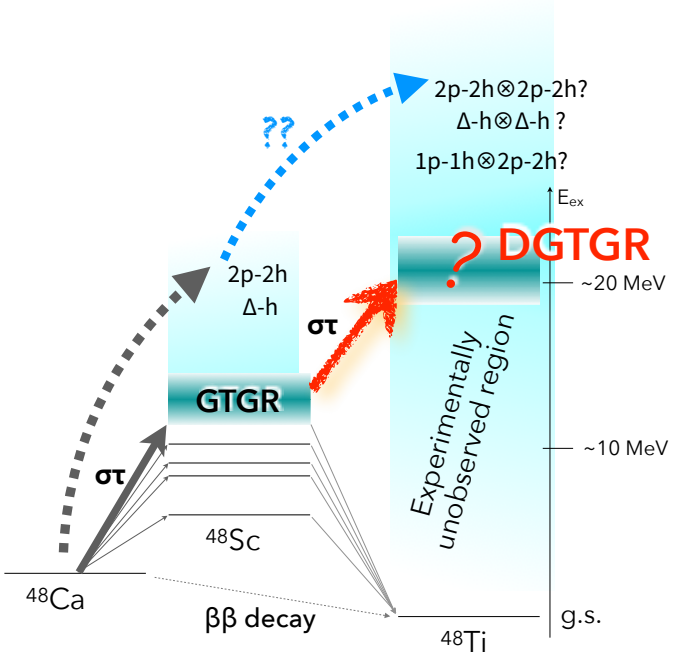

Figure 1.2: Schematic diagram of DGTGR in an example of the initial state as ^{48}Ca.

1.5 Previous experiments for observation of DGTGR

There are some conditions necessary to excite the DGTGR efficiently. The first condition is that the probe should induce spin-flip transitions. The second is that the probe should induce GT$^-$ type transition in the $N > Z$ target to avoid hinderance by the Pauli blocking. The third is that the incident energy should be $\gtrsim 100$ MeV/nucleon so that the direct reaction is dominant [26] and the reaction theories are safely applicable in the reaction analyses. This energy also enhances the ratio of spin-flip to non-spin-flip interaction strength $V_{\sigma\tau}/V_{\tau}$ in the effective nucleon-nucleon interaction [41, 26]. They have not simultaneously been fulfilled in previous studies as described in this section. This is the reason why the DGTGR remains unobserved so far.

Previously the ^{24}Mg(^{18}O, ^{18}Ne)^{24}Ne reaction in which the transition in the target is GT$^+$ type was measured at 100 and 76 MeV/nucleon at NSCL-MSU and GANIL, respectively [42]. There no particular structure was seen in the spectra. The extracted differential cross section was a few nb/sr at these energies. This is probably due to the small collectivity in the $N = Z$ target of ^{24}Mg.

The NUMEN project at INFN-LNS [43] adopts the same probe at 15 MeV/nucleon,

in which the contribution from other competing processes such as multi-nucleon transfer is crucial in this energy domain [44, 45, 46]. Their project includes the determination of such contributions and demonstrated their scheme with the transition between $^{40}\mathrm{Ca}_{\mathrm{g.s.}}$ and $^{40}\mathrm{Ar}_{\mathrm{g.s.}}$. Very recently the measurement on ^{132}Sn target which is the daughter nucleus of double β decay of ^{116}Cd has been reported [47]. They measured the excitation energy distribution of the cross section up to 25 MeV and determined the integrated cross section in the $^{116}\mathrm{Sn}_{\mathrm{g.s.}} \rightarrow {}^{116}\mathrm{Cd}_{\mathrm{g.s.}}$ region as 34^{+10}_{-25} nb by 95% confidence level. They claim that this results constrain the reaction mechanism.

The only case where all the three requirements are fulfilled, except for the slightly lower incident energy than 100 MeV/nucleon, is the (^{11}B, ^{11}Li) measurements at 70 MeV/nucleon at RCNP, but no clear conclusion on the existence of DGTGR was obtained due to the small yield [48].

1.6 The double charge exchange reaction of (^{12}C, ^{12}Be(0^+_2))

In this work, we employ the (^{12}C, ^{12}Be(0^+_2)) reaction at 250 MeV/nucleon. This reaction utilizes an isomeric state of ^{12}Be (excitation energy $E_{\mathrm{ex}} = 2.251$ MeV), as shown in the level diagram in Fig. 1.3. This reaction satisfies all of the three requirements listed above by virtue of the features of $^{12}\mathrm{Be}(0^+_2)$.

First, the transition $^{12}\mathrm{C}_{\mathrm{g.s.}} \rightarrow {}^{12}\mathrm{Be}(0^+_2)$ is regarded as a double spin-flip transition since the non-spin-flip strengths with $^{12}\mathrm{Be}(0^+_2)$ as the final state are exhausted by the transition with its double isobaric analogue partner, namely the $T = 2$ $^{12}\mathrm{C}(0^+)$ state at 29.630 MeV [49, 50]. The transition from the initial state of ^{12}C(g.s., 0^+) to the final state of $^{12}\mathrm{Be}(0^+_2)$ proceeds mainly through the intermediate of ^{12}B(g.s., 1^+). Since the total spin parity of the probe undergoes the transition of $0^+ \rightarrow 1^+ \rightarrow 0^+$, the target with the total spin 0^+ also follows the transition of $0^+ \rightarrow 1^+ \rightarrow 0^+$ with spin-flip in each step when the transfer of the orbital angular momentum is 0. Whereas the DGT operator acting on an initial 0^+ nucleus is capable of exciting 0^+ and 2^+ of final states, the transition to 0^+ states is emphasized by using this probe.

Another feature of $^{12}\mathrm{Be}(0^+_2)$ is a larger p-shell component in the wave function than the ground state [51, 52, 53, 54], which is manifested in the GT transition strength B(GT) with the value of 0.214 ± 0.051 in the transition from ^{12}B(g.s., 1^+) to $^{12}\mathrm{Be}(0^+_2)$, while 0.184 ± 0.007 in the transition to $^{12}\mathrm{Be}(\mathrm{g.s.}, 0^+_1)$. This originates from the well-known lowering of the $1s$ orbit in the neutron-rich light nuclei [55, 56]. Consequently, we can expect relatively strong double GT$^+$ transitions in the $^{12}\mathrm{C}_{\mathrm{g.s.}} \rightarrow {}^{12}\mathrm{B}(1^+) \rightarrow {}^{12}\mathrm{Be}(0^+_2)$ process which, in turn, can be used to induce double GT$^-$ transition in the target.

From the experimental perspective, this reaction has a prominent advantage of the capability of the clear reaction channel identification by measuring γ-rays deriving from the $^{12}\mathrm{Be}(0^+_2)$. The 0^+_2 state in ^{12}Be decays into the ground state by emitting an e^+e^- pair

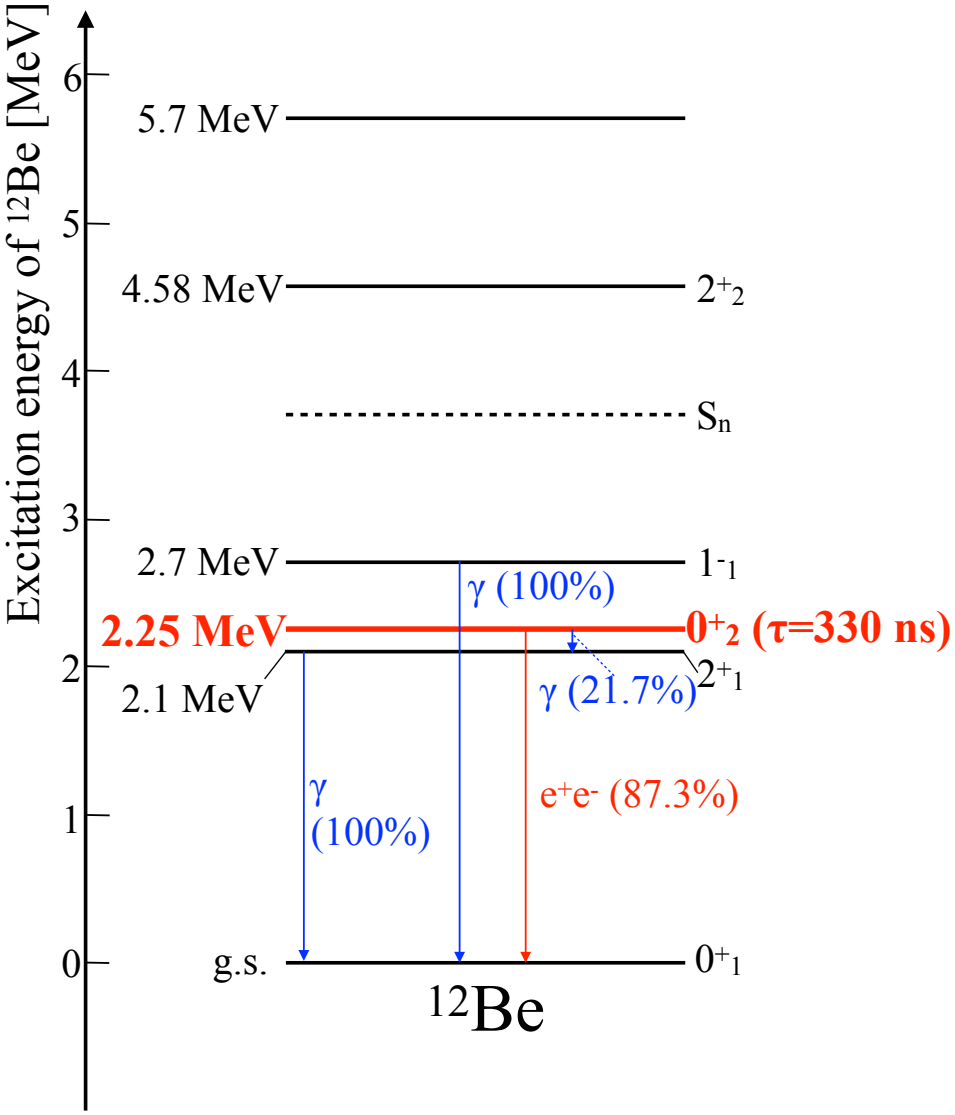

Figure 1.3: The level scheme and decay scheme of excited states of ^{12}Be.

with a lifetime of 330 ns [57, 58]. The back-to-back γ-rays from the annihilation of e^+ are emitted with accompanied by the decay of ^{12}Be(0^+_2). In addition, the long lifetime allows one to detect the delayed γ-rays far downstream from the target with smaller γ-rays background.

1.6.1 ^{12}C(^{18}O, ^{18}Ne)^{12}Be reaction experiment

The effectiveness of the probe is supported by a result of a double charge exchange study with the ^{12}C(^{18}O, ^{18}Ne)^{12}Be reaction [2]. The experiment was performed at Research Center for Nuclear Physics, RCNP, using 80 MeV/nucleon ^{18}O beam. Figure 1.4 shows the excitation energy spectra on ^{9}Be and ^{12}C. The peak of the spectrum of ^{12}Be around

2.2 MeV is mainly attributed to 0^+_2 state with 2.3 MeV. It shows that cross section of the transition to 0^+_2 state is larger than to the ground state, and thus it suggests that the transition from ^{12}C to ^{12}Be(0^+_2) is stronger than to ^{12}Be$_{\text{g.s.}}$. This results support the assumption that the DGT transition in this probe is strong.

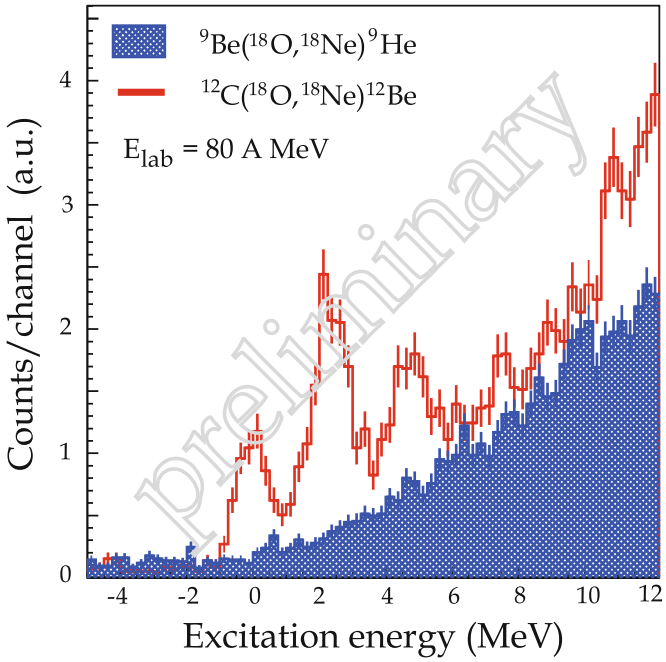

Figure 1.4: Excitation energy spectra of ^{9}He and ^{12}Be for the (^{18}O, ^{18}Ne) reaction at 0° on ^{9}Be and ^{12}C, respectively [2].

1.7 Interesting nuclei as a target of DGTGR

In the context of providing information to $0\nu\beta\beta$, the double β decaying nuclei are the candidates for the target. There are 11 double β decaying nuclei: ^{48}Ca, ^{76}Ge, ^{82}Se, ^{96}Zr, ^{100}Mo, ^{116}Cd, ^{128}Te, ^{130}Te, ^{136}Xe, ^{150}Nd, and ^{238}U.

In this thesis, we present the results of ^{48}Ca target. ^{48}Ca has the doubly closed shell with $Z = 20$ and $N = 28$, which enables the detailed nuclear structure studies. The *ab-initio* calculation with coupled-cluster theory is also progressively developed as represented by the result of a first-principles explanation of the quenching factor [59]. In addition, the single GTGR has been well investigated experimentally [60, 61], thus the comparison between the single and the double GR is possible. It enables to discuss the harmonicity quantitatively by using the observables of the single GTGR as the reference. In the context of providing the information to NME, ^{48}Ca is an important candidate of the experimental search of neutrino-less double β decay because it has the largest Q-value among the double β decaying nuclei [62]. The CANDLES project [63, 64] employs ^{48}Ca as a probe to take advantage of this feature.

1.8 Pilot experiment at RCNP using (^{12}C, ^{12}Be(0^+_2)) reaction

Takaki *et al.* performed a pilot experiment using the double charge exchange reaction of (^{12}C, ^{12}Be(0^+_2)) by employing the Grand Raiden spectrometer at RCNP in 2014 [65]. A 10-mg/cm^2 ^{48}Ca target was bombarded with a primary ^{12}C beam at 100 MeV/nucleon. An average intensity of the ^{12}C beam was 17 particle nA.

Outgoing particles were momentum-analyzed by the Grand Raiden spectrometer, and ^{12}Be was implanted in a plastic scintillator stopper with a thickness of 8.4 mm placed 1-m downstream of the focal plane of the spectrometer. The stopper was surrounded by a NaI(Tl) detector array for the detection of the γ-ray from the ^{12}Be(0^+_2) state. The array consisted of 42 NaI(Tl) detectors with the crystal size of $45 \times 80 \times 160$ mm^3 each. The photo-peak efficiency was about 10% including the geometrical acceptance.

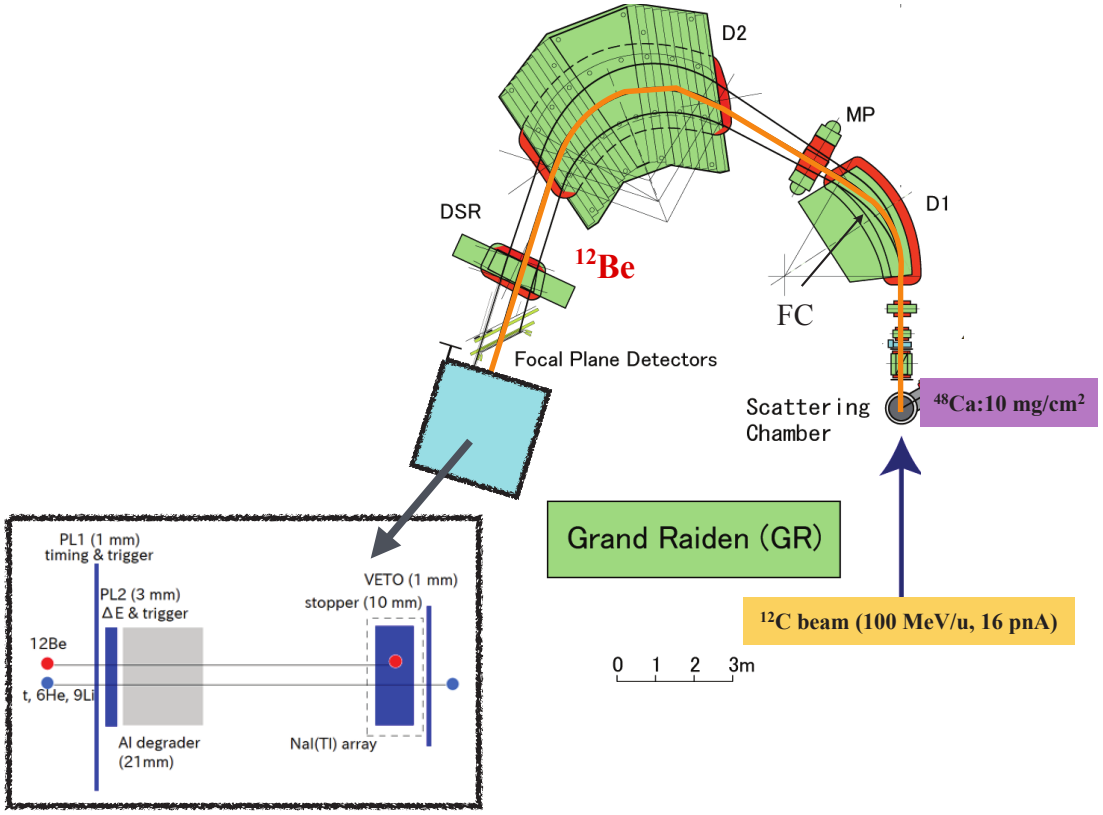

Figure 1.5: The outline of the setup of the experiment at RCNP.

Figure 1.6 shows the timing spectrum of the γ-ray detectors requiring the detection of two 511-keV γ-rays. The measured decay curve reproduces the lifetime of the ^{12}Be(0^+_2). There is a flat background component originating from β^+-decay of ^{11}C produced by nuclear reactions with light ions such as tritons off ^{12}C in the stopper. The signal-to-background ratio was 1:1.

The observed cross section has a peak at the most forward angle of 0-0.8° [65].

This may be attributed to the candidate for DGTGR. The integrated cross section in 22–30 MeV is 0.7 μb/sr.

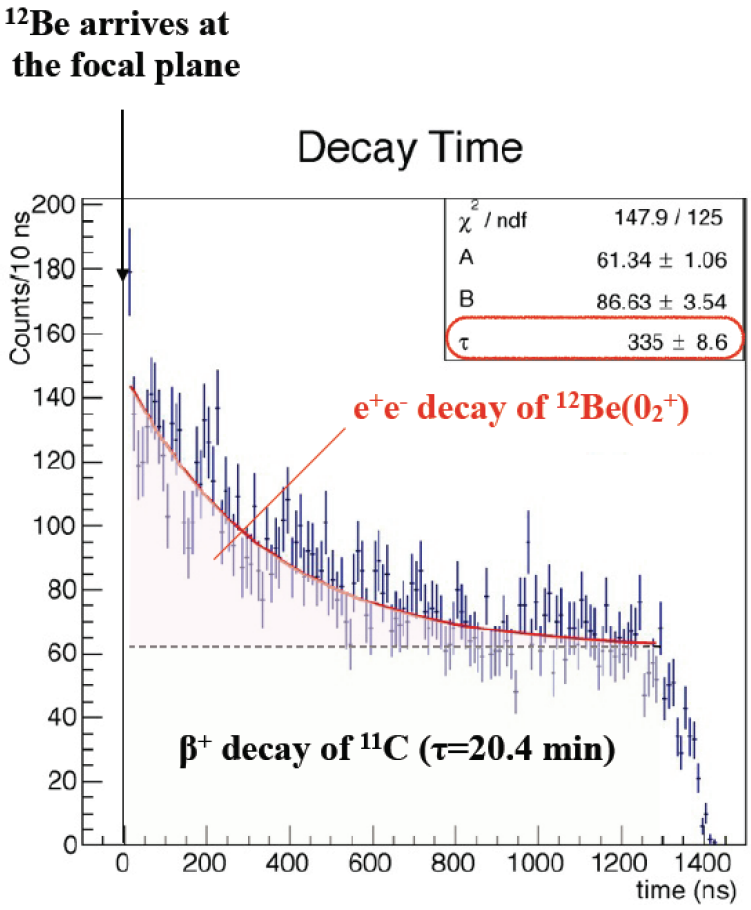

Figure 1.6: The timing of the γ-rays measured by the NaI scintillator array in the experiment of (^{12}C, ^{12}Be(0_2^+)) performed at RCNP [3].

1.9 Experiment at RIBF

Based on the experiment at RCNP, the implementation of the experiment at Radioactive Isotope Beam Factory (RIBF) [66] in RIKEN using the (^{12}C, ^{12}Be(0^+_2)) probe was planned. The intense ^{12}C beam provided from superconducting ring cyclotron (SRC) at up to 1 particle μA will improve the statistics. In general, the primary beam is utilized only for a production of RI beam at RIBF with the BigRIPS separator [67]. Recently, the spectroscopic experiment using a primary beam had been established in a pionic atoms spectroscopy experiment [6, 68]. In this experimental method, the BigRIPS is used as a spectrometer. It is applicable to double charge exchange measurement of (^{12}C, ^{12}Be(0^+_2)) in combination with the γ-ray detector array of DALI2 [69]. The details are described in Chapter. 2.

The merits and demerits in the experiment at RIBF compared with that at RCNP are as follows.

- Beam intensity

  The intensity of the ^{12}C primary beam at RIBF is several hundreds partcile nA. This amounts to more than 10 times than at RCNP. The maximum intensity at RIBF is determined by a radiation regulation so that the count rate at F3 should not exceed 10^7 Hz.

- Background rejection

  The cascade of magnets of BigRIPS serves as the background-rejection. It is expected to reduce the count of triton to the level that should not produce significant background.

- Background-free stopper

  In the experiment at RCNP, the stopper should be large enough to cover the dispersive focal plane. In the experiment at RIBF, the γ-ray detector can be settled at an achromatic focal plane downstream of a dispersive, momentum analyzing focal plane. This enlarges the choice of the stopper to a material which does not cause the production of a significant amount of β^+ emitters. Considering this along with the rate of the triton, the experiment at RIBF is free from the background γ-rays originating from the reaction at the stopper, and the main background is the accidental coincidence of room-background γ-rays and ^{12}Be.

- Efficiency of γ-ray detection

  The typical photo peak efficiency of DALI2 array for 511-keV γ-rays from ^{22}Na source is 30% [69], which is three times of that at RCNP.

- The survival ratio of ^{12}Be(0^+_2)

The Time-of-Flight from the reaction point (target place) to the γ-rays detector is 130 ns at RCNP while it is 500 ns at RIBF. Thus the survival ratio of ^{12}Be(0_2^+), the ratio of the number of the ejected ^{12}Be(0_2^+) at the target and the ^{12}Be(0_2^+) reached at the γ detector, is reduced to 25% at RIBF from 70% at RCNP.

In total, the expected yield of the true events in the experiment at RIBF is 10 times while the background events is reduced to 1/10 compared with that at RCNP.

1.10 Thesis objective

The present study is devoted to the establishment of the experimental observation of the highly excited double Gamow–Teller transition including the DGTGR. This leads to the examination of the harmonicity of DGTGR, and it provides an inspection of the natural extension of the quantum oscillation to the spin degree of freedom. In addition, the experimental data not only on the DGTGR, but whole DGT response in the wide region of excitation energy, will provide an insight on the fragmentation of the DGT strength.

In this work, the DGT transition from ^{48}Ca target was investigated using (^{12}C, ^{12}Be(0_2^+)) at 250 MeV/nucleon. In order to obtain the DGT response in high excitation energy region, the doubly differential cross sections and their angular distribution had been measured.

The measured data was compared to the calculated angular distribution to evaluate the contribution from DGT quantitatively. The DGT transition strength was obtained.

The author contributed all aspects of the preparation and conduction of the ^{48}Ca(^{12}C, ^{12}Be (0_2^+)) experiments, in particular development of ion-optics and its tuning, rejection of light ions using energy degraders and the magnetic system of F5–F7, designing the ^{12}Be stopper, and coordination of the experimental group consisting of ~50 members. The author carried out the data analyses and the reaction calculations, and led the writing the paper in close communication with the collaborator of the experiment and theory researchers.

This thesis covers the measurement of the cross section of ^{48}Ca(^{12}C, ^{12}Be(0_2^+)) and the discussion on the results. The experimental setup and conditions are described in Chapter 2. The data analysis and the results of the differential cross section are described in Chapter 3. The reaction calculation is described in Chapter 4. The multipole decomposition analysis using calculated distributions and discussion on the results are described in Chapter 5.

Chapter 2

Experiment

Our purpose is to obtain the excitation energy distribution of double-differential cross section in the double charge exchange (DCX) reaction of (^{12}C, ^{12}Be(0^+_2)) and its angular distributions. We present the results of the measurement for ^{48}Ca target. We performed the experiment at RIBF using BigRIPS.

2.1 Experimental scheme at RIBF

The overview of the facility of RIBF and BigRIPS, and the experimental scheme in the present study will be described in this section.

2.1.1 RIKEN RI Beam Factory and BigRIPS

RIBF is a cyclotron accelerator facility which provides high-intensity RI beams at kinetic energies around 200–300 MeV/nucleon. Figure 2.1 shows a bird's-eye view of the RIBF. The accelerator complex of the RIBF consists of three injectors (RILAC, RLLAC2, and AVF) and four ring cyclotrons (RRC, fRC, IRC, and SRC). The cyclotron complex is capable of accelerating heavy ions, ranging from (polarized) deuteron to ^{238}U, with the energy of more than 70% of the light speed. The available intensities extracted from SRC are a $\sim$ 100 pnA for ^{238}U and several hundreds pnA–1 pμA for light ions.

The primary beams provided from SRC are used for the production of RI beams by the projectile fragmentation or in-flight fission of heavy ions. They are separated by the in-flight superconducting fragment separator BigRIPS [67]. The BigRIPS consists of seven focal planes (F1–F7), six room-temperature dipole magnets (D1–D6), and fourteen superconducting triplet quadrupole magnets. The F3 and F7 focal planes are momentum achromatic planes while F1 and F5 foci are momentum dispersive planes. The BigRIPS is designed for an in-flight separation and identification of RI beams with a two-stage structure. The first stage from F0 to F2 serves as an RI separator while the second stage

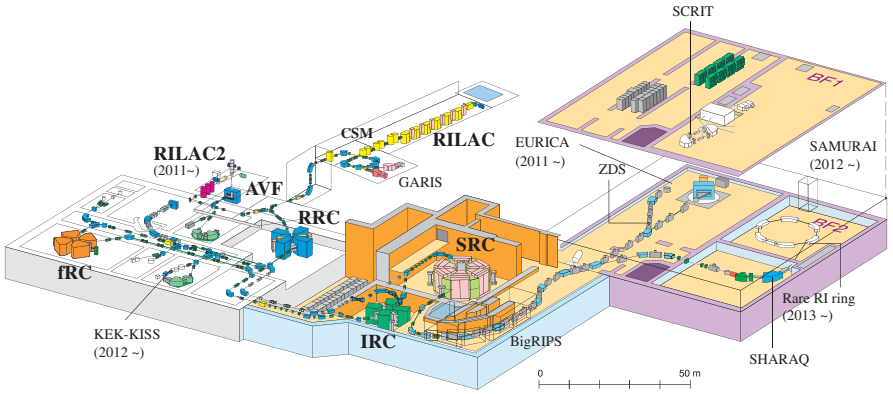

Figure 2.1: The bird's-eye view of RIKEN RIBF. This figure is taken from [4].

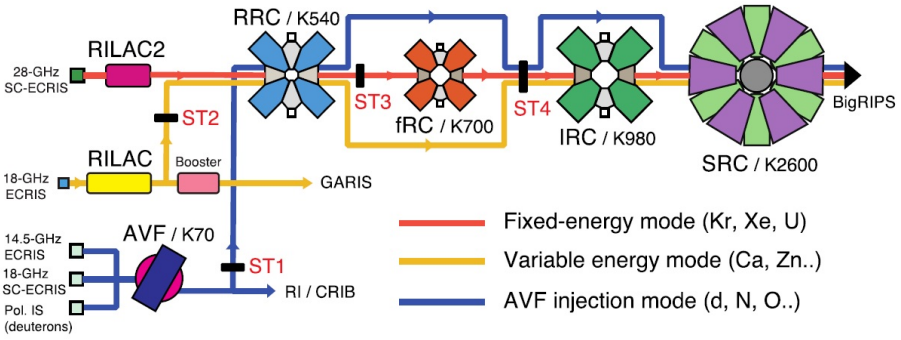

Figure 2.2: Beam acceleration mode in the RIBF. This figures is take from [5].

from F3 to F7 performs particle identification with TOF-$B\rho$-ΔE method [70].

In the downstream ends, various setups are installed according to the purpose of experiments.

2.1.2 Experimental overview

In the present study, the BigRIPS was used as a spectrometer based on the experimental concept in the pionic atoms spectroscopy [6, 68]. The experimental requirements in the present case of double charge exchange reaction measurement are as follows:

- The DGTGR is expected to lie around 20 MeV in the excitation energy in ^{48}Ti. The coverage range of energy should be as wide as 0–~40 MeV.
- Typical requirement for the energy resolution is ~2 MeV for the observation of single GTRs. 2 MeV is sufficient for the observation of the DGTGR because its width is expected to be larger than that of single resonances.
- In order to identify and extract $\Delta L = 0$ components from the observed cross sections, the forward peaking structure is to be identified. In order to decompose from

other ΔL components, the required angular resolution is 0.3° as discussed in the Sec. 4.4.

We optimized the experimental method to satisfy the requirements above. The concept of the experiment is depicted in Fig. 2.3. A primary beam of ^{12}C with a typical intensity of 600 pnA was accelerated by the Superconducting Ring Cyclotron (SRC) to 250 MeV/nucleon and impinged on the reaction target. The emitted ^{12}Be in the (^{12}C, ^{12}Be(0^+_2)) reaction is momentum-analyzed by a part of BigRIPS [67], F0–F5. ^{12}Be is transported to F8 with being decelerated by degraders. The isomeric state of ^{12}Be(0^+_2) is identified by detecting γ-rays using a NaI(Tl) scintillator array of DALI2 [69]. Other $A/Z = 3$ light ions such as t, ^{6}He, and ^{9}Li are removed by their energy loss difference and magnetic separation.

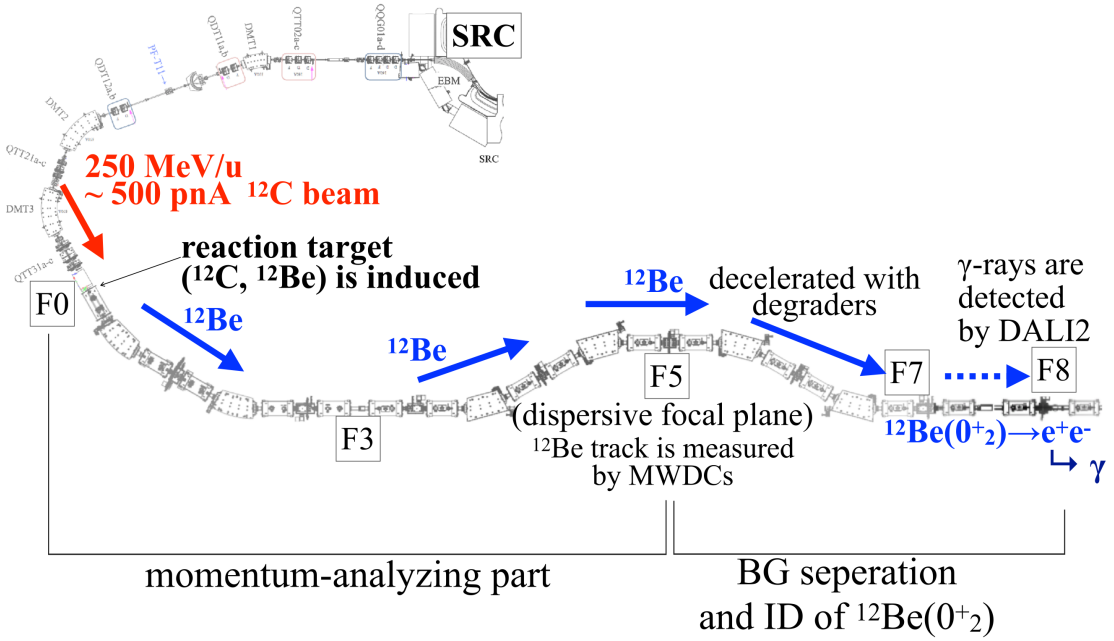

Figure 2.3: The concept of the present experiment is shown with the beam line of BigRIPS.

The typical momentum spread of the primary beam of ^{12}C is 0.08% (FWHM), which corresponds to the spread of the excitation energy of 4.2 MeV. In order to obtain sufficient energy resolution, a dispersion matching is adopted. The beam is made momentum-dispersed at F0 so that the energy spread of the beam is canceled out at F5.

In the following sections, the details of the setup and conditions will be described.

2.2 Properties of primary beam

A ^{12}C beam with the intensity of 600 pnA at maximum and the energy of 250 MeV/nucleon were used. The primary ^{12}C beam was accelerated by three accelerators: AVF, RRC, and SRC. The primary beam properties extracted from SRC are described in this section. The beam emittance and momentum spread are provided in Sec. 2.4.

2.2.1 Intensity and beam energy

The beam intensity was measured by using Faraday cups installed in the beam line between SRC and the target. The luminosity on the target was continuously monitored by counting the coincidence signals of back-scattered particles from the target with three scintillation counters installed in the upstream side of the target. The relation between triple coincidence rate and the beam intensity was obtained by measurements with changing the intensity. Figure 2.4 shows the beam intensity in the unit of electric current (enA) measured by Faraday cups against the triple coincidence rate at the successive measurements. The uncertainty of the intensity measured by Faraday cup is assumed to be 10%. The linear relation of (intensity) = $(0.076 \pm 0.003) \times$(coincidence rate) enA was obtained. During the DCX run, the average beam intensity was 3600 enA, which corresponds to 600 particle nA.

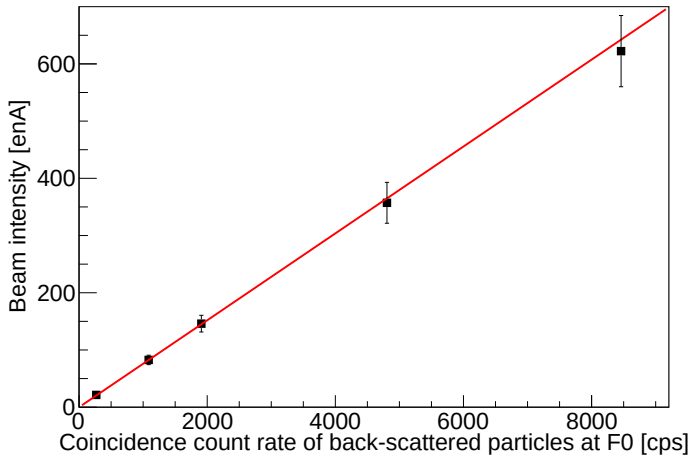

Figure 2.4: Relation between the count rate of the back-scattered particles at the target and beam intensity.

The beam energy was evaluated from the magnetic rigidity in a faint-beam measurement without target at F0. The magnetic rigidity was obtained from the field measured by Nuclear Magnetic Resonance probe (NMR) (EMA-1401R, Echo Electronics Co., Ltd.) in the D1 magnet and the central radius. The resolution of the NMR is $\pm 1 \mu$T. The beam energy was determined as 248.2 MeV/nucleon. The error of the evaluation is described in

Sec. 3.5.

2.3 Target

The targets used in the DCX reaction measurements are listed in Table 2.1.

A foil target of ^{48}Ca with an isotopic enrichment of 95.23% was used for the measurement of the DCX. Two foils of ^{48}Ca with thicknesses of 5 mg/cm^2 and 5.3 mg/cm^2 were layered to make the target with thickness of 10.3 mg/cm^2. The size of the foils are 1 cm $\times$ 1 cm. The foils are placed so that the diagonal lines would be along the horizontal line in order to make the horizontal (direction of dispersion) coverage large. The ^{48}Ca foil was sandwiched by 4-μm thick graphene sheets on both sides upstream and downstream. The graphene sheets were attached to dissipate the heat due to the high-intensity beam utilizing its large thermal conductivity. It also helped to prevent oxidation and nitridization of the target during the installation process. Figure 2.5 shows the ^{48}Ca foils and the graphene sheets during making the target.

Though the ^{116}Cd target was also used for the DCX measurement, the data are not dealt with in this thesis. The ^{8}Li was produced via the fragmentation of the ^{116}Cd target for the ion-optical study.

The DCX and single charge exchange (SCX) measurements were performed also with a graphene target. In the DCX, it is utilized for an estimation of the background events arising from the graphene coating on the ^{48}Ca target. In the SCX, it is used as a calibration.

Table 2.1: A list of targets in the experiment.

target	thickness	size	purpose
^{48}Ca	10.3 mg/cm^2	1 cm^2	DCX and SCX measurement
^{116}Cd	40 mg/cm^2	1 cm^2	DCX measurement and optics study
graphene	36 μm	1 cm^2	BG measurement for DCX and calibration in SCX

2.4 Beam transport

In this section, the beam transport when the BigRIPS is used as a spectrometer is described. The ion optics tuning in the experiment is also described.

2.4.1 Design of BigRIPS as a spectrometer

The optics to use BigRIPS as a spectrometer was first developed for the experiment of pionic atoms spectroscopy [6, 68, 71]. The design of BigRIPS as a spectrometer is summarized in Table 2.2. In this system, the F5 focal plane is dispersive when the F0 focal plane

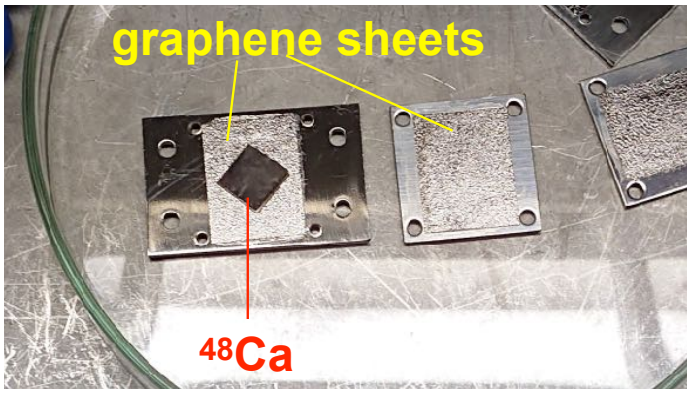

Figure 2.5: Photograph of the ^{48}Ca target. The attachment of the graphene sheets to the target was done inside of a glovebox filled with Ar gas.

is achromatic so that the momentum of particles is analyzed by the horizontal position at F5. The transfer matrices for the designed optics were calculated using GICOSY [72] as shown in Table 2.3 for F0–F5 and Table 2.4 for F0–F3 systems. Here x and y denote the horizontal and vertical positions, respectively, while a and b are the horizontal and vertical angles, respectively, and δ is relative momentum difference defined as $\delta = (p - p_c)/p_c$ where the p and p_c are the momentum of the transported particle and that of the central ray, respectively. The trajectory of a particle is described using matrix elements as $X_i = \sum_j (X_i|X_j) \cdot X_j$ on the first order, where $X_i = x,\ y,\ a,\ b$ and $X_j = x,\ y,\ a,\ b,\ \delta$.

Table 2.2: Design specifications of BigRIPS as a spectrometer [6].

Flight length (F0–F5)	54.916 m
Vertical magnification	−1.63
Horizontal magnification	−1.82
Momentum dispersion	62.0 mm/%
Momentum range	±2 %
Momentum resolution	3400
Acceptance angle-horizontal	±20 mrad
Acceptance angle-vertical	±40 mrad
Solid angle	3.2 msr

2.4.2 Dispersion matching tuning

The momentum spread of the primary beam is typically 0.08%, which is insufficient to achieve the required excitation energy resolution of 2 MeV for a ^{12}C beam with a total energy of 3 GeV. In order to avoid the deterioration of the energy resolution, dispersion matching optics [73] is applied. In a system consisting of a beam transport line and a spectrometer systems, the intrinsic momentum spread of the beam δp_{beam} contributes to

Table 2.3: Transfer matrix elements from F0 to F5.

$(x\|x)$	-1.817
$(x\|a)$	-1.13×10^{-4} m/rad
$(x\|\delta)$	62.0 mm/%
$(a\|x)$	0.182 rad/m
$(a\|a)$	-0.55
$(a\|\delta)$	-9.8×10^{-4} mrad/%
$(y\|y)$	-1.63
$(y\|b)$	-4.8×10^{-4} m/rad
$(b\|y)$	1.43 rad/m
$(b\|b)$	-0.61

Table 2.4: Transfer matrix elements from F0 to F3.

$(x\|x)$	-0.92
$(x\|a)$	6.38×10^{-6} m/rad
$(x\|\delta)$	-3.60×10^{-4} mm/%
$(a\|x)$	0.198 rad/m
$(a\|a)$	-1.09
$(a\|\delta)$	4.3×10^{-5} mrad/%
$(y\|y)$	-2.3
$(y\|b)$	-3.6×10^{-4} m/rad
$(b\|y)$	-0.64 rad/m
$(b\|b)$	-0.43

the positions at the dispersive focal plane x_{fp} as

$$x_{\mathrm{fp}} = (CS_{16} + S_{11}B_{16})\delta p_{\mathrm{beam}}, \tag{2.1}$$

where C is a kinematical factor of the reaction defined as $C = \partial P_{\mathrm{out}}/\partial P_{\mathrm{in}} \cdot P_{\mathrm{in}}/P_{\mathrm{out}}$ [73], where P_{in} and P_{out} are the momentum of the incoming to and outgoing from the reaction point, respectively. S_{11}, S_{16}, and B_{16} are the magnification and the dispersion of the spectrometer, and the dispersion of the beam line at the target, respectively. In the dispersion matching method, the S_{11}, S_{16}, and B_{16} are adjusted to realize the following condition,

$$CS_{16} + S_{11}B_{16} = 0, \tag{2.2}$$

so that the effect of the δp_{beam} vanishes.

The kinematical factor C for the DCX reaction of (^{12}C, ^{12}Be(0^+_2)) is 1.0. In the BigRIPS spectrometer, $S_{16} = (x|\delta)_{\mathrm{F0}\to\mathrm{F5}} = 62.0$ mm/% and $S_{11} = (x|x)_{\mathrm{F0}\to\mathrm{F5}} = -1.817$, so the matching condition is $B_{16} = 34$ mm/%. To fulfill the matching condition, the beam was made momentum-dispersed at F0 by tuning quadrupole magnets in the injection beamline from T11 (shown in Fig. 2.6) to F0, based on the design of the beam line

transport shown in Fig. 9 and Table 3 in Ref. [71]. One difficulty is that no tracking detector can be installed at F0, which prevent one from precise tuning. The beam diagnostic method was developed that we call "trace-back method" [74] to overcome the difficulty. In this method, the beam trajectory at F0, where no tracking detector can be installed, is reconstructed from the trajectories at F3, F7 (achromatic foci) and F5 (dispersive focus). The information on x and a was obtained from the transfer matrix of F0–F3 while δ was obtained from that of F5–F7.

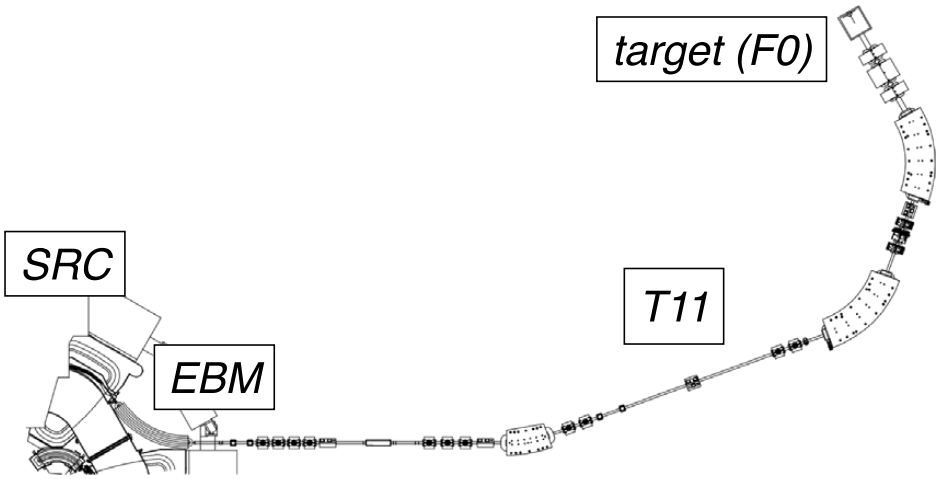

Figure 2.6: Schematic view of the beam line from SRC to target (F0). This is taken from Ref. [6].

2.4.3 Beam properties after the dispersion matching

The properties of the primary beam after the dispersion-matching tuning were measured by transporting the beam with a faint intensity to F7. The momentum spread was estimated from the distribution at F5, and the beam spot image at F0 was reconstructed from the trajectories at F3. Figure 2.7 shows the position spread of the primary beam at F5 after the dispersion matching tuning. The position spread at F5 was determined to be 1.7 mm (FWHM), which corresponds to a momentum spread of 0.026% and to an energy spread of 1.4 MeV. Figure 2.8 shows the comparison of the beam spread before (blue line) and after (red line) the dispersion matching. It should be noted that the shoulder structures on the left side of peaks are due to detectors placed at F3. The beam spread at F5 before the tuning was evaluated as 5 mm (FWHM), which corresponds to a momentum spread of 0.078% and an energy spread of 4.1 MeV. The dispersion matching tuning effectively suppressed the effect of the beam momentum spread by a factor of 3, leading to the energy resolution required in the present experiment.

The beam spot size and angular spread at F0 were evaluated from the trajectories at F3 using calculated values of the transfer matrix element from F0 to F3. The first-order terms of the description of the transport matrices were used as follows: $\mathrm{F3}x = (x|x)_{\mathrm{F0}\to\mathrm{F3}} \cdot \mathrm{F0}x$,

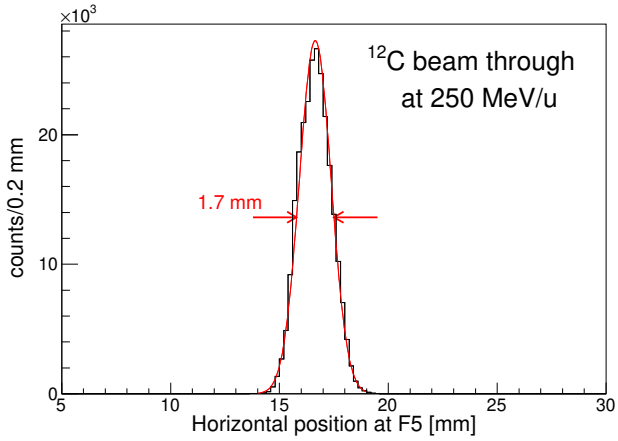

Figure 2.7: Position spread of the beam in the horizontal direction measured at F5, which corresponds to the beam energy spread.

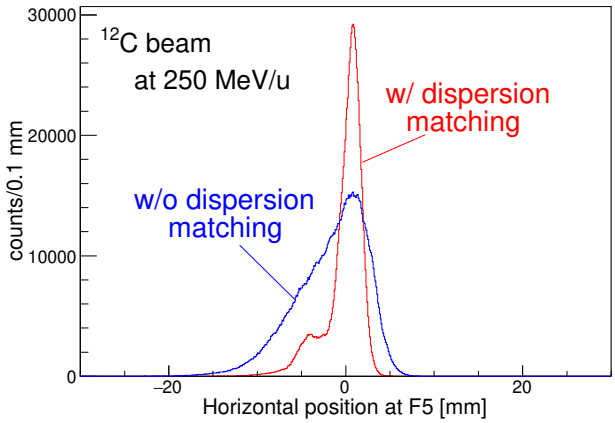

Figure 2.8: Position spread of the beam in the horizontal direction measured at F5, with dispersion matching (red) and without dispersion matching (blue).

F3y = $(y|y)_{\mathrm{F0}\to\mathrm{F3}} \cdot$ F0y, F3a = $(a|a)_{\mathrm{F0}\to\mathrm{F3}} \cdot$ F0a, and F3b = $(b|b)_{\mathrm{F0}\to\mathrm{F3}} \cdot$ F0b. Thus the image at F0 was obtained as F0x =F3$x/(x|x)_{\mathrm{F0}\to\mathrm{F3}}$, F0$y$ =F3$y/(y|y)_{\mathrm{F0}\to\mathrm{F3}}$, F0$a$ =F3$a/(a|a)_{\mathrm{F0}\to\mathrm{F3}}$, and F0$b$ =F3$b/(b|b)_{\mathrm{F0}\to\mathrm{F3}}$. The obtained images at F0 are shown in Fig. 2.9. The spatial spreads of the beam was evaluated as 5 mm(horizontal)×5 mm(vertical). The angular spreads were $\Delta\theta_{\mathrm{lab}} = 0.15°$ (in σ) in horizontal and $\Delta\theta_{\mathrm{lab}} = 0.16°$ (in σ) in vertical. The small angular spread is essential for the extraction of the DGT components, as described in Sec. 4.4. The present angular spread fulfill the requirement since they correspond to those in center of mass frame $\Delta\theta_{\mathrm{CM}} = 0.20°$ (in σ) in horizontal and $\Delta\theta_{\mathrm{CM}} = 0.22°$ (in σ) in vertical.

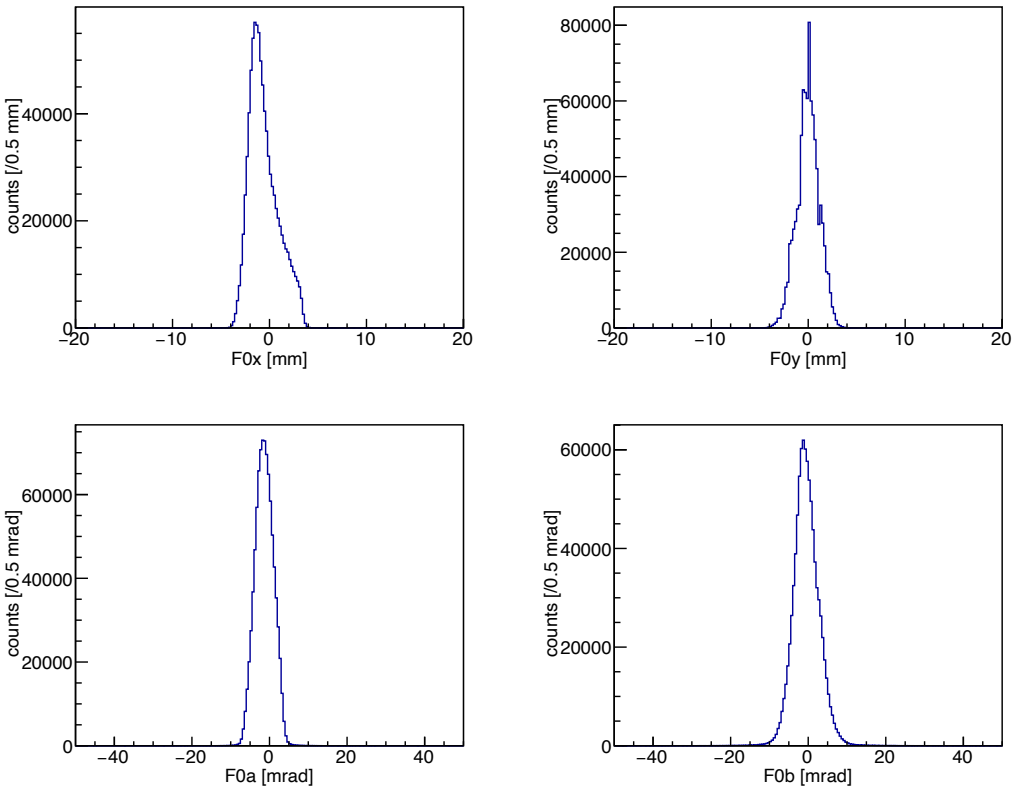

Figure 2.9: Measured beam images at F0 reconstructed from the trajectories at F3.

2.5 Detectors and materials installed in the beam line

The detectors and the materials installed in the beam line are described in this section. The schematic view of the configuration is shown in Fig. 2.10.

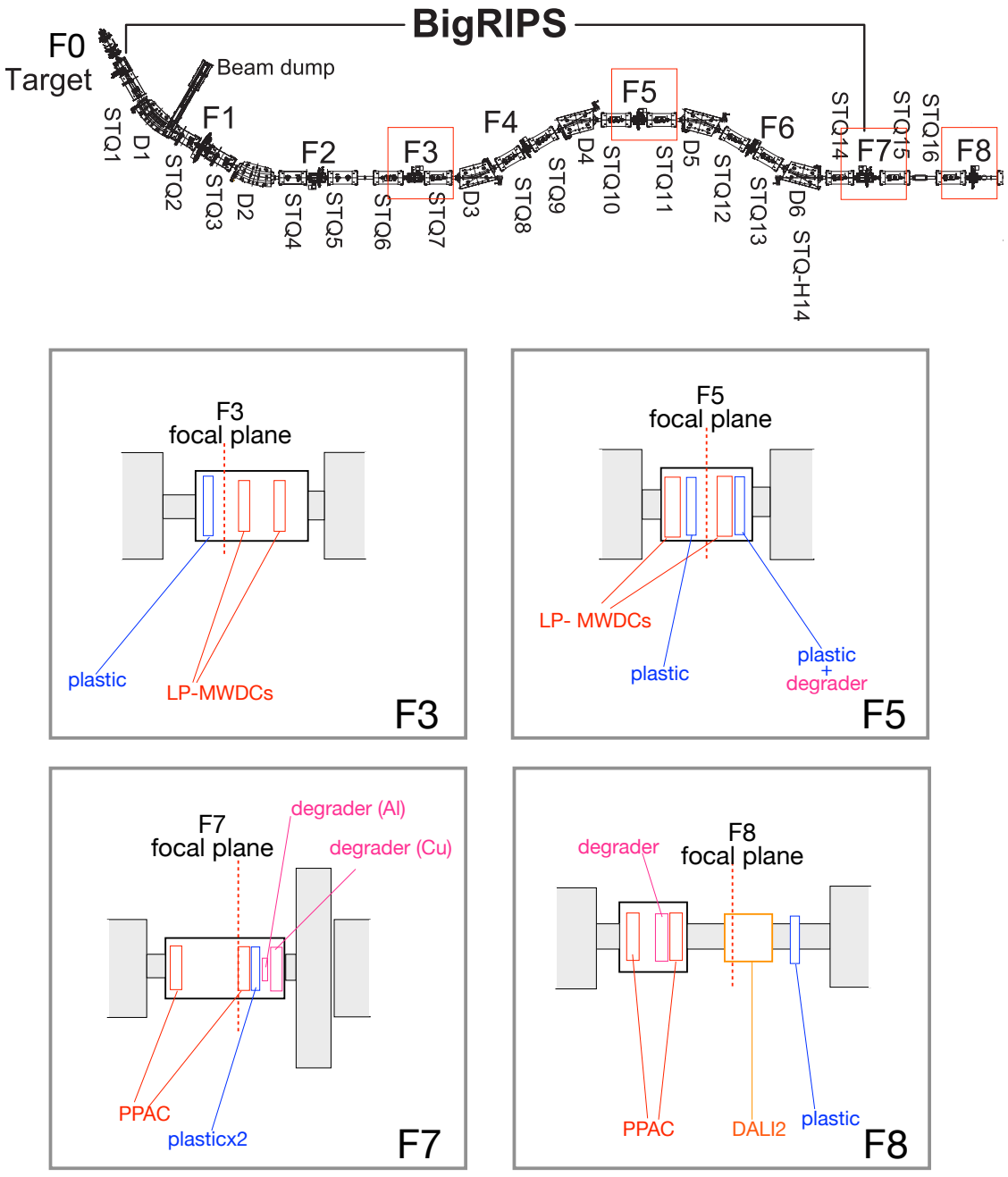

Figure 2.10: Configuration of the beam line detectors and degraders at each focal plane. White filled boxes with black lines express the vacuum chamber. Beam goes from left to right in the figure. Vertical broken red liens denotes the standard focal plane.

2.5.1 Low-pressure multi-wire drift chambers

The two sets of low-pressure multi-wire drift chambers (lp-MWDCs) [75] were installed at F3 and F5. MWDCs at F3 were used for the tuning of the measurement of the beam profiling, and were out of the beam line during the DCX run. MWDCs at F5 were used for the measurement of the track of ^{12}Be ejected in the DCX reaction as well as the study and the tuning of the beam line optics.

MWDCs at F3

At F3, the two sets of lp-MWDCs were placed at an interval of 460 mm. XX'YY'XX'Y Y' for the upstream and XX'YY' for the downstream with the cell sizes of 3 mm (upstream) and 5 mm (downstream). The prime indicates that the wire positions are displaced by half-cell size. The lp-MWDCs were installed into a vacuum chamber and were operated with 50 kPa Isobutane gas. 1200 V (upstream) and 1250 V (downstream). In X plane wires are set vertically and in Y planes wires are set horizontally. The prime means the wire positions are displaced by half-cell size. Effective area is 100×100 mm^2.The lp-MWDCs were installed into vacuum chamber and were operated with 50 kPa isobutane gas. The plane resolution was 300 μm.

MWDCs at F5

At F5, the two sets of lp-MWDCs were placed at an interval of 633 mm. The two sets of lp-MWDCs have the same configuration. These lp-MWDCs were constructed for use as the focal-plane detectors of the present experiment [76]. The specification of the lp-MWDCs is shown in Table. 2.5. The configuration is on the basis of those in Ref. [75]. One modification introduced for this experiment is the wire structure of X-X'-X", U-U'-U", and V-V'-V" with the wire displacement by 1/3-cell pitch (1/3-cell staggered MWDCs). The schematic view of the configuration of the planes is shown in Fig. 2.11. This is to reduce influence of microstructures on the tracking efficiencies, we used the other type of MWDCs than F3. This DGTGR experiment was the first practical use of these MWDCs. The operational test was performed at Cyclotron and Radioisotope Center (CYRIC) in Tohoku university [76] in 2017 and at Tandem Accelerator Complex in Tsukuba University (UTTAC) [77] in 2020.

2.5.2 Plastic scintillation counters

Plastic scintillation counters were installed at F3, F5, F7 and F8. The counter at F3 was used to count the rate of ^{3}He which was regulated to be under 10^7 cps for radiation safety. It was out of the beam line during the DCX run. The counter at F5 was installed originally for making the time reference of the MWDCs at F5, but the right side of F5 PMT was

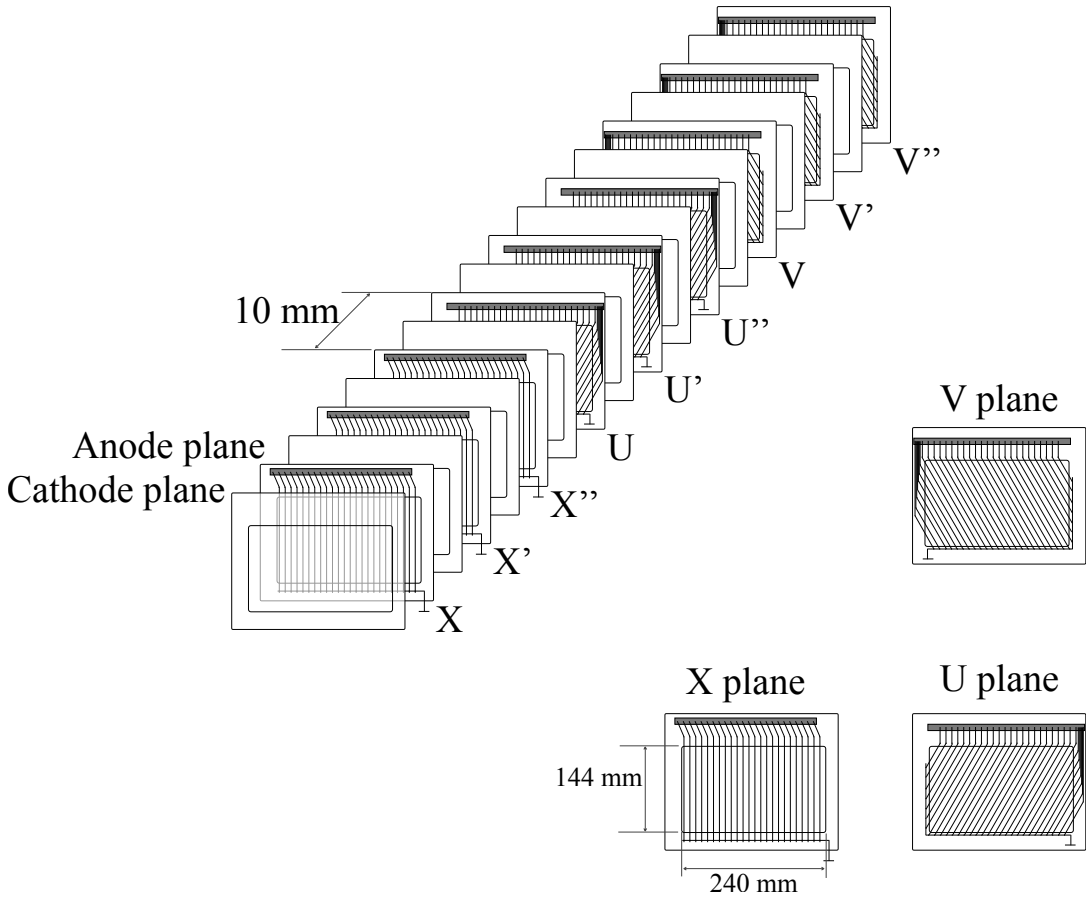

Figure 2.11: Schematic illustration of the lp-MWDCs (X-X'-X", U-U'-U", V-V'-V" type) at F5.

broken and not used. Instead, F7 counter was used. The upstream counter at F7 was used to make the trigger and the time reference of the MWDCs. The counter at F8 was installed downstream of γ-ray detector array and was used to check whether the transported ^{12}Be was stopped at the stopper. The size of the counters are listed at Table 2.6. Two set of scintillators were installed at F7. Photomultiplier tubes (PMTs) were equipped to both side of the scintillators except for the downstream one at F7. Multi-Pixel Photon Counters (MPPCs) were equipped to the downstream one at F7.

2.5.3 Parallel plate avalanche counters (PPACs)

Parallel plate avalanche counters (PPACs) with delay-line readout [78] were used at F7 and F8 in order to diagnose the image of the particles. The PPACs at F8 were used for the event rejection in the analysis as described in Sec. 3.1. The effective areas are 240×150 mm^2 (upstream of F7 and both of F8) and 150×150 mm^2 (downstream of F7). They consists of two sets of Cathode (horizontal)-Anode-Cathode (vertical) planes. Isobutane gas was used at several tens of torr. The operation voltages were typically

Table 2.5: Specification of MWDCs at F5

Sense wire	Au-W 20 μmϕ
Potential wire	Cu-W 75 μmϕ
Cell size	width = 10 mm, thickness = 10 mm
Gas	isobutane 10 kPa
Wire configuration	X = parallel to the vertical direction
	U = inclined by 30° with regard to vertical axis*
	V = inclined by −30° with regard to vertical axis*
Plane ordering along beam	XX'X"UU'U"VV'V" from downstream to upstream**
High Voltage	1350 V (upstream), 1255 V (downstream)
MWDC1-MWDC2 distance	633 mm

* Angles are measured in clockwise direction viewed from upstream.

** Wire positions of X' and X" planes are shifted by 1/3 and 2/3 cells, respectively.

Table 2.6: Plastic scintillation counters at each focal plane.

Focal plane	size
F3	$120 \times 100 \times 3$ mm^3
F5	$240 \times 100 \times 5$ mm^3
F7	$100 \times 100 \times 5$ mm^3
F8	$100 \times 100 \times 1$ mm^3

800–880 V.

2.5.4 Degraders

A copper plate with 10-mm thickness was placed just downstream of the F5 MWDCs. The plate has a wedge shape with the angle of 4 mrad in order to suppress the energy spread coming from the energy loss difference among the ^{12}Be particles. Area was 160×300 mm^2. Another copper plate with 13-mm thickness and an aluminum plate with 14.485-mm thickness were placed at F7 to decelerate ^{12}Be.

2.5.5 Stopper and γ-ray detector array of DALI2

The ^{12}Be particles were stopped at the stopper of ^{9}Be plate placed at F8. The material of the stopper of ^{9}Be was selected so that the delayed γ-rays are not produced via the production of the β-decaying nuclei. The size of the ^{9}Be stopper was $50^H \times 50^W \times 18.8^t$ mm^3.

The stopper was installed inside the beam pipe and surrounded by the crystals of

DALI2 array [69]. DALI2 is composed of 224 NaI(Tl) scintillator crystals with three types. The first type which is manufactured by SAINT-GOBAIN has dimension of $45 \times 80 \times 160$ mm^3. The second type which is manufactured by SCIONIX has dimension of $40 \times 80 \times 160$ mm^3. The third type which is manufactured by BICRON has dimension of $60 \times 60 \times 120$ mm^3. The PMTs were equipped to one side of the crystals. 224 crystals are divided into 10 layers along the beam direction. The plane view of the DALI2 array is shown in Fig. 2.12 and the placement of the crystals at each layer is shown in Fig. 2.13. The stopper was placed the 186.5 mm downstream of the face of the 1st layer of DALI2 array as shown in Fig. 2.14.

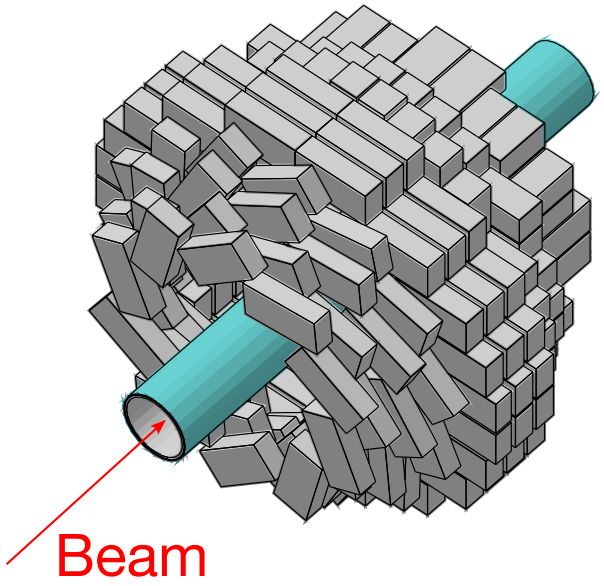

Figure 2.12: The plane view of the DALI2 array.

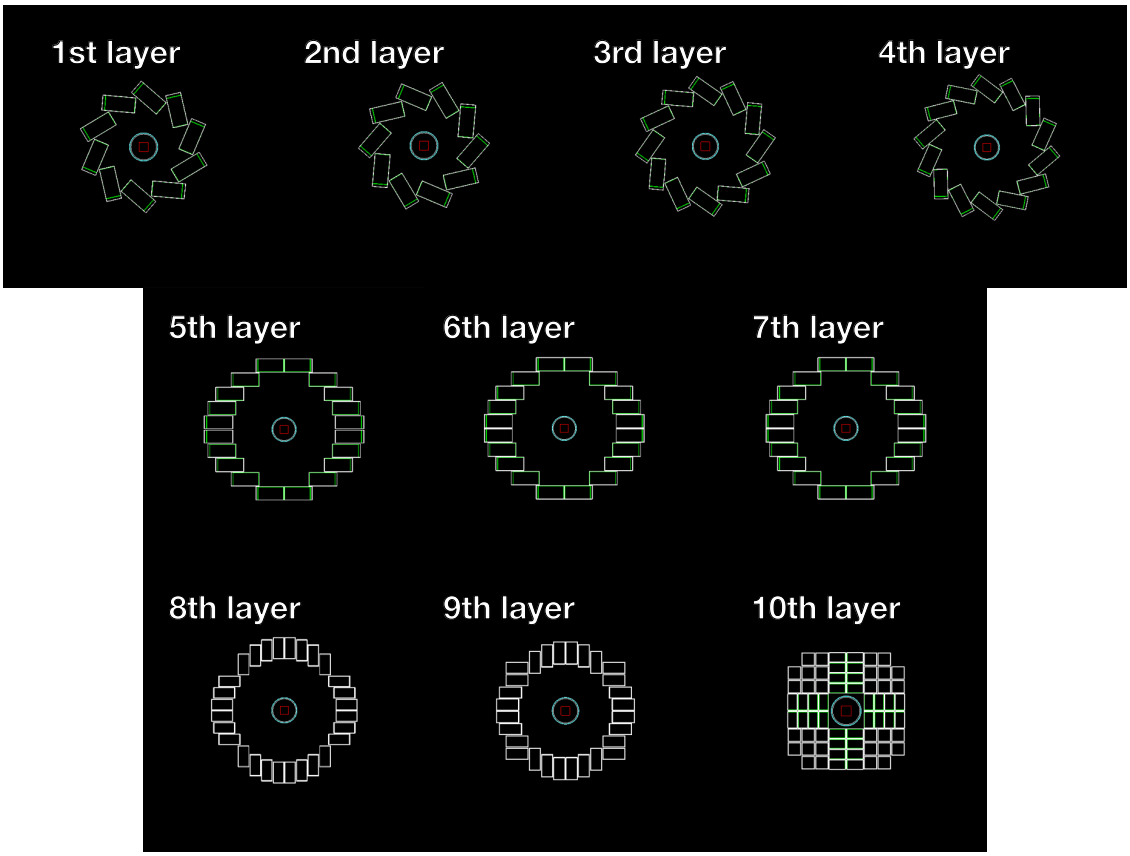

Figure 2.13: The place of the NaI(Tl) scnitillators at each layer. The red square expresses the ^{9}Be stopper.

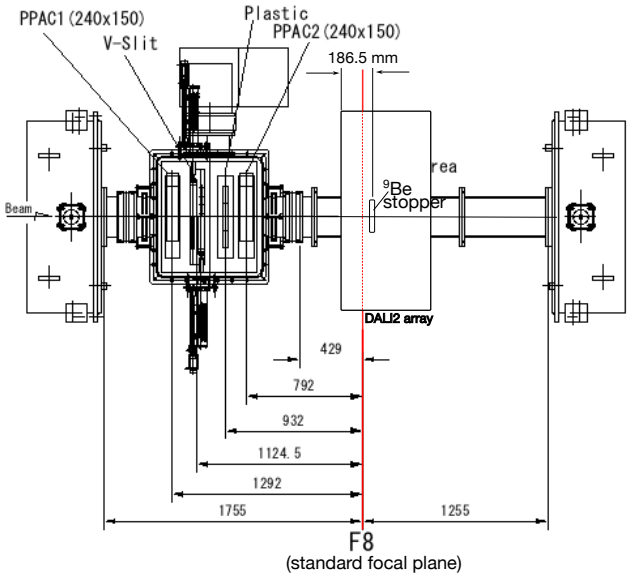

Figure 2.14: Relative position of the stopper around F8.

2.6 Data acquisition (DAQ) system

2.6.1 Signal processing

Figure 2.15 shows the outline of the data acquisition (DAQ) system of the experiment. The DAQ system was based on RIBFDAQ system [79]. In this experiment, four sets of DAQ systems are integrated: MWDCs at F3, MWDCs at F5, BigRIPS standard system, and DALI2 system. The data was acquired with a common trigger and common veto distributed by using the General Trigger Operator module (GTO) [80].

The signals from MWDCs at F3 were amplified and discriminated by the amplifier shaper discriminators (ASD) board, RPA-132, the prodcut of HAYASHI REPIC Co. Ltd., which provides a time over threshold information [81]. Timing signals from the ASD boards were read out by multi-hit time-to-digital converter module, V1190, the product of CAEN S.p.A. Digitized data was collected by using the mountable controller (MOCO) with parallelized VME (MPV) [82].

The signals from MWDCs at F5 were also put into RPA-132 boards, and output timing signals were read out by multi-hit AMT-TDC developed in KEK [83]. The charge information was also recorded as a time-over-threshold information. Digitized data was collected by MPV.

The signals from plastic scintillators and PPACs at F3, F5, F7, and F8 were processed with standard system used in BigRIPS. The output signals were sent to the counting room via optical fibers and were divided into several lines by a module of linear fan-in-fan-out. The charge information of plastic scintillators was recorded with charge-to-time converters (QTC) [84] modules. The other signals were put into Constant Fraction Discriminators (CFDs). The timing signals from QTCs and CFDs were put into time-to-digital converter module, V1290, the product of CAEN S.p.A. for plastic scintillators and V1190 modules for PPACs. The timing of Radio Frequency (RF) signal provided from the accelerator was also put into V1290. Digitized data was collected with MPV.

The signals from NaI(Tl) detectors of DALI2 array were amplified and shaped by CAEN N568B. The charge information was recorded by CAEN V785. The divided signals were put into CFDs and timing information was recorded by CAEN V1190. Digitized data was collected by using V7867 VME CPU module. The data was recorded within the timing window which was set to 2 μs in order to detect the delayed γ-rays deriving from the decay of $^{12}\mathrm{Be}(0_2^+)$.

The numbers of accepted triggers, requested triggers, and other number of the detector hits were recorded by a scaler of SIS3820, the product of Struck Innovative Systeme GmbH. The number of the coincidence of the stack of three plastic scintillator counters at F0 was also recorded to monitor the primary beam intensity during the run.

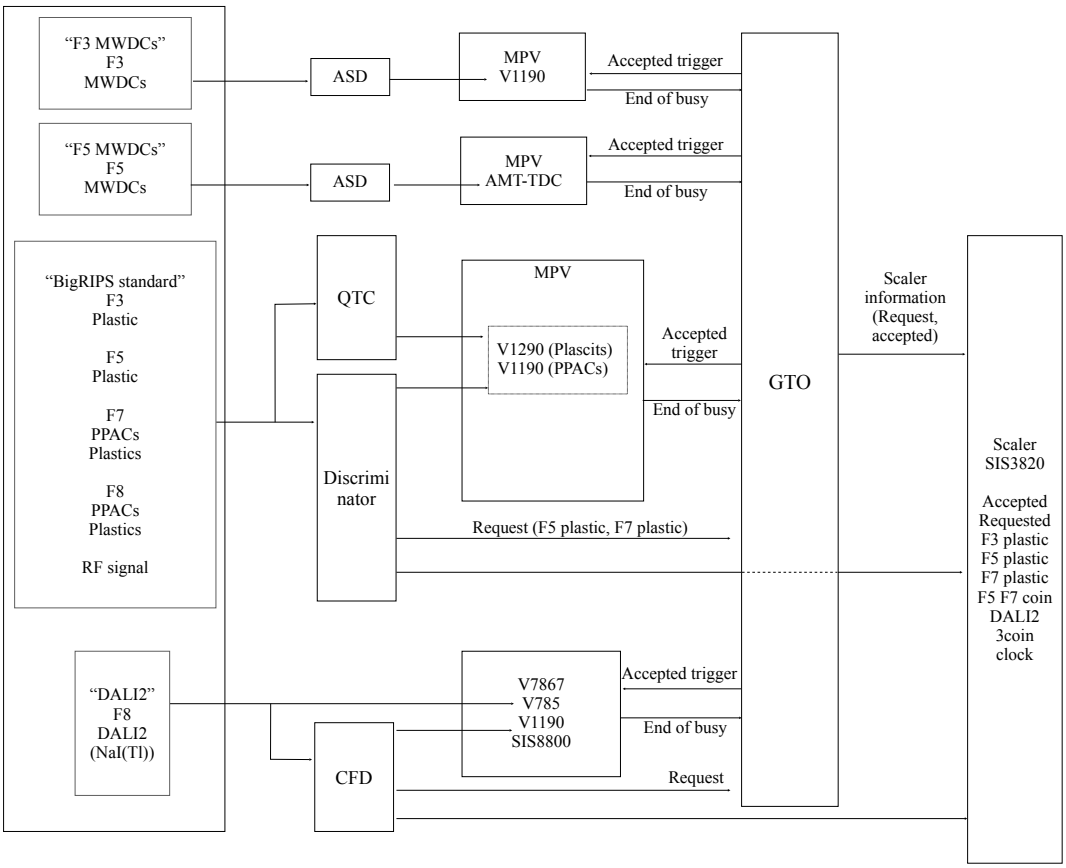

Figure 2.15: Outline of the data acquisition system.

2.6.2 Trigger condition

In the double charge exchange measurement, three types of trigger request signals were put into GTO module: (a) Coincidence of signals from the left and right side of plastic scintillator (LR coincidence) at F7, (b) signals from left side of plastic scintillator at F5 which is down-scaled by 1/500, and (c) signals from NaI(Tl) scintillators of DALI2 array which is down-scaled by 1/180. The data were recorded with the condition of OR of these signals. The processing of the signals from plastic scintillator at F7 and that from DALI2 is described in Fig. 2.16 and Fig. 2.17. The events with the LR coincidence at F7 were used for the analysis of the (^{12}C, ^{12}Be(0^+_2)) reaction.

2.7 Run summary

The conducted measurements in the experiment in 2021 are summarized in Table 2.7. The target, analyzed particle by BigRIPS, settings of the magnetic field B in the unit of $B\rho$ (ρ: orbit radius), intensity of the primary beam of ^{12}C, duration of the measurement, and the purpose are shown.

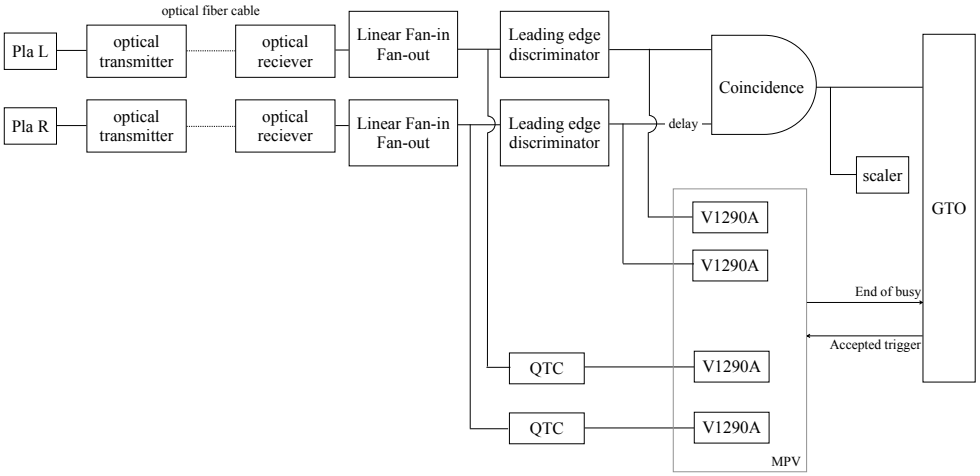

Figure 2.16: Diagram of the signal processing from the scintillator at F7 and the trigger making from the signal.

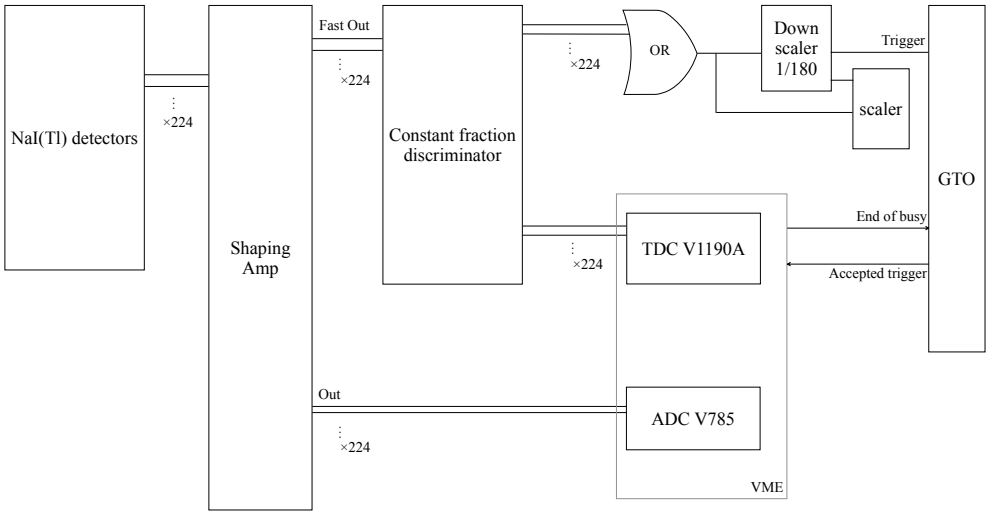

Figure 2.17: Diagram of the signal processing from DALI2 array and the trigger making from the signal.

The double charge exchange (DCX) (^{12}C, ^{12}Be(0^+_2)) measurements were performed for ^{48}Ca and ^{116}Cd target. The measurement with same reaction was also performed with graphene target for the purpose of the study of the background event in the measurement of ^{48}Ca target.

The single charge exchange (SCX) (^{12}C, ^{12}B) measurements were performed with ^{48}Ca target and graphene target. The SCX measurement were performed for the purpose of the reference of the analysis: verification of the energy calibration, optics study, and the reference of the reaction calculation.

The the transfer matrix between F0 and F7 was examined with ^{8}Li produced via pro-

jectile fragmentation in a 50 mg/cm^2 ^{116}Cd target. The tuning of the optical system upstream of F0 was performed with transporting the primary beam of ^{12}C with a faint intensity to F7 without target at F0.

The measurements with ^{3}He was performed for the purpose of the study of the subsequent experiment of pionic atoms spectroscopy [85]. The dispersion is evaluated utilizing the data in this measurement.

The measurement with ^{10}Be produced via projectile fragmentation in a 50 mg/cm^2 ^{116}Cd target was performed for detector conditioning.

Table 2.7: Run summary of the experiment

target	analyzed particle	$B\rho$ [T·m]	Intensity	Duration	Purpose
^{48}Ca	^{12}Be	7.2	2000 min	600 pnA	DCX
^{116}Cd	^{12}Be	7.2	1000 min	600 pnA	DCX
^{48}Ca	^{12}B	5.8	150 min	10 pnA	SCX
graphene	^{12}Be	7.2	120 min	200 pnA	BG study of DCX
graphene	^{12}B	5.8	60 min	10 pnA	SCX (calibration)
^{116}Cd	^{8}Li	7.2	400 min	-	study of transfer matrix of BigRIPS (F0–F7)
Cu 25 mm	^{3}He	2.4	60 min	-	dispersion measurement
(none)	^{12}C	4.8	200 min	-	Optics tuning upstream of F0
^{116}Cd	^{10}Be	6.0	60 min	-	detector conditioning

Chapter 3

Data analysis

3.1 Event selections for ^{12}Be(0^+_2)

The ^{12}Be(0^+_2) events are selected by identifying ^{12}Be using the charged particle detectors placed from F5 to F8, and detecting decaying γ-rays at F8 with DALI2. The evaluation of the efficiency of DALI2 is also discussed in this section.

3.1.1 Event selections for ^{12}Be

The scattered ^{12}Be are selected by the energy deposited in MWDC2 at F5 and the plastic scintillator at F7 for the events in which the F8 PPAC is triggered. Figure 3.1 shows the correlation of the energy deposits in the F5 MWDC and the F7 plastic scintillator with the software cut adopted in the analysis.

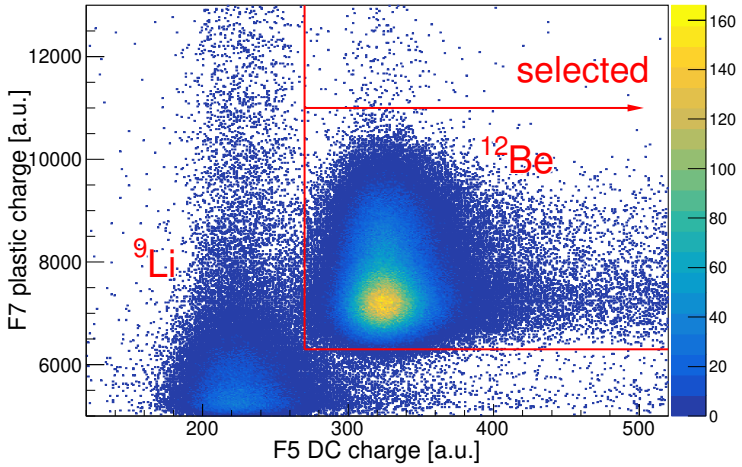

Figure 3.1: Correlation of charge distribution at F7 plastic and F5 MWDC2. Overlaid lines define the selected region.

The contamination and the inefficiency are evaluated from the extrapolation of the projection of the distribution. Figure 3.2 shows the projection of the charge distribution of MWDC2 with gating the charge in the F7 plastic scintillator. There are two components with peaks at 230 ch and at 330 ch, corresponding to ^{9}Li and ^{12}Be, respectively. We fitted the charge distribution with two Gaussians. The contamination of the tail of the lower component inside the gate is 0.08% of the selected events, while the loss of the higher component out of the gate is 0.03% of the selected events. Similarly, Fig. 3.3 shows the projection of the charge distribution of the F7 plastic scintillator with gating the charge measured with MWDC2. The contamination of the tail of the lower component inside the gate is 0.04% of the selected events, while the loss of the higher component out of the gate is 0.5% of the selected events. Thus the selected events possibly contain 0.08% of the contamination of ^{9}Li and 0.5% of the loss of ^{12}Be. The uncertainty of the number of the contamination and the loss is 1% to the value at maximum.

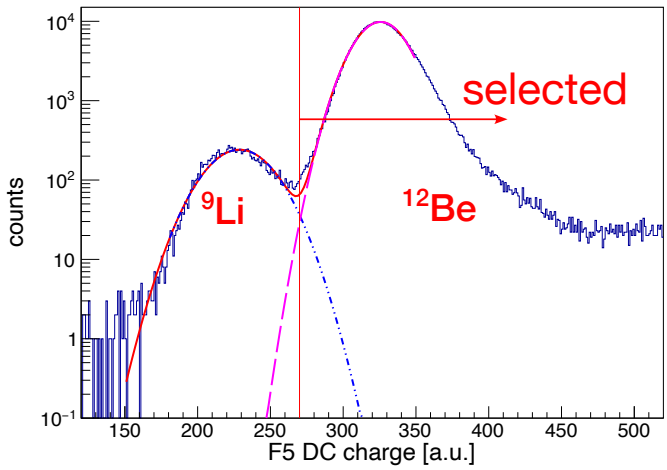

Figure 3.2: Projected distribution of the charge in F5 MWDC2 with the gate on the charge in F7 plastic (> 6300 ch).

3.1.2 Event selections for ^{12}Be(0^{+}_{2})

The isomeric states of ^{12}Be(0^{+}_{2}) are selected by the timing and the energy of the γ-rays measured with DALI2.

The measured data of charge are converted to energy of γ-rays by using the measured data with calibration sources of ^{137}Cs and ^{60}Co. The photo peaks at 662 keV from ^{137}Cs and 1173 keV and 1333 keV from ^{60}Co are used for the calibration. The measurements with these sources were performed just before and after the production measurement. The peak positions are fitted by Gaussian function and calibration parameters are made by each crystal. The conversion function is obtained as a parameter of the linear function for individual crystals. The energy spread of the photo peak of ^{137}Cs is 31 keV (FWHM).

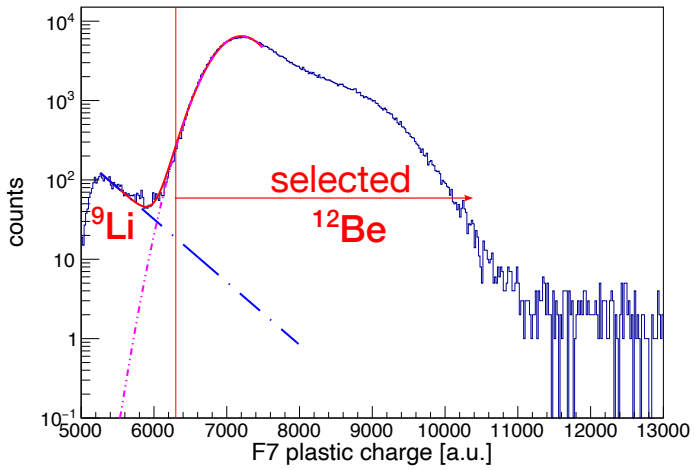

Figure 3.3: Projected distribution of the charge in F7 plastic with the gate on the charge in F5 MWDC2 (> 270 ch).

The fluctuation during the double charge exchange (DCX) measurement is examined by the charge distribution bundled up by 5 hours. The fluctuation is up to 1% of the dynamic range and is negligible.

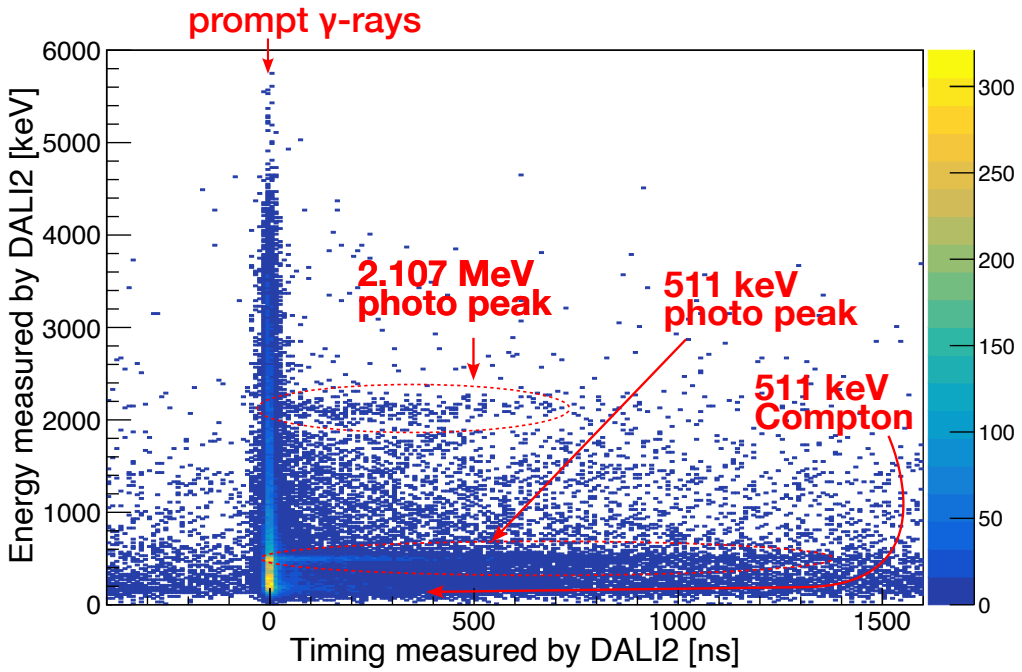

Figure 3.4: The timing and the charge measured by DALI2.

The timing offsets in the DCX measurement are corrected by setting the timing of the prompt γ-rays as an origin. We aligned the origin of the timing distribution by fitting the timing spectrum for each crystal with Gaussian distribution.

The timing distribution against the charge is shown in Fig. 3.4. The loci corresponding to the photo peaks of 511-keV and the Compton scattering are seen. There is another locus at 2.1 MeV, which is also attributed to the γ-rays from ^{12}Be(0^+_2). ^{12}Be(0^+_2) decays into the ground state directly by emitting e^+e^- pair with the branching ratio of 87.3% [86] while the rest decays via 2^+ ($E_{\rm ex}$ = 2.107 MeV) state by emitting 0.144 MeV and 2.107 MeV γ-rays. The locus at 2.1 MeV is attributed to the photo peak of the 2.107-MeV γ-rays.

The left panel of Fig. 3.5 shows the energy distribution of the γ-rays. The photo peak at 511 keV is clearly seen. The main background in the data is accidental coincidence between ^{12}Be and room-background γ-rays. The accidental coincidence ratio and its energy distribution is evaluated by gating γ-ray timing in 100–400 ns before the prompt γ-rays. The corresponding energy spectrum is shown in red in the left panel of Fig. 3.5. There is no peak corresponding to 511-keV γ-rays in the background spectrum. It suggests that the background deriving from β^+-emitter is not negligible. It should be noted that β^+-emitter in the stopper is the main source of the background in the previous experiment at RCNP [65]. The energy gate is set to $E_\gamma < 580$ keV. The main component is attributed to the 511-keV photons.

The right panel of Fig 3.5 shows the timing distribution of the γ-rays for $E_\gamma < 580$ keV. The decay curve is fitted with the function of an exponential and a constant background, $p_0 \cdot \exp\{-t/p_1\} + p_2$. The decay constant is found to be 302 ± 7 ns, which is consistent to the literature value of 331 ± 12 ns [57]. The constant background reflects the accidental coincidence between ^{12}Be and room-background γ-rays.

The timing gate starts 20 ns after the signal of the prompt γ-rays. The end time of the gate is determined so that the signal-to-noise (S:N) ratio is optimized. We assume that the exponential part and the constant part of the fit results of the timing distribution correspond to the number of the signal (true) events and noise (background) events, respectively. The number of signal and background events within a given timing gate can be calculated by integrating the fit function. The optimization was performed so as to minimize the relative error of $\Delta N_{\rm signal}/N_{\rm signal} = \sqrt{(\Delta N_{\rm all})^2 + (\Delta N_{\rm BG})^2}/N_{\rm signal}$, where $N_{\rm signal}$ and $N_{\rm BG}$ are the number of signal and background events within the gate, and $N_{\rm all}$ is the whole events within the gate and adopted ($N_{\rm all} = N_{\rm signal} + N_{\rm BG}$). The gate width is determined to be 940 ns.

Detection of at least one of the γ-rays from ^{12}Be(0^+_2) in DALI2 is required within the timing and the energy gates described above. The contamination is estimated to be 10% of the total events and is eventually eliminated in the evaluation of the DGT components of the cross section.

3.1.3 Estimation of the tagging efficiency

The detection efficiency is estimated using a simulation with GEANT4 [69]. The geometry of 224 NaI counters is fully considered.

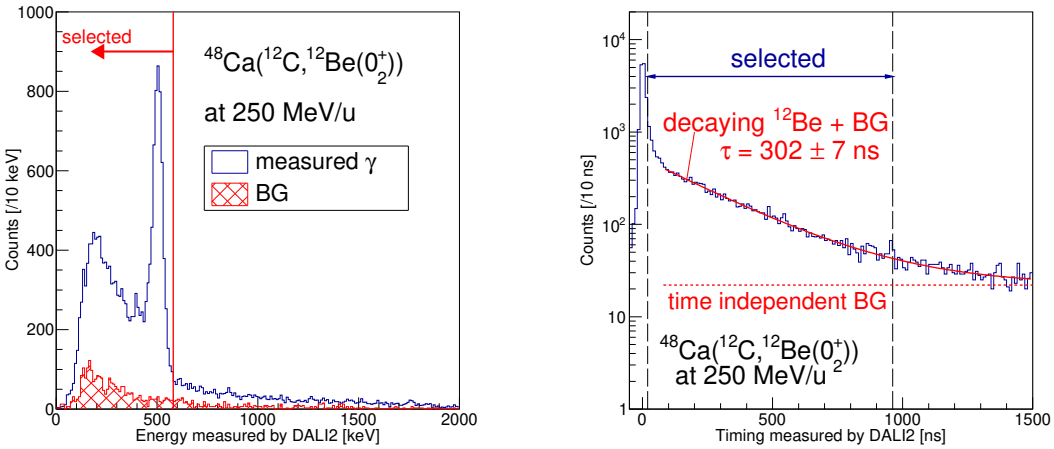

Figure 3.5: The spectra of γ-rays measured by DALI2. The energy distribution (left), the timing distribution (right).

The detection efficiency for back-to-back 511-keV γ-rays

In the simulation, a pair of γ-rays are generated with the energy of 511 keV and the direction is 180° from each another. The γ-rays are generated from the center of the ^{9}Be stopper. The energy deposited in each crystal is recorded and smeared by the resolution ΔE which is calculated by the function depending on the photon energy as $\Delta E = 2.256\sqrt{E}$ keV. The efficiency is estimated by counting the number of the events satisfying the same condition as in the data analysis. 73% of the generated events are within the gate.

The detection efficiency for 2.107-MeV γ-rays

2.107 MeV and 144 keV γ-rays are generated from the center of the ^{9}Be at the same time. The energy distribution before and after smearing is shown in Fig. 3.7. In this simulation, 27% of the generated events are within the gate.

3.1.4 Checking the validity of the simulation in source measurement

The data of the measurements with ^{137}Cs source are used to check the validity of the simulation. The source was attached to the upstream or downstream face of the ^{9}Be stopper. Measurement without the stopper but with the source placed at the stopper position instead, was also performed. The detection efficiency estimated from the rate and the measurement time is 25.0% (without stopper) and 23.4% (with stopper). On the other hand, the detection efficiencies in the simulation are 22.2% (without stopper) and 19.8% (with stopper). The reproducibility in the efficiency is 15% relatively. The simulation for 511-

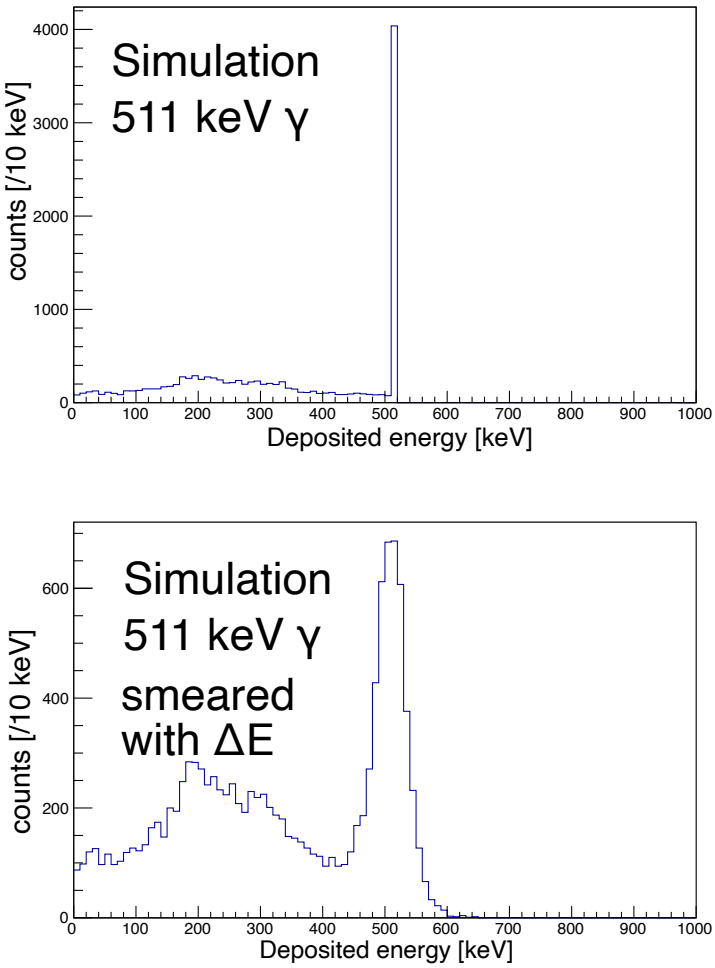

Figure 3.6: The simulated energy distribution deposited in the scintillators of DALI2 array for the 511 keV γ-rays. Lower panel shows the smeared distribution with experimental resolution ΔE.

or 2107-keV γ-rays might also deviate to this extent. Therefore, the efficiency is regarded as $73\pm11\%$ for 511-keV γ-ray and $27\pm4\%$ for 2.107-MeV γ-ray. Considering the branching ratio, the tagging efficiency of ^{12}Be(0^+_2) is $(73 \pm 11\%) \times BR(511\text{ keV}) + (27 \pm 4\%) \times BR(2.107\text{ MeV}) = 67\pm10\%$, where $BR(511\text{ keV}) = 87.3\%$ and $BR(2.107\text{ MeV}) = 22.7\%$ are the branching ratios, respectively.

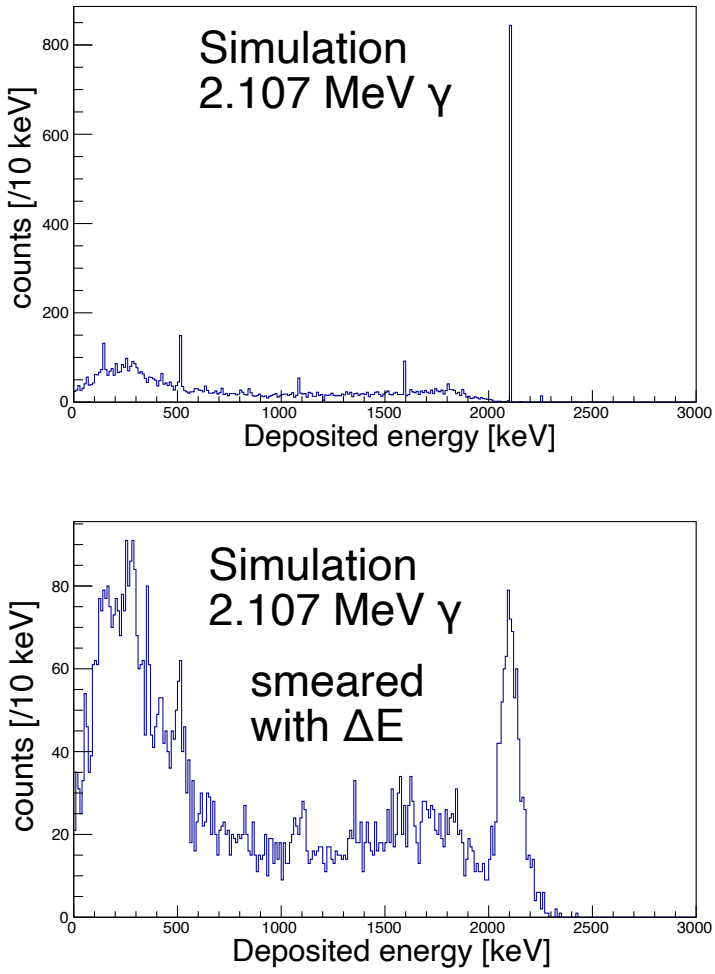

Figure 3.7: The simulated energy distribution deposited in the scintillators of DALI2 array for the 2.107 MeV and 144 keV γ-rays. Lower panel shows the smeared distribution with experimental resolution ΔE.

3.2 Tracking of ^{12}Be

The trajectories of ^{12}Be at F5 are determined by using two sets of MWDCs. The detailed description is presented in Appendix A.

3.2.1 Geometry

The two sets of MWDCs, MWDC1 (upstream) and MWDC2 (downstream) were placed inside of the F5 vacuum chamber. The wire configuration is X-X'-X"-U-U'-U"-V-V'-V" in each chamber. The direction of the wires in X, X', and X" planes is vertical to the horizontal (x) axis. The directions in U, U', and U" and V, V', and V" planes are tilted 30° and −30° to the wires in X plane, respectively. The placement of the wires is illustrated in Fig. 3.8. The pitch of the sense wires is 10 mm and the distances between wire planes are 10 mm. The wires in X' (U', V') and X" (U", V") planes are placed with the shift of 1/3-cell and 2/3-cell against to wires in X (U, V) plane, respectively. The distance between two MWDCs measured from the U'-wire plane of each is 633 mm.

3.2.2 Determination of the hit position in each plane

The position of the scattered particle in each plane is determined from the drift time. The drift time was measured as a time difference between the MWDC signals and the F7 scintillator signal. The drift time, dt, is converted to the drift distance, dl, from the sense wire using a conversion function. The data of ^{10}Be is employed to make the conversion function. The evaluation of the conversion function of the drift time to distance is described in Appendix A. Thus the one-dimensional position along the axis vertical to the wire direction (x_j, u_j, v_j axis in Fig. 3.8) is obtained at which the particle passed through. The position resolution in each plane is approximately 0.3 mm as described in Appendix A.3.

3.2.3 Tracking in 1/3-cell staggered MWDCs

The trajectory of the particle is determined by the least squares method. X_i, the position at which the particle passed in ith plane, is determined so that the following χ^2 is minimized,

$$\chi^2 = \sum_i^N \frac{(X_i - x_i)^2}{\sigma_i^2}, \tag{3.1}$$

where $N = 18$ is the number of planes used in the analysis. As X_i are located on the straight trajectory, X_i is linear as a function of z. x_i is the observed position along the axis of x_j, u_j, v_j. σ_i express the resolution in ith plane. $\sigma_i = 0.3$ mm is applied for the hit in which $0.6 < dl < 4.4$ mm. For the planes $dl < 0.6$ mm and $dl < 4.4$ mm, $\sigma_i = 2.0$ mm is applied. This helps to avoid using the timing information from the MWDC planes with

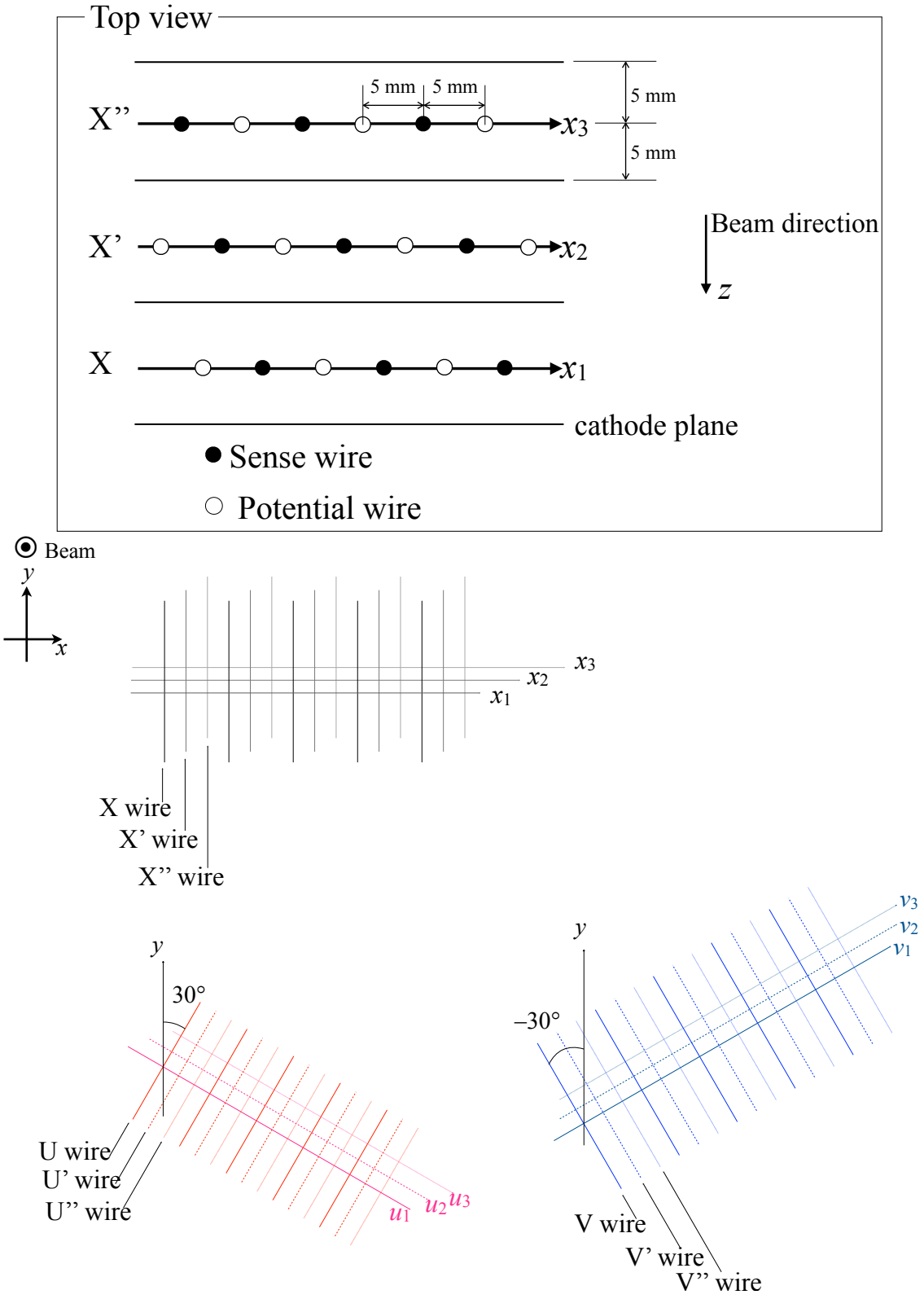

Figure 3.8: Illustration of the wire configuration of F5 MWDCs.

hits near to the cell boundaries or close to the sense wire. The details of the analysis are described in Appendix A. The left-right combination is determined with the best value of the χ^2.

The trajectory of the particle is obtained by the determination of X_i, as a set of parameters: the horizontal position X, the vertical position Y, the angle projected to xz-plane a, and the angle projected to yz-plane b. The position resolution is ΔX =0.1 mm (horizontal) and ΔY =0.2 mm (vertical). The angular resolution is Δa = 0.3 mrad and Δb = 0.7 mrad.

Figure 3.9 shows the horizontal position distribution obtained by the tracking analysis. The ^{12}Be(0^+_2) events selected by the gates described in Sec. 3.1 are shown. The negative direction corresponds to the higher excitation energy in ^{48}Ti. In the following section, the conversion of the horizontal position at F5 to the excitation energy and the deduction of the scattering angle at F0 from the trajectory at F5 are described.

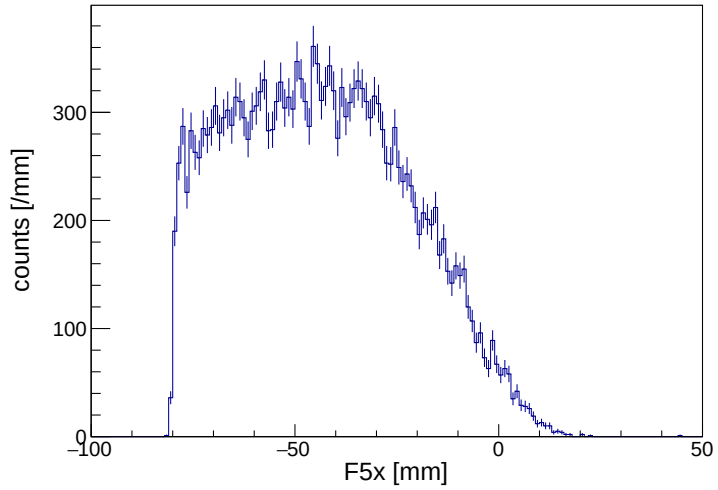

Figure 3.9: The horizontal position distribution at F5 obtained in the tracking analysis.

3.3 Reconstruction of angles and momenta at the target

The scattering angles and momenta of ^{12}Be are obtained from the trajectories at F5 using the ion-optical transfer matrix. In this section, the reconstruction of the horizontal angle a, vertical angle b (F0a and F0b, respectively), and the momentum deviation δ is described.

3.3.1 Procedure of the reconstruction

Scattering angles at F0

The angles at F5, F5a (horizontal) and F5b (vertical) reflect the angles at F0, F0a and F0b. The main dependence of the values at F5 on F0 is described as

$$\mathrm{F5}a = (a|a)_{\mathrm{F0}\to\mathrm{F5}} \cdot \mathrm{F0}a, \tag{3.2}$$

$$\mathrm{F5}b = (b|b)_{\mathrm{F0}\to\mathrm{F5}} \cdot \mathrm{F0}b + (b|b\delta)_{\mathrm{F0}\to\mathrm{F5}} \cdot \mathrm{F0}b \cdot \delta + (b|b\delta\delta)_{\mathrm{F0}\to\mathrm{F5}} \cdot \mathrm{F0}b \cdot \delta^2, \tag{3.3}$$

respectively, where $(X_i|X_j)_{\mathrm{F0}\to\mathrm{F5}}$ is the transfer matrix elements, the coefficient describing the value of X_i at F5 (X_i = F5x (horizontal position at F5), F5y (vertical position at F5), F5a (horizontal angle at F5), F5b (vertical angle at F5)) as a polynomial of the value of X_j at F0 (X_i = F0x (horizontal position at F0), F0y (vertical position at F0), F0a (horizontal angle at F0), F0b (vertical angle at F0), momentum deviation of the particle δ defined using the momentum of the particle p and that of the central ray p_c, as $\delta = (p - p_c)/p_c$). $(b|b\delta)_{\mathrm{F0}\to\mathrm{F5}}$ and $(b|b\delta\delta)_{\mathrm{F0}\to\mathrm{F5}}$ express the higher order dependence on δ. Thus the angles at F0 are obtained as

$$\mathrm{F0}a = \frac{\mathrm{F0}a}{(a|a)_{\mathrm{F0}\to\mathrm{F5}}}, \tag{3.4}$$

$$\mathrm{F5}b = \frac{\mathrm{F5}b}{(b|b)_{\mathrm{F0}\to\mathrm{F5}} \cdot + (b|b\delta)_{\mathrm{F0}\to\mathrm{F5}} \cdot \delta + (b|b\delta\delta)_{\mathrm{F0}\to\mathrm{F5}} \cdot \delta^2}. \tag{3.5}$$

The procedure is as follows:

- Offset of F5a and F5b are corrected
- $(a|a)_{\mathrm{F0}\to\mathrm{F5}}$, $(b|b)_{\mathrm{F0}\to\mathrm{F5}}$, $(b|b\delta)_{\mathrm{F0}\to\mathrm{F5}}$, $(b|b\delta\delta)_{\mathrm{F0}\to\mathrm{F5}}$ are evaluated mainly from the data of ^{7}Li
- A relative scale of $(a|a)_{\mathrm{F0}\to\mathrm{F5}}$ and $(b|b)_{\mathrm{F0}\to\mathrm{F5}}$ is determined so as the horizontal and vertical distribution to be symmetric
- Absolute value of $(b|b)_{\mathrm{F0}\to\mathrm{F5}}$ (or $(a|a)_{\mathrm{F0}\to\mathrm{F5}}$) is determined so as to reproduce the kinematic curve in vertical direction
- $(x|aa)_{\mathrm{F0}\to\mathrm{F5}}$ is determined so as to reproduce the kinematic curve in the horizontal direction

Momentum

The momentum deviation of the particle $\delta = (p - p_c)/p_c$ is deduced from

$$\mathrm{F5}x' = (x|\delta)_{\mathrm{F0}\to\mathrm{F5}} \cdot \delta \tag{3.6}$$

The aberration of F5x due to $(x|aa)_{\mathrm{F0}\to\mathrm{F5}}$ is corrected (F5x'). The dispersion $(x|\delta)$ is obtained from the data of ^{3}He. p_c is obtained from NMR.

3.3.2 Reconstruction of angles

Correction of offset

The offsets of the angle obtained in the tracking are evaluated. The possible causes are an imperfect alignment or an inclination of the chambers, so the offsets can be coupled with horizontal position. Figure 3.10 shows the angular distributions at F5 each region of horizontal position F5x in the double charge exchange (DCX) reaction. The yield should be highest at the most forward angle, thus the correction of the offset is performed so that the peak position is 0. The center of the distribution is determined from the projection to each direction at each region of F5x. The dependences on F5x of the offsets of F5a and F5b are shown in Fig. 3.11. The dependences are fitted by a linear function, and obtained function is used for the correction of the offsets.

Horizontal angular reconstruction

The transfer matrix element of $(a|a)_{\mathrm{F0}\to\mathrm{F5}}$ is deduced from the relation of F3a = $(a|a)_{\mathrm{F0}\to\mathrm{F3}}$ · F0a and F5a = $(a|a)_{\mathrm{F3}\to\mathrm{F5}}$ · F3a, thus $(a|a)_{\mathrm{F0}\to\mathrm{F5}} = (a|a)_{\mathrm{F0}\to\mathrm{F3}} \cdot (a|a)_{\mathrm{F3}\to\mathrm{F5}}$.

$(a|a)_{\mathrm{F3}\to\mathrm{F5}}$ is obtained from the data of ^{8}Li produced via projectile fragmentation in a 50 mg/cm^2 thick ^{116}Cd target. The correlation between F5a and F3a is shown in Fig. 3.12. The distribution is fitted by a linear function and $(a|a)_{\mathrm{F3}\to\mathrm{F5}}$ is obtained as the obtained coefficient.

The transfer in the horizontal direction between F0 and F3 is studied by constraining the position by a slit. The central position of the slit was −7, 0, 7 mm. The correlation between F3x and F0x is shown in Fig. 3.13. $(x|x)_{\mathrm{F0}\to\mathrm{F3}}$ is evaluated as −0.94 from the correspondence with the horizontal position at F3. Using Liouville's theorem, $(x|x) \cdot (a|a) - (x|a) \cdot (a|x) = 1$. The $(a|a)_{\mathrm{F0}\to\mathrm{F3}}$ is evaluated as the inverse of the $(x|x)_{\mathrm{F0}\to\mathrm{F3}}$.

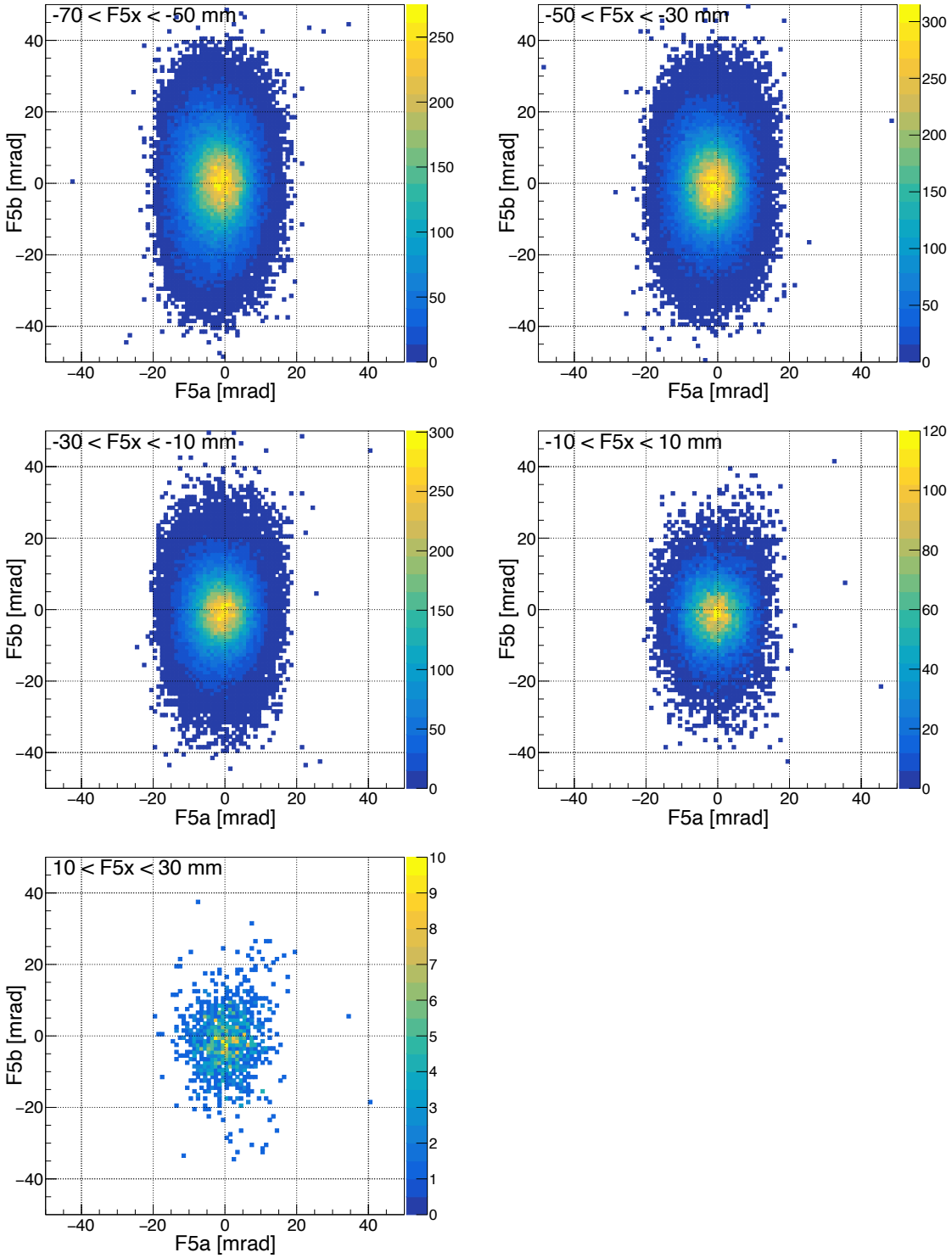

Figure 3.10: Measured angular distribution at F5 at each region of the horizontal position at F5.

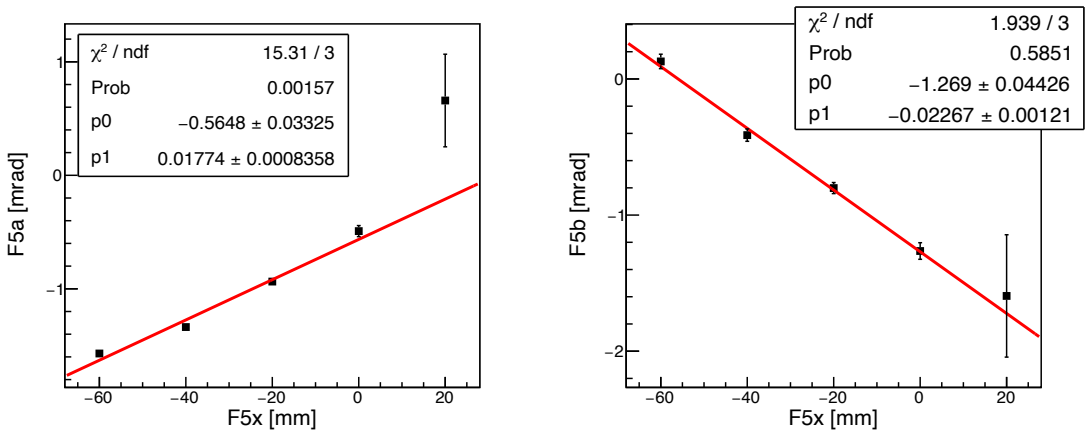

Figure 3.11: Dependence of the offset of angles on the horizontal position at F5. Left: The offset of horizontal angle F5*a*. Right: The offset of vertical angle F5*b*.

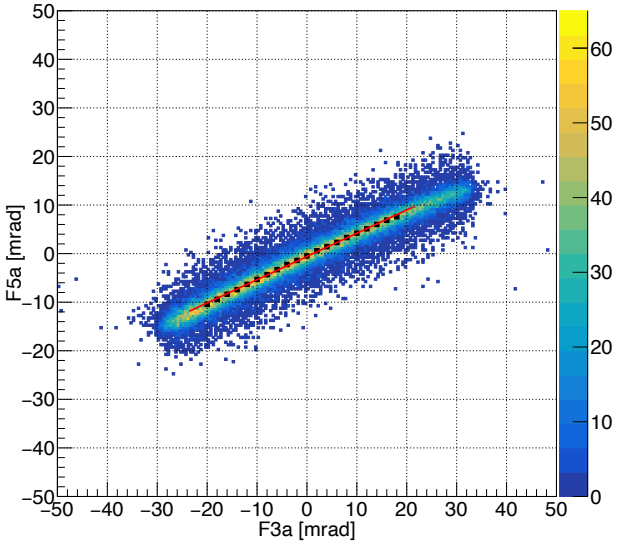

Figure 3.12: Correlation between F3a and F5a.

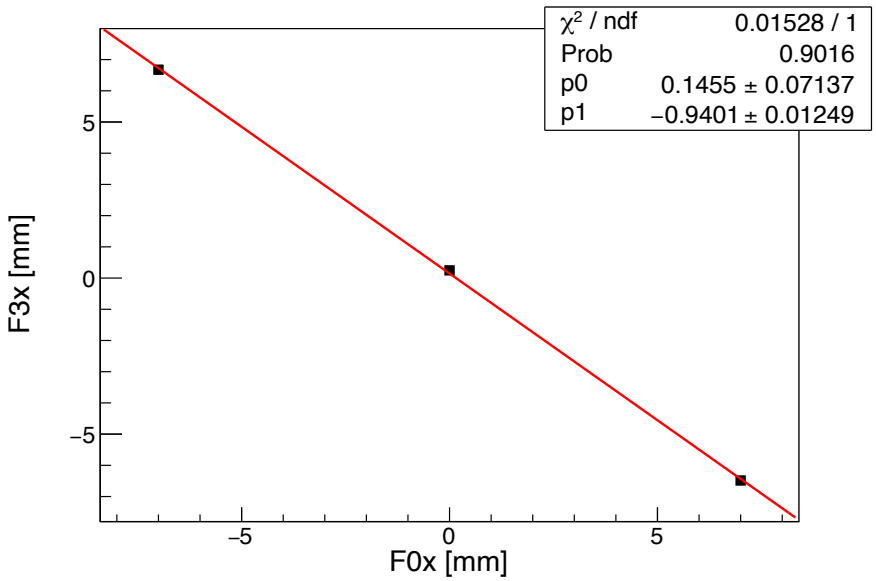

Figure 3.13: Correlation between F3x and F0x.

Vertical angular reconstruction

The relations between F0b and F5b are obtained as dependent values on δ. As we have no detectors at F0 nor calibration measurement for the vertical direction, F0b is reconstructed from the image at F3 using the calculated transfer matrix by GICOSY. Figure 3.14 shows the correlation between F5b and F0b which are obtained from the image at F3. Each panel shows different regions of F5x, corresponding to different δ values. They are fitted by a linear function and the coefficients are plotted against δ as shown in Fig. 3.15. The correlation between the coefficients and δ is fitted by a quadratic polynomial. Thus $(b|b)$, $(b|b\delta)$, and $(b|\delta\delta)$ are obtained.

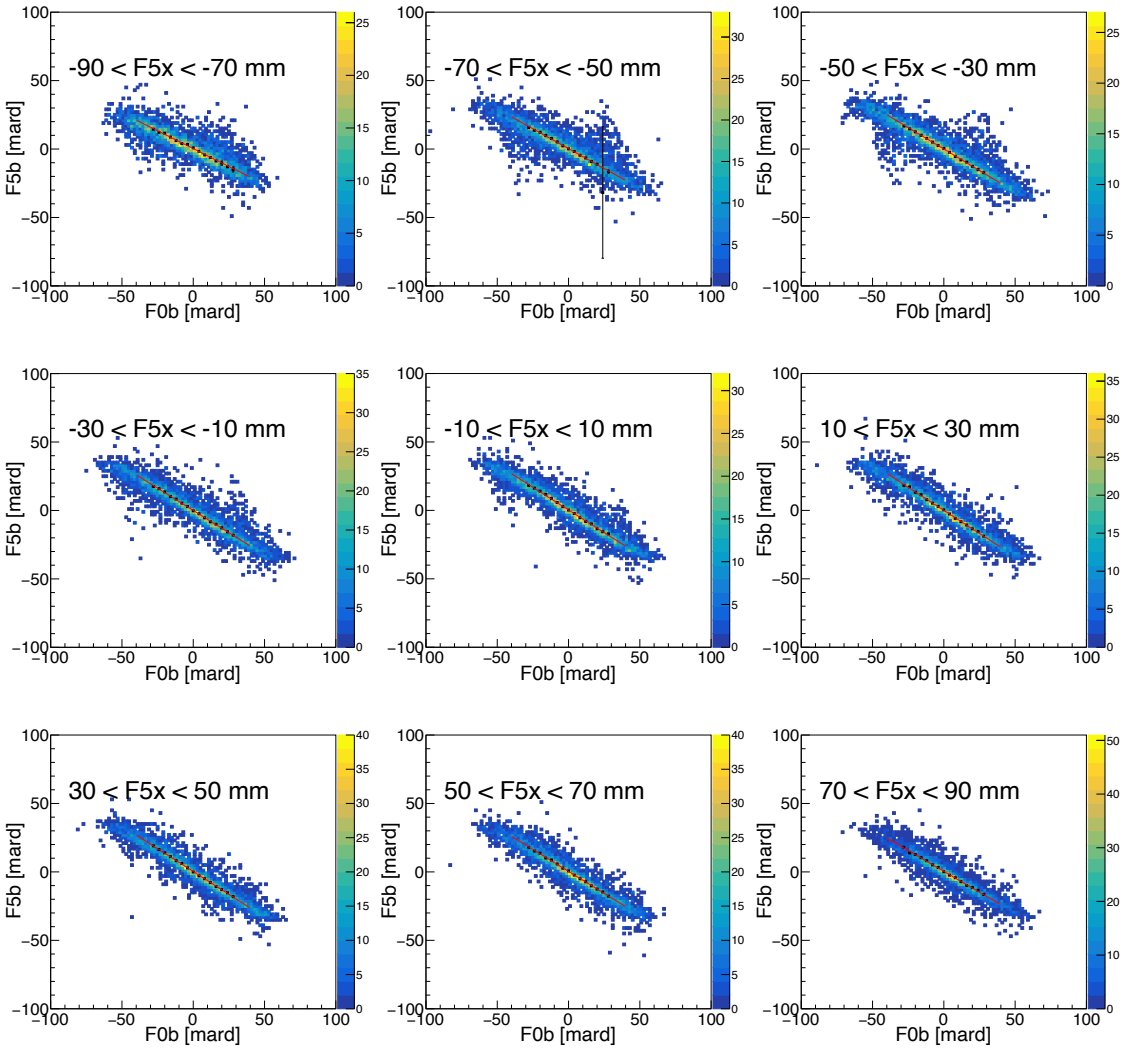

Figure 3.14: Correlation between F5b and F0b. Each panel shows the each region of horizontal position at F5 (F5x), which correspond to different δ.

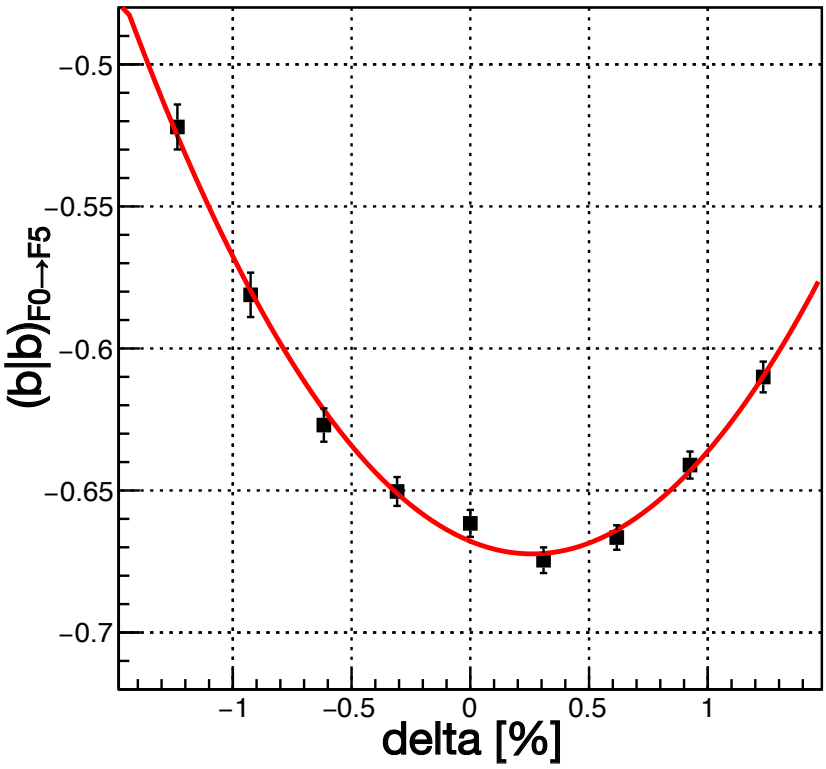

Figure 3.15: The slope of linear functions shown in Fig. 3.14 plotted against δ. The result of the fit with a quadratic polynomial is shown in red curve.

3.3.3 Correction of transfer matrix elements

The obtained elements of the transfer matrix are fine-tuned by utilizing the data of the single charge exchange reaction of the ^{12}C(^{12}C, ^{12}B) reaction, considering some constraints.

Symmetry of the scattering angle

The system in the ^{12}C(^{12}C, ^{12}B) measurement is symmetric in polar angle, so the reconstructed horizontal and vertical distribution should be the same size. Figure 3.16 shows the reconstructed angles using the transfer matrix deduced above. Figure 3.19 shows the projection to each direction. The widths evaluated by the Gaussian fit are 8.1 mrad (horizontal) and 10.0 mrad (vertical) in σ, respectively. This means that the scale of the horizontal angle from F5 to F0 is relatively underestimated to the vertical angle, and thus $(a|a)_{\mathrm{F0}\to\mathrm{F5}}$ is relatively overestimated to $(b|b)_{\mathrm{F0}\to\mathrm{F5}}$ or $(b|b)_{\mathrm{F0}\to\mathrm{F5}}$ is relatively underestimated to $(a|a)_{\mathrm{F0}\to\mathrm{F5}}$. The relative scale of $(a|a)_{\mathrm{F0}\to\mathrm{F5}}$ to $(b|b)_{\mathrm{F0}\to\mathrm{F5}}$ are examined in which the horizontal and vertical widths are the same. Figures 3.17 and 3.20 show the same ones as Fig. 3.16 and Fig. 3.19 but $(a|a)_{\mathrm{F0}\to\mathrm{F5}}$ is multiplied by 0.85 while $(b|b)_{\mathrm{F0}\to\mathrm{F5}}$ is fixed. The horizontal and vertical widths are adjusted to be equal to each other with this scale. Similarly, Fig. 3.18 and Fig. 3.21 show the same ones but $(b|b)_{\mathrm{F0}\to\mathrm{F5}}$ is multiplied by 1.18 while $(a|a)_{\mathrm{F0}\to\mathrm{F5}}$ is fixed. This scaling also satisfies the condition. The relative scale factor for $(a|a)$ of 0.85 and for $(b|b)$ of 1.18 is consistent, as $1/1.18 = 0.85$. The correction factor to $(a|a)$ of 0.85 is adopted. The uncertainty of the correction factor to $(a|a)$ is estimated to be 2% from the consistency with the scale factor for $(b|b)$.

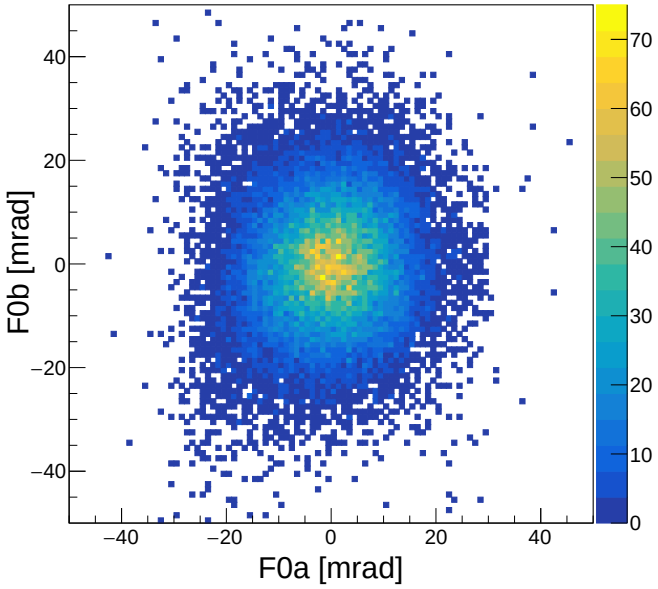

Figure 3.16: The reconstructed distribution of the horizontal angles and the vertical angles deduced with the original values of $(a|a)_{\mathrm{F0}\to\mathrm{F5}}$ and $(b|b)_{\mathrm{F0}\to\mathrm{F5}}$.

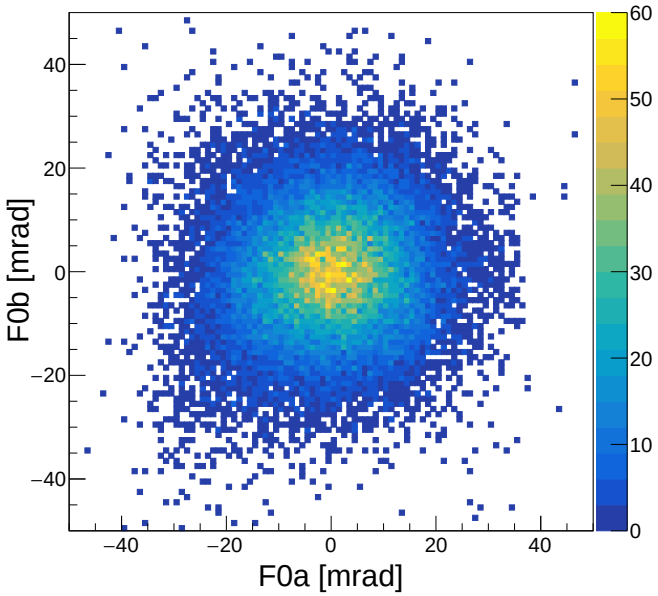

Figure 3.17: Same as Fig. 3.16 but the $(a|a)_{\mathrm{F0}\to\mathrm{F5}}$ is scaled by 0.85.

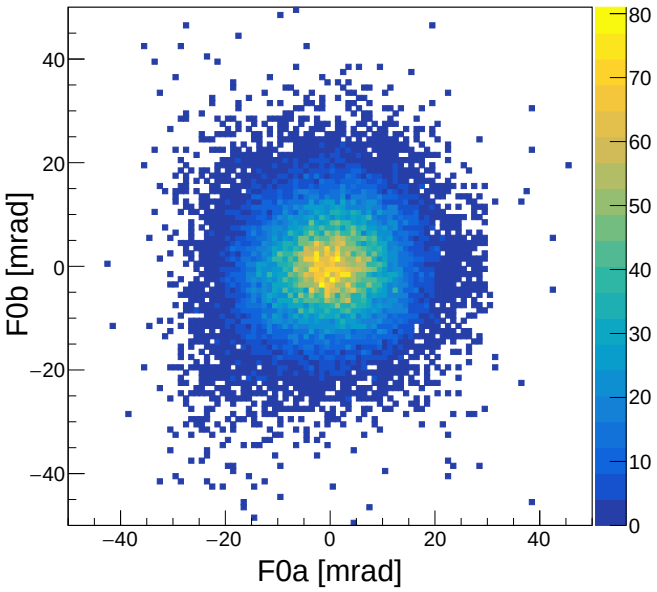

Figure 3.18: Same as Fig. 3.16 but the $(b|b)_{\mathrm{F0}\to\mathrm{F5}}$ is scaled by 1.18.

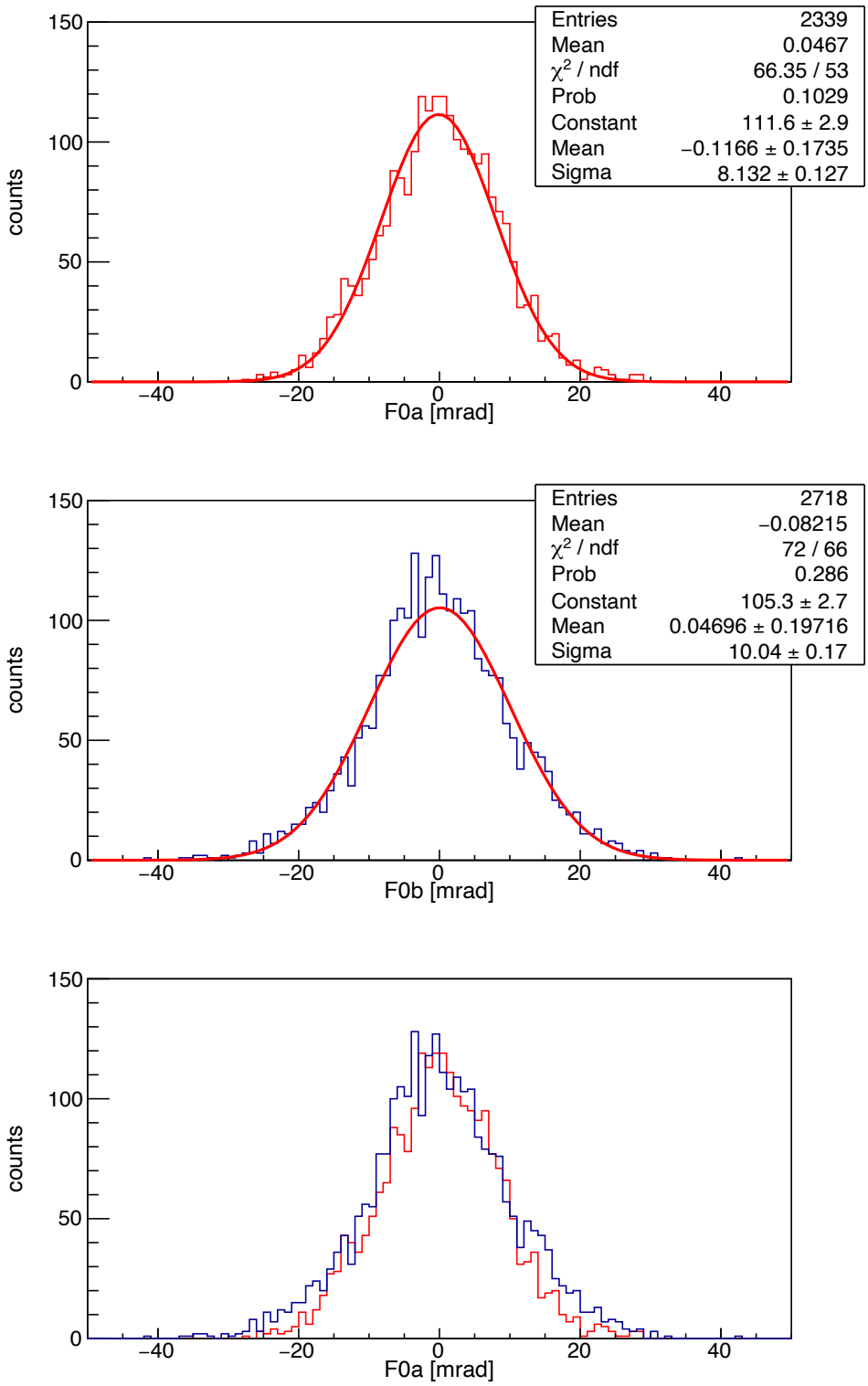

Figure 3.19: The projection of the reconstructed distribution of the horizontal angles and the vertical angles deduced with the original values of $(a|a)_{\mathrm{F0}\to\mathrm{F5}}$ and $(b|b)_{\mathrm{F0}\to\mathrm{F5}}$. Top panel: F0$a$, middle panel: F0$b$, bottom panel: F0$a$ an F0b are overlaid.

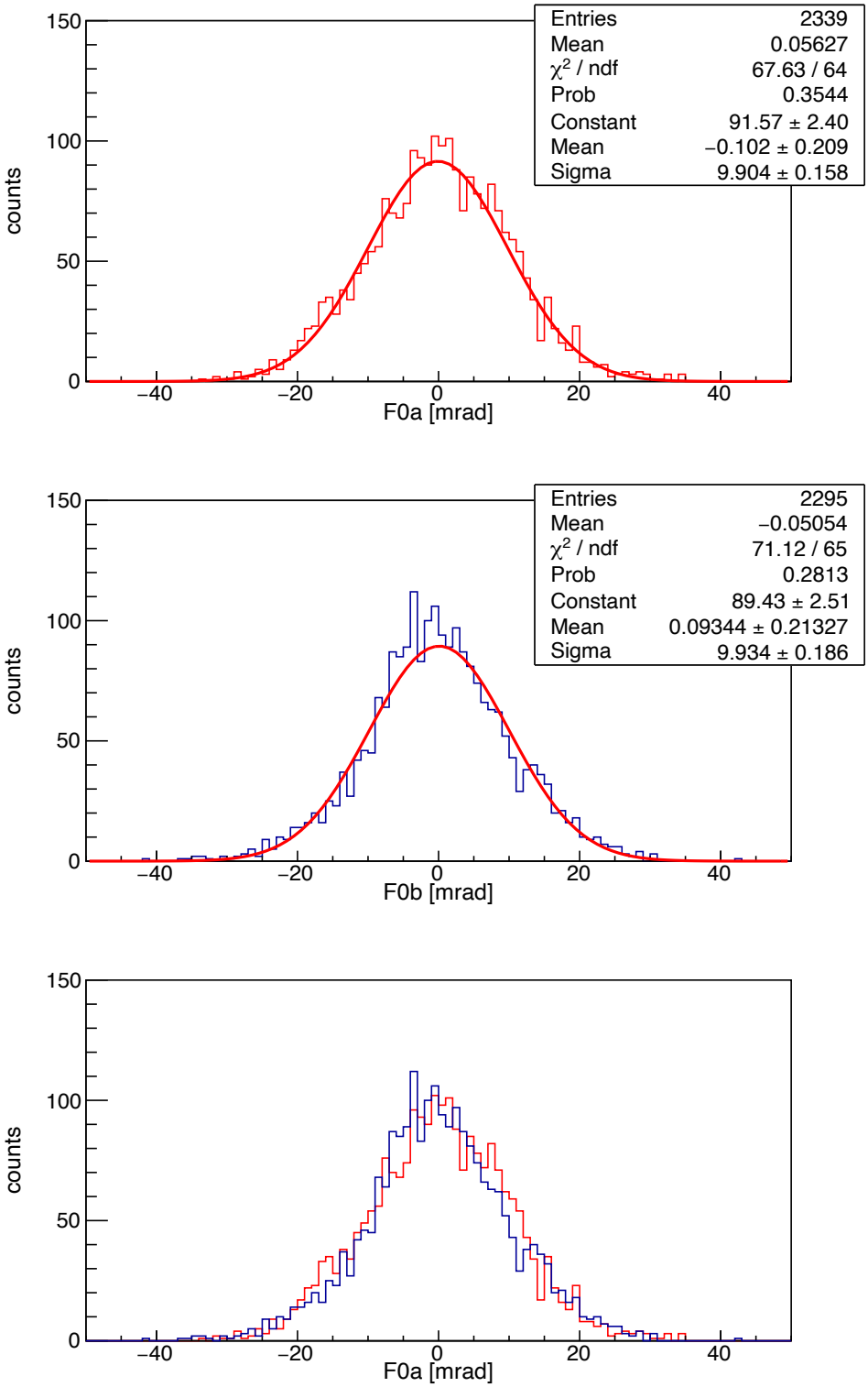

Figure 3.20: Same as Fig. 3.19 but the $(a|a)_{\mathrm{F0}\to\mathrm{F5}}$ is scaled by 0.85.

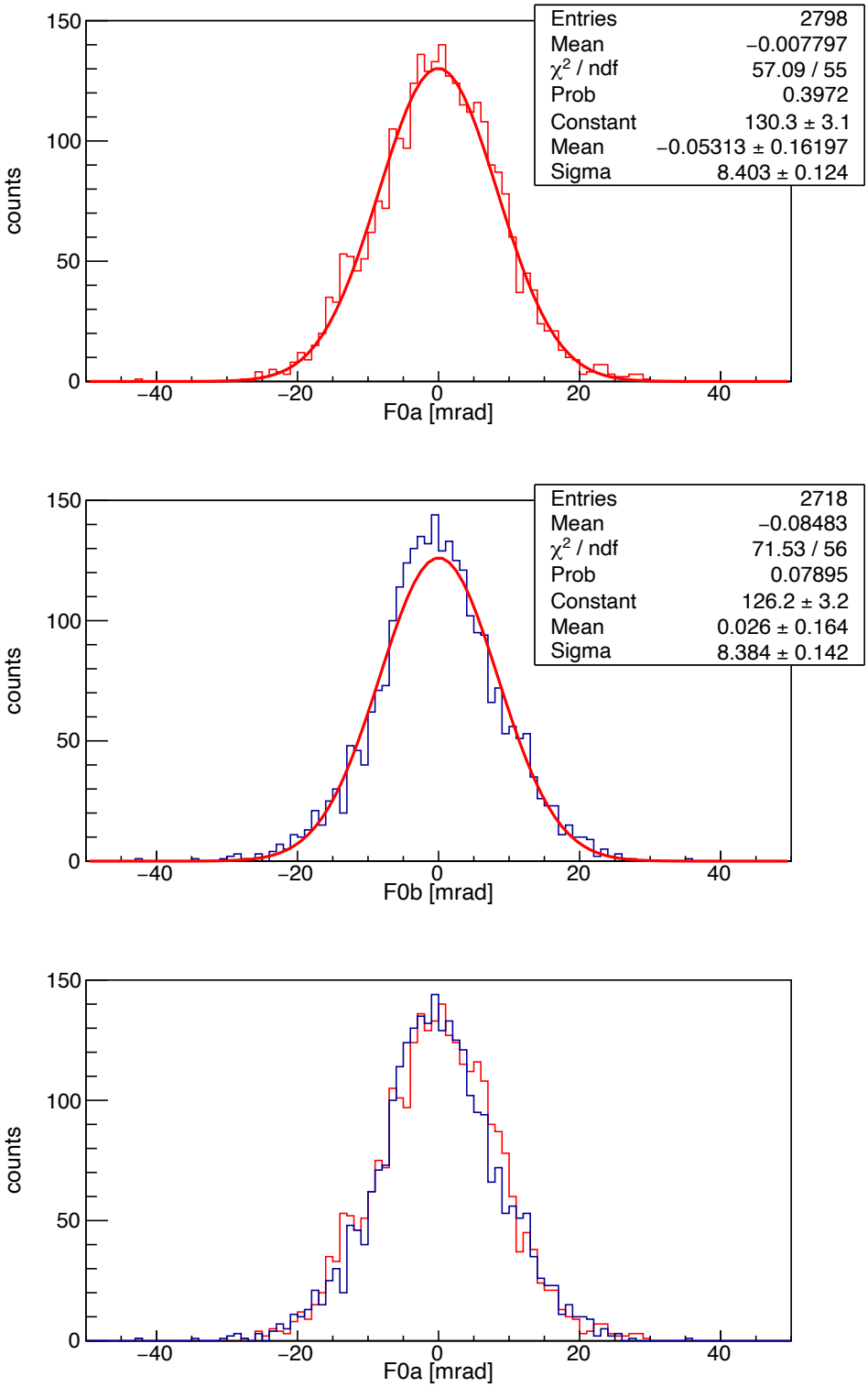

Figure 3.21: Same as Fig. 3.19 but the $(b|b)_{\mathrm{F0}\to\mathrm{F5}}$ is scaled by 1.18.

Constraint from kinematics of scattered particle

Another constraint can be made from the kinematic curve in the measurement of ^{12}C(^{12}C, ^{12}B)^{12}N$_{\mathrm{g.s.}}$ reaction. The dependence of the momentum of ^{12}B on the scattering angle is approximately quadratic. Figure 3.22 shows the position at F5 against the reconstructed scattering angles, F0b (top panel) and F0a (bottom panel) when the $(a|a)$ is multiplied by 0.85 by the original value. The loci corresponding to the ground state should be straight except for the aberration. The whole scale of $(a|a)$ and $(b|b)$ are scanned and determined so that the correlation between F5x and F0b to be straight. The scale factor of 1.15 is adopted in which the quadratic coefficient becomes 0 in the vertical direction as shown in the top panel of Fig. 3.23. The remaining correlation in the horizontal direction shown in the bottom panel of Fig. 3.23 is regarded as the second-order aberration. The uncertainty of the scale factor is estimated to be 4% which is the uncertainty of the determination where the quadratic coefficient becomes 0.

3.3.4 Errors in the reconstruction of the angles

The errors in the reconstruction of the scattering angles are attributed to the offset of the angles and $(a|a)_{\mathrm{F0}\to\mathrm{F5}}$ and $(b|b)_{\mathrm{F0}\to\mathrm{F5}}$. The error for the offset of the angle at F5 is 0.04° at maximum, which originates from the statistical error in the fit. The error of $(a|a)_{\mathrm{F0}\to\mathrm{F5}}$ is 6% considering the uncertainty in the relative scale determined by the constraints from the symmetry and the kinematics. The error of $(b|b)_{\mathrm{F0}\to\mathrm{F5}}$ is 4% considering the uncertainty in the relative scale determined by the constraints from the kinematics. The systematic error of the angle is evaluated as the quadratic sum of the errors of $(a|a)_{\mathrm{F0}\to\mathrm{F5}}$ and $(b|b)_{\mathrm{F0}\to\mathrm{F5}}$, 7%.

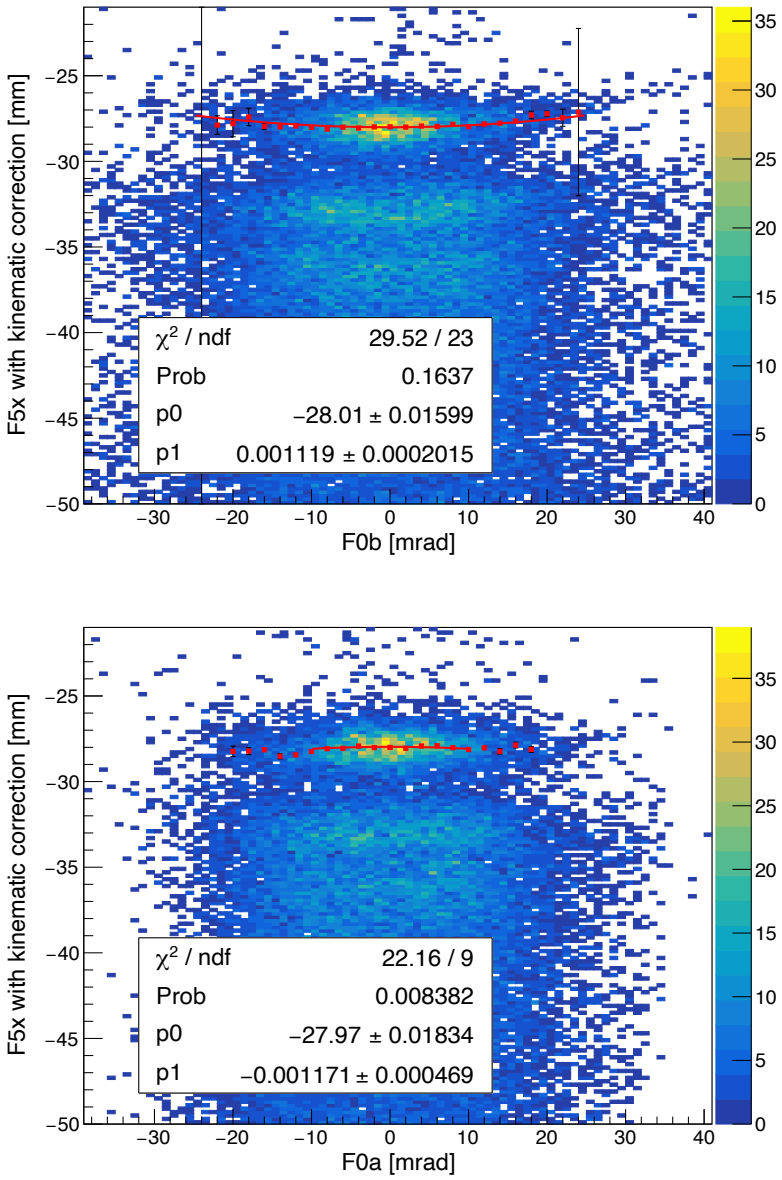

Figure 3.22: Correlation between the reconstructed angles at F0 and the horizontal position at F5 before correction of the scale. Top: correlation with the vertical angle F0*b*, bottom: the horizontal angle F0*a*.

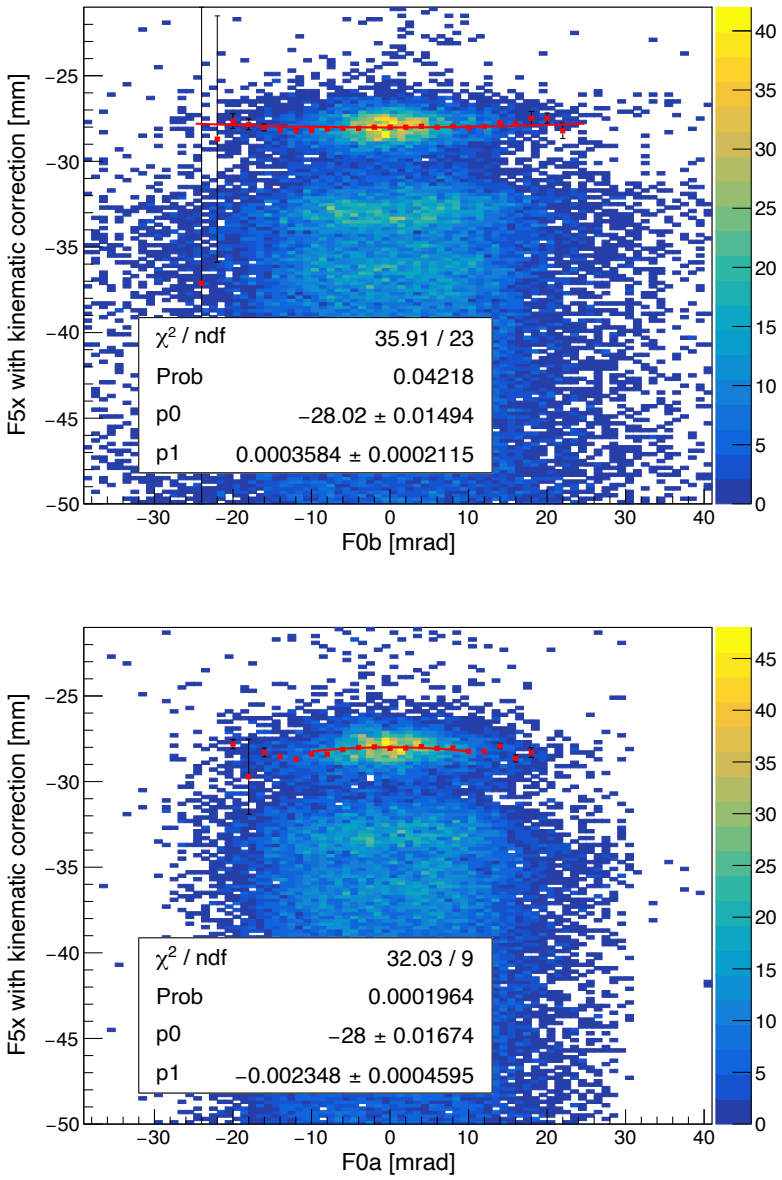

Figure 3.23: Correlation between the reconstructed angle and the horizontal position at F5 after correction of the scale. Top: correlation with the vertical angle F0*b*, bottom: the horizontal angle F0*a*.

3.3.5 Determination of dispersion between F0 and F5

The dispersion between F0 and F5 is determined from the measurements with scaling the magnetic fields from D1 to D4. The particle was ^{3}He produced via projectile fragmentation in a 25 mm thickness copper target. Figure 3.24 shows the δ which is corresponding the scaling of the magnetic field and the central positions of the ray. The dispersion is determined by fitting the correlation as 64.86 mm/%.

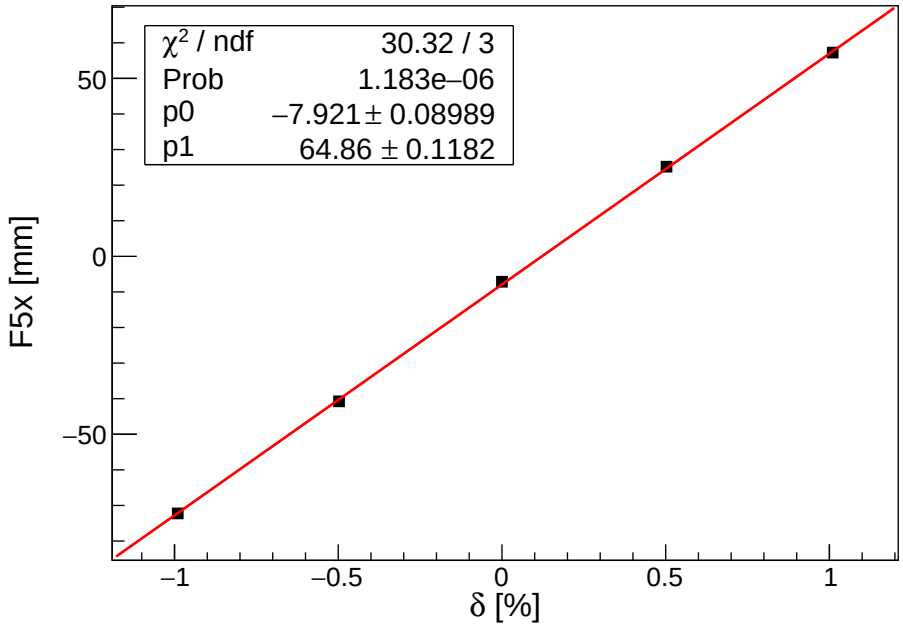

Figure 3.24: Correlation between F5x and δ.

3.4 Deduction of the excitation energy

The central value of the beam energy is determined to be 248.2 MeV/nucleon from the field strength of the D1 magnet given by the NMR probe. The momenta of the central ray of F0–F5 spectrometer in the DCX or SCX measurements were also evaluated from the NMR readout of D1.

The correspondence between the excitation energy in ^{48}Ti and the horizontal position at F5 was obtained. The position at F5 obtained from the tracking, F5x, is converted to F5x' in which the aberration due to the horizontal angle is corrected.

The momentum of ^{12}Be(0_2^+) corresponding to the excitation energy in ^{48}Ti $E_{\rm ex} = 0$ is calculated using the deduced beam energy of 248.2 MeV/nucleon. The reaction is assumed to occur at the center of the target and the energy loss in the target and the graphene were calculated using a code LISE++ [87]. δ was calculated from the calculated momentum and the central momentum of the spectrometer. δ was converted to the F5x' by multiplying the dispersion between F0 and F5.

The positions of F5x' corresponding $E_{\rm ex} = 10$ and 20 MeV were obtained in the same way. The correlation between F5x' and $E_{\rm ex}$ were approximated by a linear function and obtained the conversion function.

3.5 Evaluation of the experimental resolution and the check of the validity of the reconstruction

The validity of the conversion of the position to the momentum is checked using the single charge exchange reaction.

The energy calibration was checked using the peak position corresponding to some states observed in SCX. Figure 4.8 shows the horizontal position at F5 (F5x) in the SCX measurements with a gate of the forward angle, $\theta_{\rm lab} < 0.3^\circ$. In the ^{12}C(^{12}C, ^{12}B)^{12}N reaction, the ground state, 4.1 MeV in ^{12}N are identified. In the ^{48}Ca(^{12}C, ^{12}B)^{48}Sc reaction, 2.517 MeV in ^{48}Sc was identified. The peak position of these states are determined by Gaussian fitting. On the other hand, δ corresponding to these states are calculated from the reaction kinematics assuming the beam energy of 248.2 MeV/nucleon as determined in Sec. 3.4. The black points in Fig. 3.26 show the measured position F5x plotted against the corresponding δ. The blue circles show the measured F5x and δ in the measurement of the dispersion. The blue line shows the linear function with its slope of the dispersion which is adopted in the analysis. The blue line well reproduces the relation of the F5x and δ obtained in the SCX measurements. The deviation of the slope of the blue line from the black point is 3%, while the offset is 0.01% in δ which corresponds to 500 keV in kinetic energy. These are interpreted as a systematic error of the excitation energy.

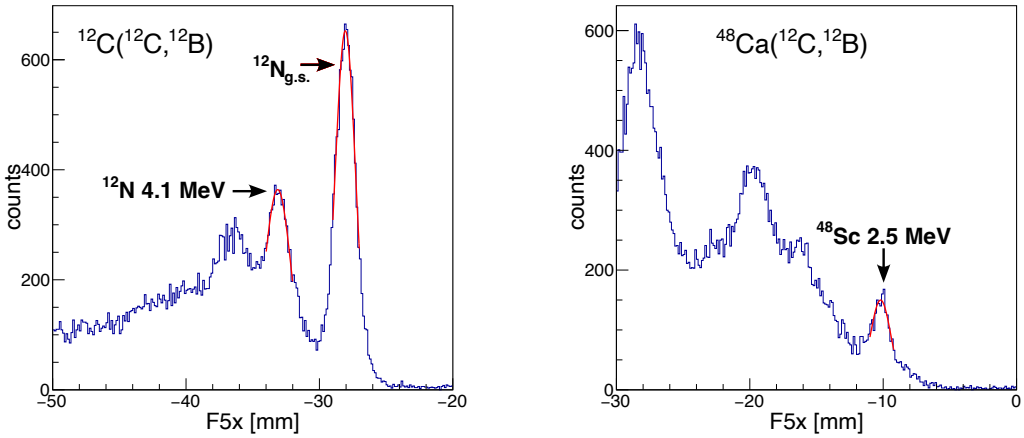

Figure 3.25: The horizontal position at F5 in several reactions in the forward angles.

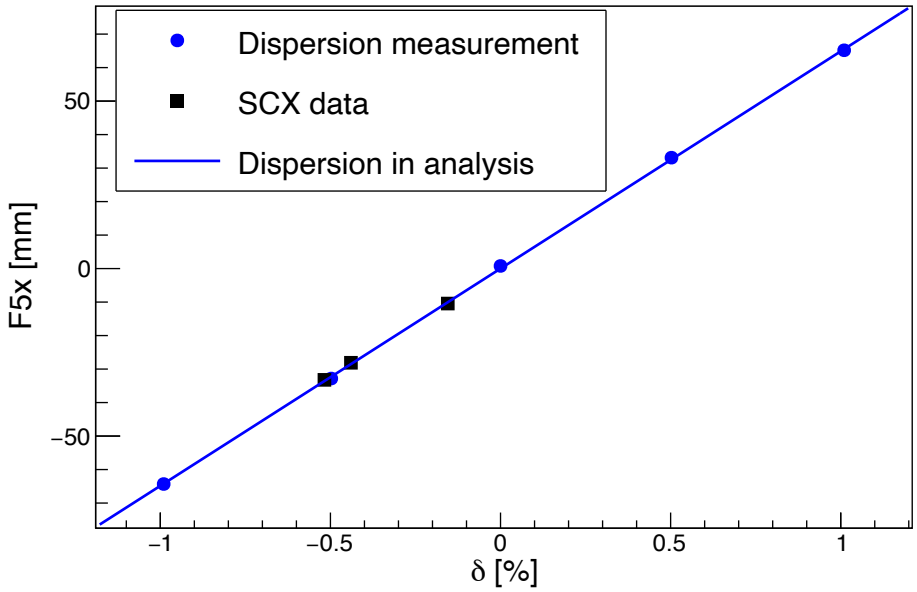

Figure 3.26: The horizontal position at F5 against corresponding δ in the SCX reaction (blue circles) and the dispersion measurement (black square). The blue line shows the dispersion relation adopted in the analysis.

The energy resolution was estimated considering the energy spread of the beam, the uncertainty of the reaction point in the target, and the resolution of the position determination by the tracking.

The position spread at F5 deriving from the beam spread is 1.7 mm (FWHM), as shown in Fig. 2.7 in Sec. 2.4.3. The spread is assumed to consist of the beam energy spread and the resolution of the position determination by MWDCs at F5. As the tracking resolution is evaluated as 0.24 mm (FWHM), the main contribution to the measured

spread of 1.7 mm is attributed to the beam. This corresponds to 1.4 MeV (FWHM) in the kinetic energy of ^{12}Be.

The contribution to the energy resolution of the ^{48}Ca target was evaluated from the energy loss difference calculated using LISE++. The difference of the energy loss in 10 mg/cm^2 of ^{48}Ca between as ^{12}C and as ^{12}Be is 530 keV. We assume the reaction point distribution is uniform and obtained 153 keV in σ, leading to 0.4 MeV in FWHM.

The resolution of the position determination by MWDCs is 0.24 mm (FWHM), and it corresponds to 0.2 MeV (FWHM).

The quadratic sum of these values leads to an excitation energy resolution of 1.5 MeV (FWHM).

The plausibility of the evaluation is checked by the consistency with the energy spread observed in the SCX measurement of ^{12}C(^{12}C, ^{12}B)^{12}N$_{\mathrm{g.s.}}$. The same evaluation is applied except for the energy loss in the target. The evaluated resolution is 1.5 MeV. The values are summarized in the table 3.1. This is consistent to the observed width in the SCX measurement as shown in Fig. 3.27.

Table 3.1: Contributions to the excitation energy resolution (FWHM)

	^{12}C(^{12}C, ^{12}B)^{12}N	^{48}Ca(^{12}C, ^{12}Be(0^+_2))^{48}Ti
beam energy	1.4 MeV	
F5 tracking resolution	0.2 MeV	
in-target energy loss difference	0.2 MeV	0.4 MeV
total resolution	1.4 MeV	1.5 MeV

The resolution of scattering angle θ_{lab} is estimated as 0.15° in horizontal and 0.17° in vertical directions considering the angular spread of the beam (0.15° (horizontal) and 0.16° (vertical)), the tracking resolution of the MWDCs (0.03° and 0.05°), and the multiple scattering in the target (0.008°).

3.6 Deduction of the double differential cross section

The double differential cross sections are obtained from the counts in an energy bin and an angular bin. The observed count is described as

$$\mathrm{count} = \frac{d\sigma}{d\Omega} \cdot N_{\mathrm{tgt}} \cdot N_{\mathrm{incident}} \cdot R_{\mathrm{surv.}} \cdot \epsilon_\gamma \cdot \epsilon_{\mathrm{trans}} \cdot \epsilon_{\mathrm{DAQ}} \cdot \epsilon_{\mathrm{tracking}} \cdot \epsilon_{\mathrm{PID}} \cdot d\Omega \tag{3.7}$$

The evaluations of the elements listed above and the accompanying errors are described below.

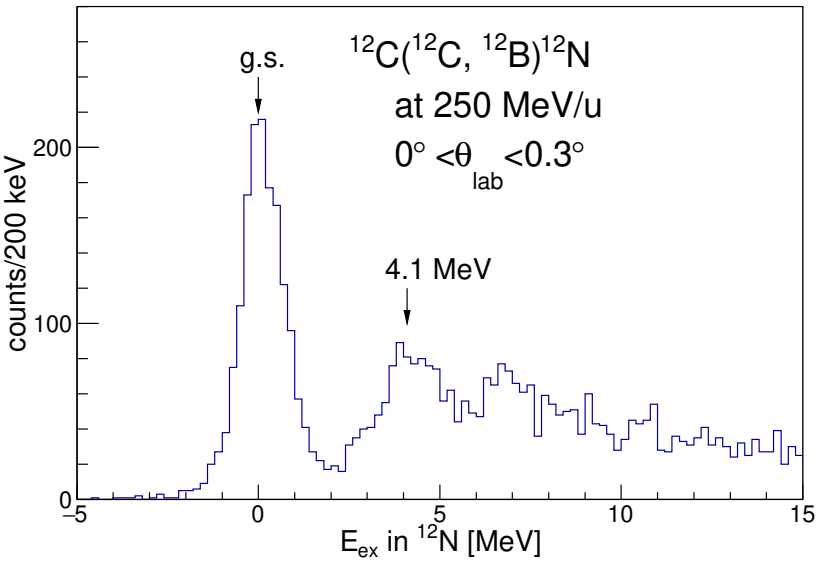

Figure 3.27: Excitation energy spectrum measured in the SCX reaction of ^{12}C(^{12}C, ^{12}B)^{12}N with graphene target.

Table 3.2: List of the elements in Eq. (3.7) with the mean values and relative errors.

		Mean value	Relative error
N_{target}	Number of target	1.23×10^{20} [cm^{-2}]	15%
N_{incident}	Incident particles	4.08×10^{17}	20%
ϵ_{PID}	PID efficiency	98%	0.7%
$\epsilon_{\text{tracking}}$	Tracking efficiency	78%	0.1%
ϵ_{trans}	Transmission	20%	20%
$R_{\text{surv.}}$	surviving ratio of ^{12}Be(0^+_2)	27%	4%
ϵ_{DAQ}	DAQ efficiency	88%	< 1%
ϵ_γ	tagging efficiency of ^{12}Be(0^+_2)	67%	15%
$d\Omega$	Solid angle	-	7%

Target thickness

We adopted the nominal value of the target. The isotope enrichment is 95.23%. The uncertainty in the thickness is taken as 15% corresponding to uncertainty in the thickness measurement (area and weight) as well as the unevenness within the beam spot.

Incident particles

The total number of the incident particles is evaluated from the count of the coincidence of three scintillators. The error for the relation between the beam intensity and the count of

the coincidence is 4% as shown in Sec. 2.2. The uncertainty of the absolute value depends on the uncertainty of the measurement by the Faraday cup, which has 20% uncertainty relatively. Thus the uncertainty in N_{incident} is evaluated to be 20%.

Transmission

The loss of ejected $^{12}\text{Be}(0_2^+)$ between F0 and F8 is due to the acceptance of the beam line and the reaction with materials, mainly degraders. The loss due to the acceptance between F0 and F7 is studied by the simulation using LISE++ code [87] and found to be negligible in the spatial region used in the analysis. The reaction loss between F0 and F7, upstream of the aluminum degrader, is attributed to the loss in the degrader at F5 and is estimated with LISE++ as the ratio of the number of surviving particles comparing to that of incoming particles. Thus the transmission between F0 and F7 is evaluated to be 85% as shown in the first row in Table. 3.3. Similarly, the reduction after passing the degraders of the 14.875-mm aluminum and the 33-mm copper at F7 are also calculated with LISE++. Table 3.3 shows the result of the simulated transmission at each of three degrarders.

Table 3.3: Simulated ratio of ^{12}Be surviving after passing through the energy degraders. Here only the reaction loss is considered.

Material	ratio to number of generated particle
F5 copper 10 mm	0.85
F7 aluminum 14.875 mm	0.75
F7 copper 23 mm	0.51

The transmission between F7 and F8 including the effect of the acceptance and the reaction is evaluated from the event numbers counted in the plastic scintillator at F7 and the PPAC at F8. The vertical axes of Fig. 3.28 show the ratio of the event number counted at F7 and F8. The horizontal axes show the position or the angle at F7. In the analysis, we use the region of angles at F0 with F0a $< 0.9^\circ$ and F0b $< 1.5^\circ$, which correspond to the angles at F7, F7a $<$ 16 mrad and F7b $<$ 10 mrad. In that region, the averaged transmission is 27 ± 4%.

The transmission between F0 and F8 is evaluated by multiplying the transmission of F0–F7 and F7–F8.

The uncertainty in the estimation of the reaction loss by LISE++ is the dominant uncertainty in the evaluation of the transmission. The reaction loss between F7 and F8 estimated by LISE++ differs from the measured one by a factor of 0.5. If the estimation for the reaction loss at the degrader at F5 by LISE++ underestimates by 0.5 likewise, the actual loss at F5 should be 30% and the transmission between F0 and F5 is 70%. Considering along with the evaluated transmission between F7 and F8, the transmission between F0 and F8 is considered to be within the range of 16%–24%. Thus the transmission between F0 and F8 is evaluated to be 20 ± 4%.

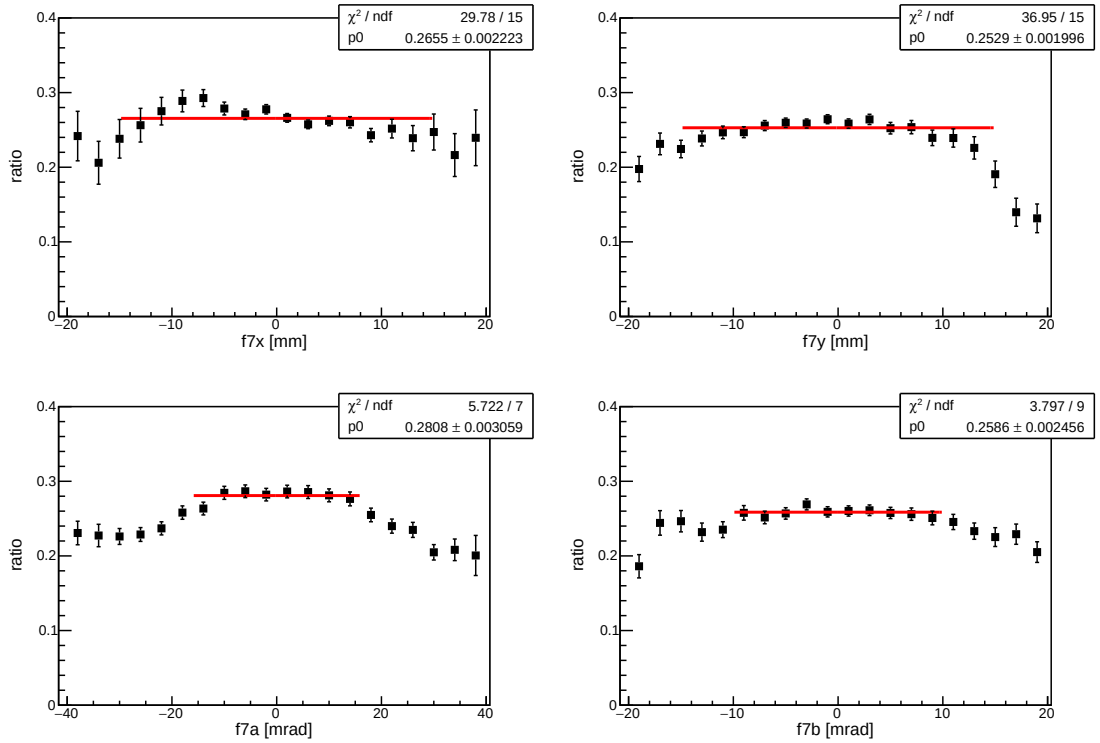

Figure 3.28: Position and angular dependence of the transmission between F7 and F8. Dependence on the horizontal position at F7, F7x (top left), the vertical position F7y (top right), the horizontal angle F7a (bottom left), and the vertical angle F7b (bottom right).

Surviving ratio of ^{12}Be(0^+_2)

The reduction of the isomeric state arriving at F8 due to its lifetime is evaluated from the time of flight from F0 to F8.

Table 3.4: The energy of ^{12}Be(0^+_2) in each period, flight length, flight time and the ratio between the start and the end at the period. The energy losses in the degraders at the boundary of the period are considered.

	^{12}Be(0^+_2) energy [MeV/nucleon]	γ factor	flight length [m]	flight time [ns]	ratio
F0 to F5	254.64	1.26	54.916	299.602	0.49
F5 to F7	212.39	1.23	23.283	133.810	0.72
F7 to F8	83.40	1.10	11.300	92.107	0.78
F0 to F8					0.273

The main uncertainty comes from the value of the lifetime, $\tau = 330 \pm 12$ ns [58]. The survival ratio is $27.3 \pm 1.0\%$.

Identification of the ^{12}Be

The number of the ^{12}Be events has uncertainties in the gate with PPAC at F8 and the selection using the charge information.

The efficiency of the PPAC at F8 is evaluated from the detected number of events of the two sets of PPACs at F8. We assume that the hits are independent each. We used the upstream one to gating the events. Its efficiency is evaluated as 98 ± 0.7%. The selection by the charge in the MWDC2 at F5 and the scintillator at F7 is described in Sec. 3.1.1 The number of selected events by the charge is to be corrected by 0.4% due to the contamination of ^{9}Li and the loss of ^{12}Be. The error for this value is relatively 1% and negligible. Considering the efficiency of the PPAC along with the selection of the charge, the error of the estimation of the number of ^{12}Be is 0.7%.

Tracking efficiency

The events in which the quality of the tracking is sufficient are adopted for the analysis. The events in which the χ^2 defined as Eq. 3.1 is within a limit. The limit is set to 1600, and the number of the adopted events is 78% of the total number of ^{12}Be. The possible error for the number of adopted events is the contamination of the events other than ^{12}Be in the total number or the adopted events. Considering the possibility that the rejected events have a bias to the noise event such as ^{9}Li, the error for the number of the adopted events is estimated to be 0.1% at maximum.

Tagging efficiency of ^{12}Be(0^+_2)

As described in sec. 3.1.3, the tagging efficiency of ^{12}Be(0^+_2) by detecting the γ-rays is 67 ± 10%.

DAQ efficiency

The efficiency due to the DAQ dead time is evaluated from the numbers of accepted events and the requested events is 88%. The miss counting is estimated < 1%.

Solid angle

The cross sections are derived in each region of the angles in the center of mass frame, $\theta_{\rm CM}$ = 0°–0.3°, 0.3°–0.5°, and in 0.2° intervals for large angles up to $\theta_{\rm CM}$ = 1.9°. These angles correspond to the angles in the laboratory system $\theta_{\rm lab}$ = 0°–0.23°, 0.23°–0.35°. $\theta_{\rm lab}$ are calculated from the F0*a* and F0*b*, and the events in each angular region are selected

by gating the corresponding F0a and F0b. Because the vertical angular acceptance is larger than the horizontal one, the selection of the events with the horizontal angle is up to $\theta_{\mathrm{CM}} < 1.2^\circ$ which correspond to $\theta_{\mathrm{lab}} < 0.92^\circ$. The error of the solid angles is attributed to the uncertainty of the reconstruction of the angles at F0 from the trajectories at F5. This is determined by the uncertainty of the $(a|a)_{\mathrm{F0}\to\mathrm{F5}}$ and $(b|b)_{\mathrm{F0}\to\mathrm{F5}}$, which is 7% as described in Sec. 3.3.

3.6.1 Deduction of the differential cross sections

The blue histograms in Fig. 3.29 show the differential cross sections deduced from the observed counts in each angular bin against the excitation energy in ^{48}Ti for the (^{12}C, ^{12}Be(0^+_2)) reaction. The cross sections are calculated in the center of mass frame with nine angle steps of $\theta_{\mathrm{CM}} = 0^\circ$–$0.3^\circ$, 0.3°–0.5°, and in 0.2° intervals for large angles up to $\theta_{\mathrm{CM}} = 1.9^\circ$. Here only the statistical errors are shown. The total systematic uncertainty in the absolute value of the cross section is evaluated by taking the quadratic sum of the contributions listed in Table 3.2, as 36%.

3.6.2 Contribution from accidental coincidence

The distribution of the accidental coincidence events with room-background γ-rays is evaluated from the ^{12}Be singles spectra without the coincidence with DALI2. The numbers of the events are evaluated from the number in the time region of -400 ns before the prompt γ-rays. The distribution of the accidental coincidence events are shown in the red histograms in Fig. 3.29. Figure 3.31 shows the spectra in which the contribution of the accidental coincidence background is subtracted.

3.6.3 Contribution from graphene sheets

The contribution from the graphene sheets attached to the ^{48}Ca foil is evaluated from the measurement with the graphene target with the thickness of 36 μm. Figure 3.30 shows the excitation energy distributions of the observed counts in the measurement with the ^{48}Ca target (blue histogram) and the graphene target (red histogram). Here the histograms with the graphene target is scaled with the number of the injected particles and the thickness of the graphene sheet. The contribution is negligible at $E_{\rm ex} < 34$ MeV because the Q-value of the ^{12}C(^{12}C, ^{12}Be(0^+_2))^{12}O$_{\rm g.s.}$ is -59.3 MeV corresponding to an excitation energy of 36.5 MeV. In the region of $E_{\rm ex} = 34$–50 MeV, the contribution amounts to $6 \pm 2\%$ of the spectra.

3.7 Results of the measurement of cross sections of the (^{12}C, ^{12}Be(0^+_2)) reaction

Figure 3.31 shows the spectra of the cross section in which the contribution of the accidental coincidence background is subtracted. Figure 3.32 shows the angular distribution at every 4-MeV energy bin. In Fig 3.32, the accidental coincidence background is not subtracted and is shown in hatched histograms. In both Fig. 3.31 and Fig. 3.32, the background from the graphene that contributes $E_{\rm ex} > 35$ MeV is not subtracted.

The double charge exchange processes with double spin and isospin flips have been identified at the energy region which can not be populated by the double β decays, using the nuclear reaction at the incident energy of 250 MeV/nucleon. When compared with the pilot experiment at RCNP [65], the quality of the data has improved in terms of statistical significance by 2.5 times. It is partly because of the low-background detection of γ-rays thanks to rejection of tritons and other light particles in the F5–F7 magnetic system and to the use of the ^{9}Be stopper which hardly produce long-lived β^+ emitters. They resulted in an improvement of the true-to-accidental ratio from 1:1 at RCNP to 9:1 in the present work.

The improvements in the statistics allowed us to observe enhancements at 14–22, 26–30, and 34–42 MeV at the most forward angle of 0–0.3°. The forward peaking angular distributions suggest that the $\Delta L = 0$ transition components exist in the region. The integrated cross section over 0–34 MeV where the background from graphene does not contribute is 1.33 ± 0.12 μb/sr at the angular range of $\theta_{\rm CM} = 0°$–0.3°. In addition, even more prominent structure was found in 34–40 MeV at 0–0.3°.

In the following chapter, the DGT transition strengths included in the observed cross sections will be discussed more quantitatively with the help of the coupled-channel distorted -wave Born approximation.

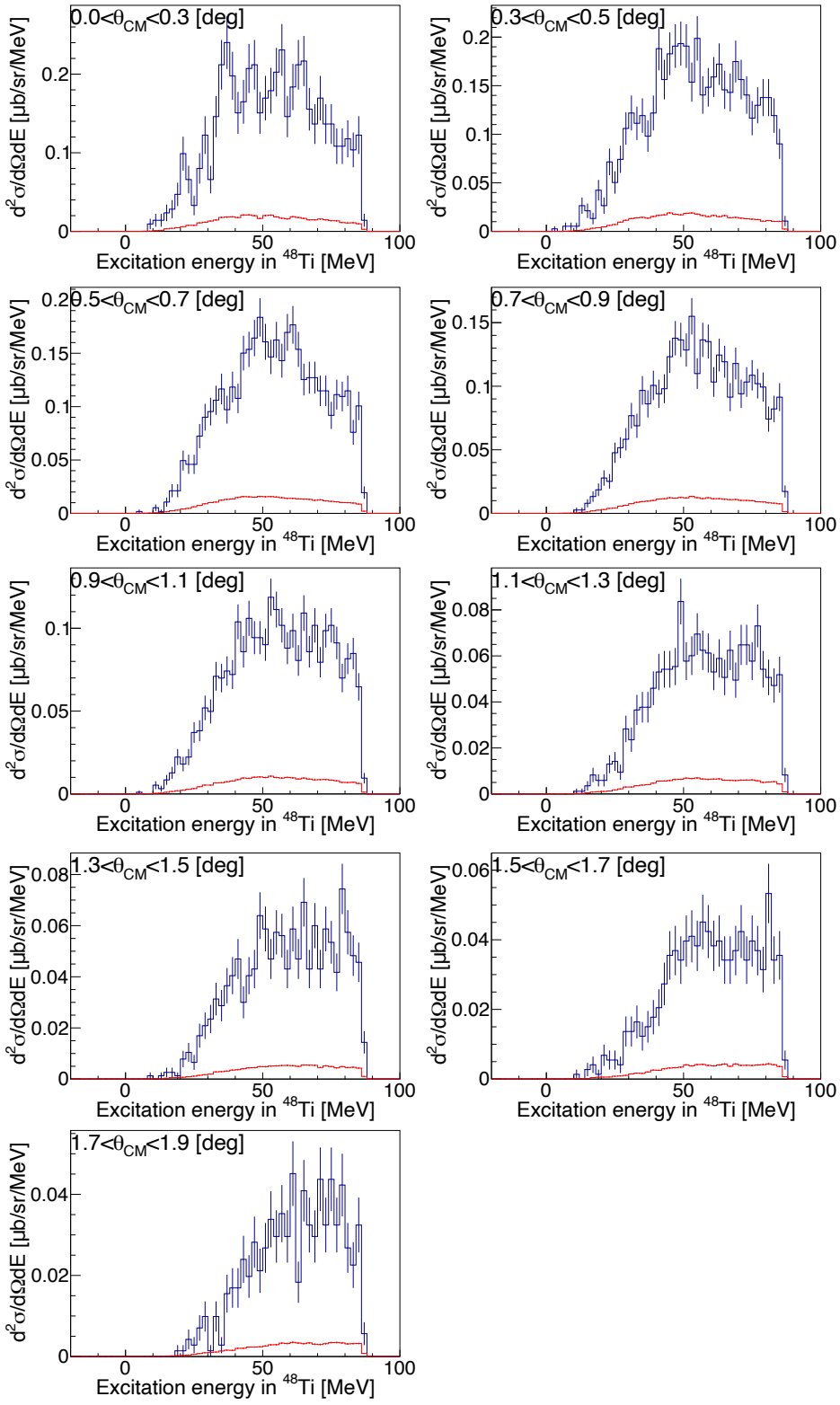

Figure 3.29: Double-differential cross sections of the ^{48}Ca(^{12}C, ^{12}Be(0^+_2))^{48}Ti reaction against the excitation energy in ^{48}Ti for each angle (blue histograms). Each panel shows the cross section at 0.0–0.3° (top left), 0.3–0.5° (top right), and follows in 0.2° interval from top to bottom. Red histograms show the contribution of the accidental coincidence events.

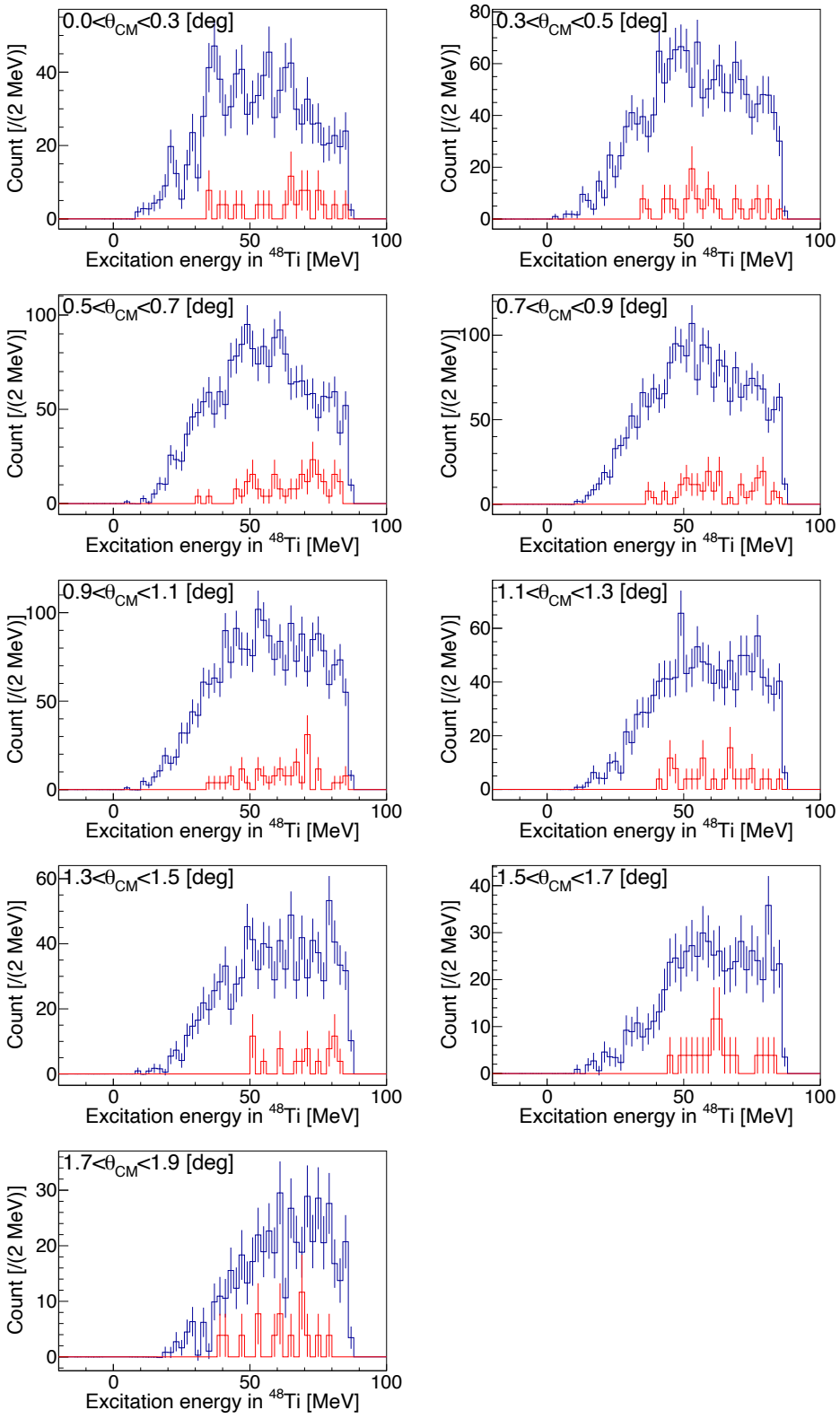

Figure 3.30: The excitation energy distribution of the observed count in the measurement with the ^{48}Ca target (blue histograms) and the graphene target (red histograms), respectively. Red histograms are scaled with the number of the incident particles and the thickness of the target and the coating.

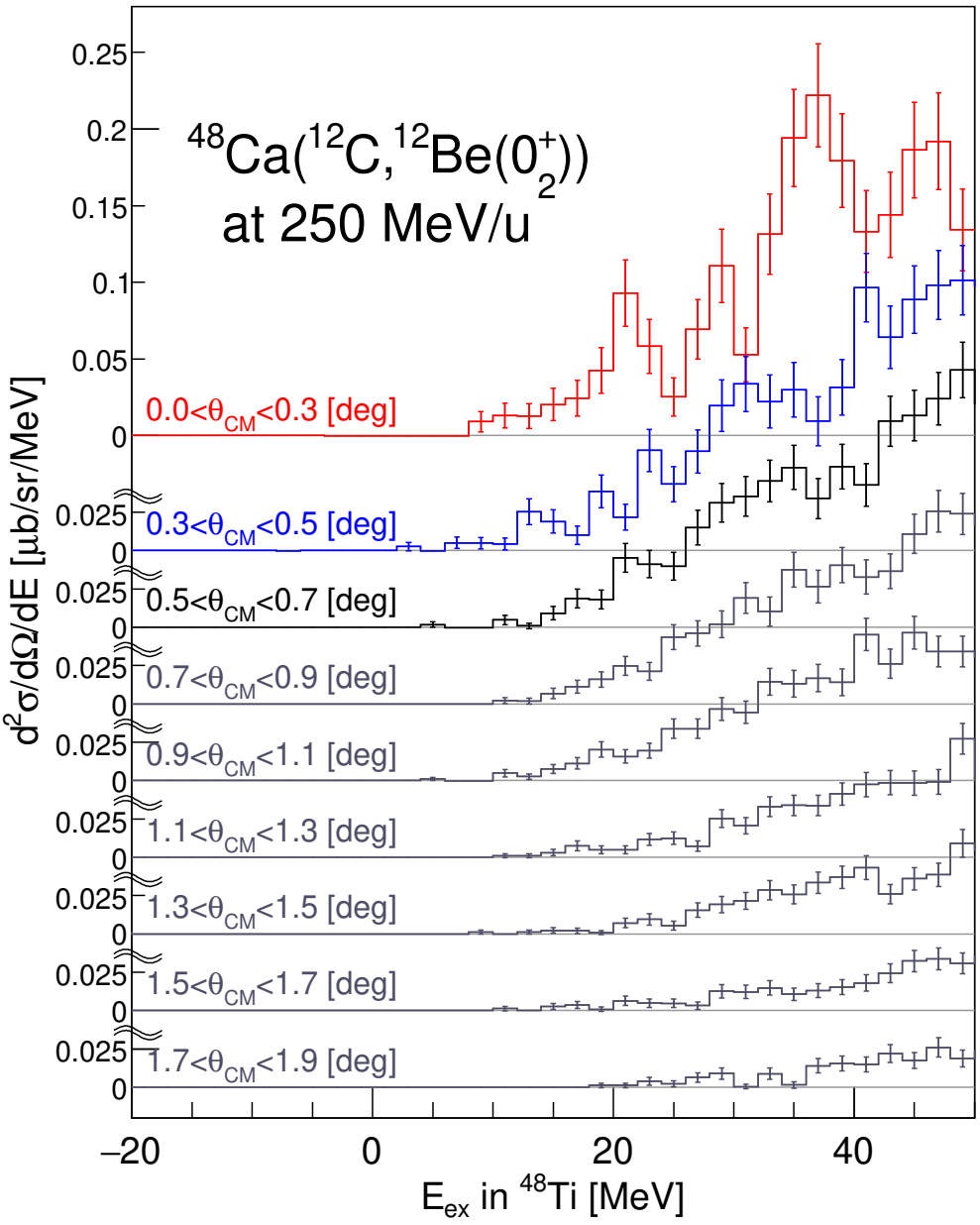

Figure 3.31: Double-differential cross sections of the ^{48}Ca(^{12}C, ^{12}Be(0^+_2))^{48}Ti reaction against the excitation energy in ^{48}Ti for each angle from 0.0° to 1.9°.

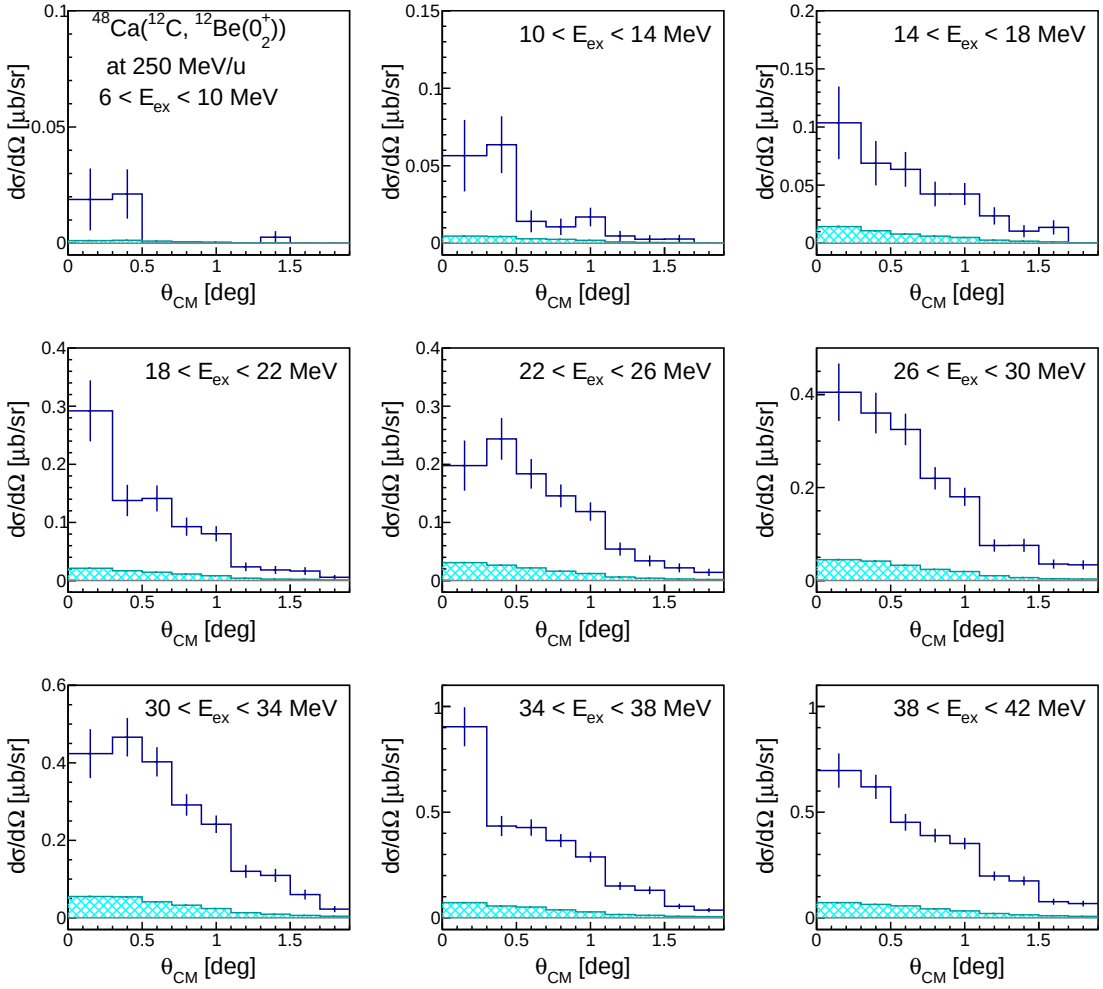

Figure 3.32: Observed angular distribution in the ^{48}Ca(^{12}C, ^{12}Be(0^+_2))^{48}Ti reaction at each excitation energy (histograms with blue outlines). Distributions with the accidental coincidence events are shown in hatched histograms.

Chapter 4

Expected angular distribution of DGT

For a quantitative argument on the existence of the DGTGR, the cross section spectra are compared to the coupled channel calculations. In this chapter, the derivation of the expected angular distribution will be described.

4.1 Outline of the reaction calculation

The double charge exchange ^{48}Ca(^{12}C,^{12} Be(0^+_2))^{48}Ti reaction is described as a two-step transition : $^{48}\mathrm{Ca}_{\mathrm{gnd}}(0^+) \rightarrow {}^{48}\mathrm{Sc}(1^+) \rightarrow {}^{48}\mathrm{Ti}(0^+)$ in the target and $^{12}\mathrm{C}_{\mathrm{gnd}}(0^+) \rightarrow {}^{12}\mathrm{B}(1^+) \rightarrow {}^{12}\mathrm{Be}(0^+_2)$ in the projectile. Reaction calculations are carried out using ECIS97, by solving the coupled channel equation with the three channels,

Initial channel	$^{48}\mathrm{Ca}_{\mathrm{gnd}}(0^+) + {}^{12}\mathrm{C}_{\mathrm{gnd}}(0^+)$
Intermediate channel	$^{48}\mathrm{Sc}(1^+) + {}^{12}\mathrm{B}(1^+)$
Final channel	$^{48}\mathrm{Ti}(0^+) + {}^{12}\mathrm{Be}(0^+_2)$

4.1.1 Coupled channel equation

The coupled-channel wave function of the system Ψ is assumed to be expressed as

$$\Psi = \Psi_0(\xi_{A;0}, \xi_{a;0}, \boldsymbol{R}_0) + \Psi_1(\xi_{A;1}, \xi_{a;1}, \boldsymbol{R}_1) + \Psi_2(\xi_{A;2}, \xi_{a;2}, \boldsymbol{R}_2) \quad (4.1)$$

$$= \chi_0(\boldsymbol{R}_0)\phi_0(\xi_{a;0})\Phi_0(\xi_{A;0}) + \chi_1(\boldsymbol{R}_1)\phi_1(\xi_{a;1})\Phi_1(\xi_{A;1}) + \chi_2(\boldsymbol{R}_2)\phi_2(\xi_{a;2})\Phi_2(\xi_{A;2}) \quad (4.2)$$

where $\Psi_c(\xi_{A;c}, \xi_{a;c}, \boldsymbol{R}_c)$ denotes the wave function in the channel c ($c = 0$: initial, $c = 1$: intermediate, and $c = 2$: final). The wave function of each channel can be written as a product of the distorted wave χ_c as a function of the relative coordinate $\boldsymbol{R}_c$ of the projectile and the target, and the internal wave functions of the projectile $\phi_c(\xi_{a;c})$ and the target $\Phi_c(\xi_{A;c})$ with their internal coordinate $\xi_{a;c}$ and $\xi_{A;c}$ as variables. In the present case where

there is no mass transfer between the projectile and the target, one can drop the channel suffix of $\boldsymbol{R}_c$, $\xi_{a;c}$, and $\xi_{Ai;c}$. In the following, $\boldsymbol{R}$, ξ_a, ξ_A, defined in Fig. 4.1, are used for the relative and internal coordinates of the projectile and the target in all the channels.

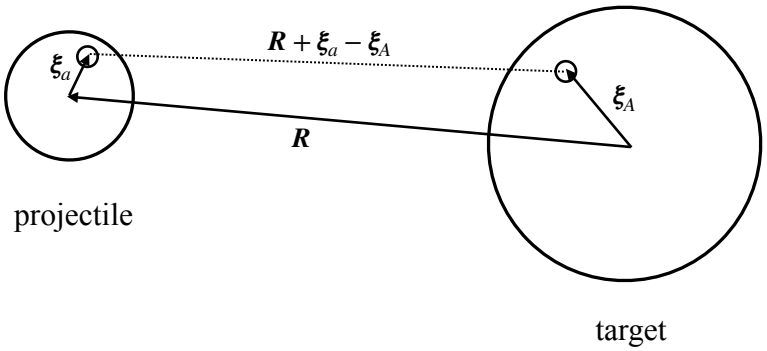

Figure 4.1: Coordinate in the heavy-ion reactions.

The Hamiltonian of the system can be written as

$$\mathcal{H} = \mathcal{H}_{\rm rel}(R) + \mathcal{H}_{\rm prj}(\xi_a) + \mathcal{H}_{\rm tgt}(\xi_A)\,, \tag{4.3}$$

where

$$\begin{aligned}
\mathcal{H}_{\rm rel}(R) &= \hat{T}_R + U_{\rm rel}(R) + V'_{\rm rel}(R) && (4.4)\\
\mathcal{H}_{\rm prj}(\xi_a) &= \mathcal{H}_{\rm prj;0}(\xi_a) + v_{cc'}(\xi_a)\,, && (4.5)\\
\mathcal{H}_{\rm tgt}(\xi_A) &= \mathcal{H}_{\rm tgt;0}(\xi_A) + V_{cc'}(\xi_A)\,. && (4.6)
\end{aligned}$$

The first and second terms in Eq. (4.4) are the kinetic-energy and diagonal potential terms for the relative motion of the projectile and the target, while the third term represents the off-diagonal term that induces the transition between the channels. The internal Hamiltonians for the projectile (Eq. (4.5)) and the target (Eq. (4.6)) consist of the diagonal terms ($\mathcal{H}_{\rm prj;0}(\xi_a)$ and $\mathcal{H}_{\rm tgt;0}(\xi_A)$) and the off-diagonal terms ($v_{cc'}(\xi_a)$ and $V_{cc'}(\xi_A)$). The diagonal terms satisfy the Schödinger equations as

$$\begin{aligned}
\mathcal{H}_{\rm prj;0}(\xi_a)\phi_c(\xi_a) &= \varepsilon_c\phi_c(\xi_a) && (4.7)\\
\mathcal{H}_{\rm tgt;0}(\xi_a)\Phi_c(\xi_A) &= E_c\Phi_c(\xi_A)\,, && (4.8)
\end{aligned}$$

where ε_c and E_c are the internal energies of the projectile and the target in the channel c. The off-diagonal terms in Eqs. (4.5) and (4.6) cause the transition between the channels. It is assumed that the double charge exchange process always proceeds through the intermediate channel and thus

$$v_{02}(\xi_a) = v_{20}(\xi_a) = V_{02}(\xi_A) = v_{20}(\xi_A) = 0 \tag{4.9}$$

The scattering wave functions of the channels can be obtained by solving the coupled channel equation

$$(\mathcal{H} - E_{\rm total})\Psi = 0\,. \tag{4.10}$$

In the present case, however, the transitions between the channels are relatively weak and it is sufficient to consider contributions from the Born terms as

$$\begin{aligned} T_{20} &= T_{21}\mathcal{G}_1 T_{10} && (4.11)\\ &= \langle\Psi_2|\tilde{V}_{21}|\Psi_1\rangle\mathcal{G}_1\langle\Psi_1|\tilde{V}_{10}|\Psi_0\rangle\,, && (4.12)\end{aligned}$$

where $\mathcal{G}_1$ is the Green's function in the channel 1 and $\tilde{V}$ is the interaction that causes the transition between the channels. The explicit expression of $\tilde{V}$ is discussed later. The double charge exchange cross section from the channel 0 to 2 is calculated as

$$\frac{d\sigma}{d\Omega} = \left(\frac{\mu}{2\pi\hbar^2}\right)^2 \frac{k_f}{k_i}|T_{20}|^2\,, \tag{4.13}$$

where μ is the reduced mass and k_i (k_f) is the relative momentum in the initial (final) channel.

4.1.2 Procedure of numerical calculations

Figure 4.2 shows the schematic diagram of the calculation. The cross section is calculated by using ECIS97 [88]. The transition amplitude in each step is calculated as

$$\begin{aligned} T_{c'c} &= \langle\Psi_{c'}|\tilde{V}_{c'c}|\Psi_c\rangle && (4.14)\\ &= \int d\boldsymbol{R}\,\chi^{(-)}_{c'}(\boldsymbol{R})\chi^{(+)}_{c}(\boldsymbol{R}) \int d\boldsymbol{\xi}_a d\boldsymbol{\xi}_A V'_{c'c}(\boldsymbol{R},\boldsymbol{\xi}_a,\boldsymbol{\xi}_A)\,(\Phi_{c'}|V_{c'c}|\Phi_c)\,(\phi_{c'}|v_{c'c}|\phi_c) && (4.15)\\ &\equiv \int d\boldsymbol{R}\,\chi^{(-)}_{c'}(\boldsymbol{R})\chi^{(+)}_{c}(\boldsymbol{R})F_{c'c}(\boldsymbol{R})\,. && (4.16)\end{aligned}$$

The integrand in Eq. (4.16) is a product of the distorted waves in channels c and c', and the transition form factor $F_{c'c}$. Thus, for the calculations, one needs

- Optical potentials for calculations of the distorted waves
- Transition form factors for the transition 0$\longrightarrow$1 and 1$\longrightarrow$2.

In Sec. 4.3, the optical potentials used in the calculation are described. As is shown in Fig. 4.2 and discussed in Sec. 4.2, the transition form factor is obtained by double-folding the effective interaction with transition densities in the projectile and the target, using a code of FOLD [89].

In the following sections, how to obtain the elements is described.

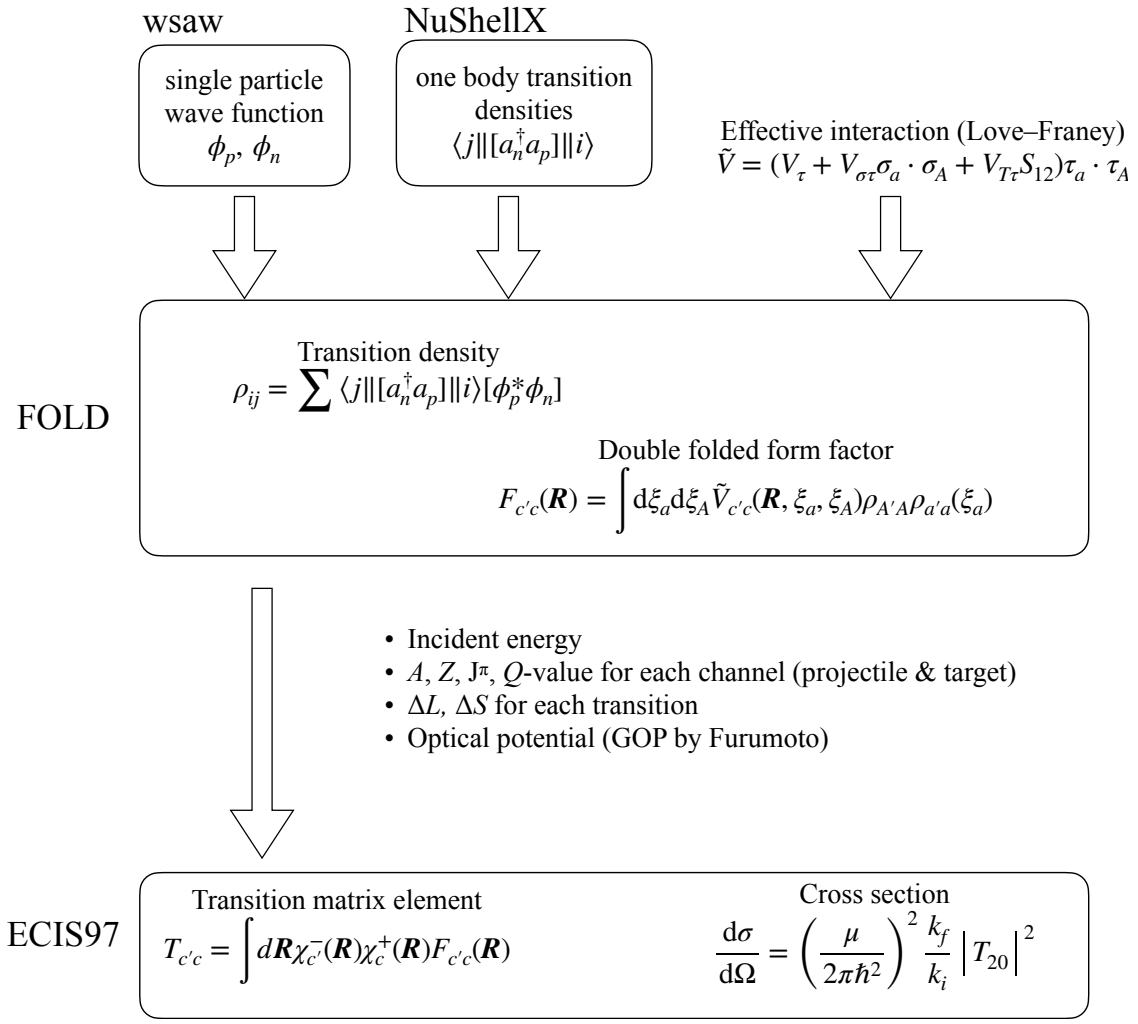

Figure 4.2: Outline of the calculation.

4.2 Transition Form Factor

In the present case where both the projectile and the target are heavy ions with internal structures, the transition form factors are calculated by double folding as

$$F_{c'c}(\boldsymbol{R}) = \int d\boldsymbol{\xi}_a d\boldsymbol{\xi}_A V'_{c'c}(\boldsymbol{R}, \boldsymbol{\xi}_a, \boldsymbol{\xi}_A)\,(\Phi_{c'}|V_{c'c}|\Phi_c)\,(\phi_{c'}|v_{c'c}|\phi_c) \tag{4.17}$$

$$\equiv \int d\boldsymbol{\xi}_a d\boldsymbol{\xi}_A \tilde{V}_{c'c}(\boldsymbol{R}, \boldsymbol{\xi}_a, \boldsymbol{\xi}_A)\rho_{A'A}(\boldsymbol{\xi}_A)\rho_{a'a}(\boldsymbol{\xi}_a) \tag{4.18}$$

where $\tilde{V}_{c'c}$ is the effective interaction that induces the transition between the channels and ρ_{ij} is the transition density between the nucleus of $i \to j$. They are calculated from the single-particle wave function and the one-body transition densities as

$$\rho_{ij} = \sum \langle j||[a_n^\dagger a_p]||i\rangle\,[\phi_p^* \phi_n]. \tag{4.19}$$

The sum runs over all the possible particle-hole combinations in the model space whose quantum numbers are equal to that of the corresponding transition. In the present case,

the particle-hole pairs with $S = 1$ and $T = 1$ are taken for the projectile.

The transition form factor for each step is obtained using FOLD [89] by double-folding the effective interaction at 270 MeV by Franey-Love [90] with transition densities for the projectile and the target. The Franey-Love interaction is an effective NN interaction constructed to describe nucleon-nucleus scattering at 50–1000 MeV/nucleon incident energies. It has been successfully applied to reaction analyses of scatterings of nucleons and light nuclei off the target nucleus.

The transition densities for the projectile are calculated using the shell-model code NuShellX [91]. We fix the transition of the projectile as $^{12}\mathrm{C}_{\mathrm{gnd}}(0^+) \rightarrow {}^{12}\mathrm{B}_{\mathrm{gnd}}(1^+) \rightarrow {}^{12}\mathrm{Be}(0^+_2)$ with the transfer of the orbital angular momentum $\Delta L = 0$. Utsuno–Chiba Hamiltonian for *p-sd* shell [92] is used with modification of the increased *p-sd* shell gap by 1 MeV [54]. The transition densities are input as $Z_J(j_p, j_h)$ coefficients [93] in FOLD.

The validity of the transition densities is checked by comparing the Gamow–Teller transition strength B(GT) calculated using the transition densities with the experimental one. B(GT) is defined as

$$B(\mathrm{GT}) = \frac{1}{2J_i + 1} \left| \left\langle f \left\| \sum_k \sigma_k \tau_k \right\| i \right\rangle \right|^2 . \tag{4.20}$$

The corresponding B(GT) to the transition densities of $Z_J(j_p, j_h)$ is calculated using Eq. (13a) in Ref. [93]. The obtained transition densities correspond to the Gamow–Teller transition strengths B(GT) of 1.0 for $^{12}\mathrm{C}_{\mathrm{gnd}} \rightarrow {}^{12}\mathrm{B}_{\mathrm{gnd}}$ and 0.27 for $^{12}\mathrm{B}_{\mathrm{gnd}} \rightarrow {}^{12}\mathrm{Be}(0^+_2)$ with a widely accepted value of the quenching factor, 0.6. They reproduce the values deduced from the log ft values of the β decay [94] and the data of the charge exchange $^{12}\mathrm{B}_{\mathrm{gnd}}(^7\mathrm{Li},^7\mathrm{Be})^{12}\mathrm{Be}$ reaction [54].

For the target, transitions of specific one-particle-one-hole (p, h) configurations are calculated individually. The calculations for $\Delta L_{\mathrm{DCX}} = 0$, the (p,h) configurations of $(f_{7/2}, f^{-1}_{7/2})$ and $(f_{5/2}, f^{-1}_{7/2})$ are taken for both the transition of $^{48}\mathrm{Ca} \rightarrow {}^{48}\mathrm{Sc}$ and $^{48}\mathrm{Sc} \rightarrow {}^{48}\mathrm{Ti}$. The transition density was set to an arbitrary value ($Z = 1$), which corresponds to B(DGT) of 10.3 for $(f_{7/2}, f^{-1}_{7/2})$ and 13.7 for $(f_{5/2}, f^{-1}_{7/2})$.

The single-particle radial wave functions for the projectile and the target were calculated with Wood–Saxon potentials [95] with the parameters of radius $r_0 = 1.25$ fm, diffuseness $a = 0.65$ fm, and spin-orbit potential strength $V_{\mathrm{so}} = 7.0$ MeV, respectively, in which the potential depths of the volume term were tuned to reproduce the binding energies for neutrons and protons. The binding energies were taken as the neutron or proton separation energies.

The obtained form factors are shown in Fig. 4.3. The left panel of the figure shows the form factors for the first step: $^{48}\mathrm{Ca} + {}^{12}\mathrm{C} \rightarrow {}^{48}\mathrm{Sc} + {}^{12}\mathrm{B}$. The right panel of the figure shows the form factors for the first step: $^{48}\mathrm{Ca} + {}^{12}\mathrm{C} \rightarrow {}^{48}\mathrm{Sc} + {}^{12}\mathrm{B}$. The two patterns of (p,h) configurations in the target are overlaid. The red and magenta curves show the real

part of the form factor with (p,h)=($f_{7/2}$, $f_{7/2}^{-1}$) and ($f_{5/2}$, $f_{7/2}^{-1}$), respectively. The blue and grape curves show the imaginary part of the form factor with (p,h)=($f_{7/2}$, $f_{7/2}^{-1}$) and ($f_{5/2}$, $f_{7/2}^{-1}$), respectively.

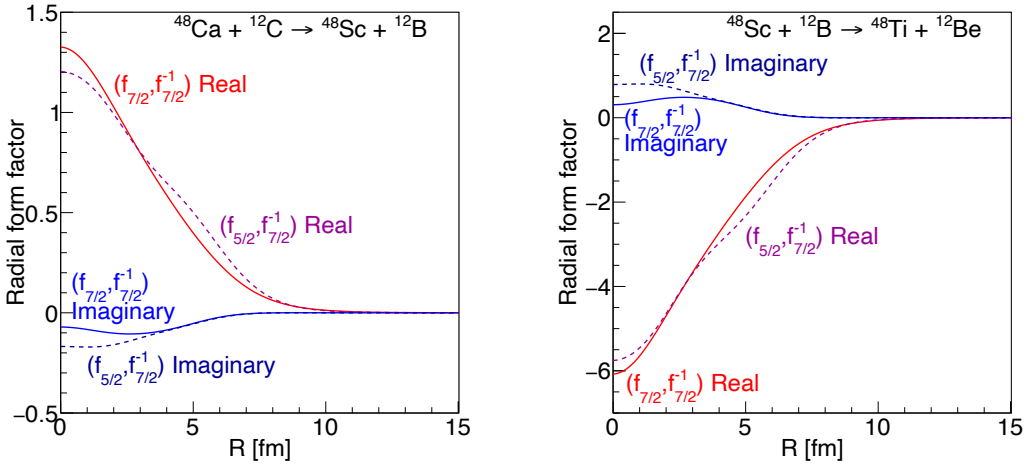

Figure 4.3: Transition form factors calculated by FOLD. Left: ^{48}Ca + ^{12}C → ^{48}Sc + ^{12}B, right: ^{48}Sc + ^{12}B → ^{48}Ti + ^{12}Be. Red and blue solid lines show the real and imaginary part of the potentials for the configuration of (p,h)=($f_{7/2}$, $f_{7/2}^{-1}$), respectively. Violet and navy broken lines show the real and imaginary part of the potentials for the configuration of (p,h)=($f_{7/2}$, $f_{5/2}^{-1}$), respectively.

4.3 Optical potential

The optical potentials for the entrance, intermediate, and exit channels were obtained through the global optical potential based on the double-folding-model [7]. The global optical potential is constructed for the description of nucleus-nucleus scatterings and is obtained by folding the CEG07 G-matrix interaction [96, 97] with projectile and target density distributions. It is applicable to reactions nucleus-nucleus systems including unstable nuclei, as in the present case, at 50–400 MeV/nucleon. In Ref. [7], the validity of the optical potential is verified for several cases including ^{40}Ca +^{16} O, ^{90}Zr +^{16} O at E=93.9 MeV/nucleon and ^{12}C + ^{12}C at 25–200 MeV/nucleon. Figure 4.4 shows the real and imaginary parts of the potential.

4.4 Calculated angular distribution

We calculated the three patterns of the cross sections for the DCX reaction. The first type is $\Delta L = 0$ in both of the transitions from the initial state to the intermediate state and from the intermediate state to the final state. This corresponds to the DGT transition. We refer

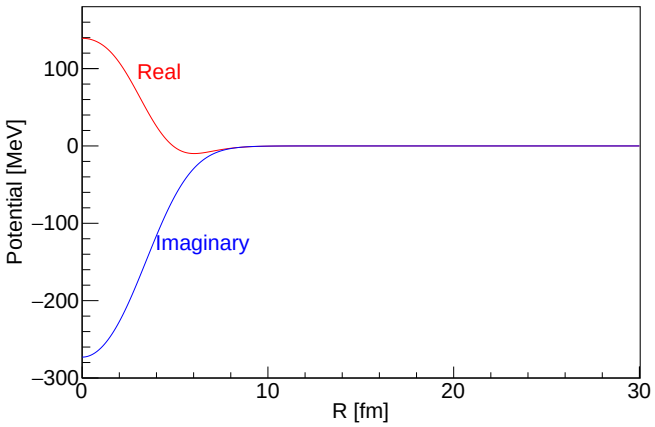

Figure 4.4: Optical potential for ^{48}Ca + ^{12}C at 250 MeV/nucleon obtained through the global optical potential in Ref. [7].

to this combination of the transfers of ΔL as "$\Delta L_{\mathrm{DCX}} = 0$" in the following. Other two types are $\Delta L = 1$ or $\Delta L = 2$ for the transition from the initial to the intermediate state, and $\Delta L = 0$ for from the intermediate state to the final state. We refer to these as "$\Delta L_{\mathrm{DCX}} = 1$" and "$\Delta L_{\mathrm{DCX}} = 2$", respectively. For calculating $\Delta L_{\mathrm{DCX}} = 1$ and 2, $(g_{5/2}, f_{7/2}^{-1})$ and $(f_{7/2}, f_{7/2}^{-1})$ are assumed, respectively.

The cross sections of $\Delta L_{\mathrm{DCX}} = 0$, 1, and 2 were calculated with ECIS97. The potentials obtained above were used. The momentum transfer in each transition is designated. The Q-value going to the intermediate state, which is defined as the energy difference compared to the initial state, was set to a half of that of the final state.

The solid lines in Fig. 4.5 shows the angular distributions of $\Delta L_{\mathrm{DCX}} = 0$ (red), $\Delta L_{\mathrm{DCX}} = 1$ (blue), and $\Delta L_{\mathrm{DCX}} = 2$ (black), respectively. Here, the cross sections scaled to arbitrary values are shown. The left panel shows the calculation at the Q-value of the final state of $-Q = 24$ MeV (corresponds to the excitation energy in ^{48}Ti of $E_{\mathrm{ex}} = 1$ MeV), while the right panel shows at $-Q = 54$ MeV ($E_{\mathrm{ex}} = 31$ MeV). The $\Delta L_{\mathrm{DCX}} = 0$ has a peak at 0° while other transitions of $\Delta L_{\mathrm{DCX}} = 1$ and $\Delta L_{\mathrm{DCX}} = 2$ have at $\sim 0.5°$ and $\sim 0.7°$, respectively.

The thin lines show the distributions smeared with the experimental angular resolution of $\Delta\theta_{\mathrm{CM,horizontal}} = 0.197°$ and $\Delta\theta_{\mathrm{CM,vertical}} = 0.217°$. These smeared distributions were used for the fit described in the next chapter (Chapter 5).

The shape of the angular distribution depends on Q-value in $\Delta L_{\mathrm{DCX}} = 1$ and $\Delta L_{\mathrm{DCX}} = 2$. The change in $\Delta L_{\mathrm{DCX}} = 0$ is negligible.

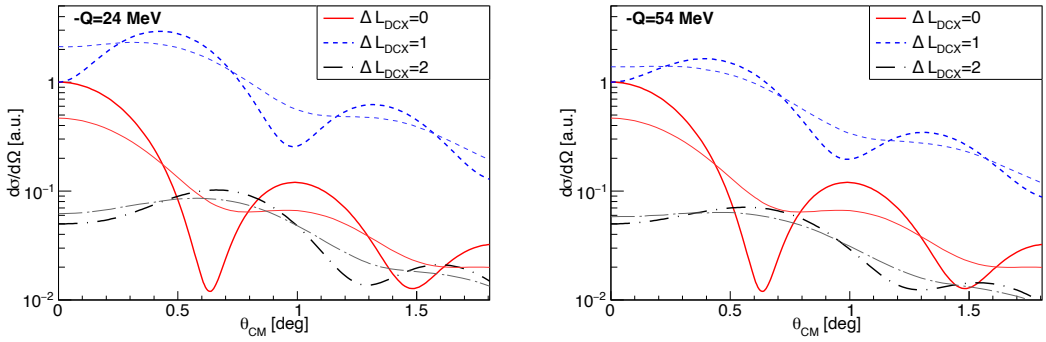

Figure 4.5: Calculated angular distributions for $\Delta L_{\rm DCX}$ =0, 1, and 2. Calculation at $-Q$ =24 MeV (left) and 54 MeV (right). The thick (thin) curves represent the distribution before (after) the angular smearing.

4.5 Unit cross section and (q, ω) dependence

The absolute value of the cross section for the $\Delta L_{\rm DCX} = 0$ transition is related to the DGT transition strength B(DGT) which is defined as

$$B(\mathrm{DGT}) = \frac{1}{2J_i + 1} \left| \langle f \| (\sigma\tau)^2 \| i \rangle \right|^2 . \tag{4.21}$$

It is well known that the proportionality relation holds for GT transitions [24] between the cross section and the transition strength B(GT). In the following it is assumed that the proportionality relation analogous to that also holds for the DGT transitions as

$$\frac{d\sigma}{d\Omega}(0^\circ) = \hat{\sigma}_{\rm DGT} F(q, \omega) B(\mathrm{DGT}), \tag{4.22}$$

where $\hat{\sigma}_{\rm DGT}$ is the normalization factor, so-called "unit cross section" of the DGT transition. $F(q, \omega)$ describes the dependences on the momentum q and energy ω transfers and is defined to be unity at $(q, \omega) = (0, 0)$. In heavy ion reactions where both the projectile and the target are composites of nucleons, B(DGT) can be reasonably factorized as

$$\frac{d\sigma}{d\Omega}(0^\circ) = \hat{\sigma}_{\rm DGT} F(q, \omega) B_{\rm target}(\mathrm{DGT}) B_{\rm projectile}(\mathrm{DGT}), \tag{4.23}$$

where $B_{\rm target}$ and $B_{\rm projectile}$ are the DGT strengths in the target and the projectile, respectively. It should be noted that the validity of the proportionality relation Eq. (4.22) is subject to future experimental and theoretical verifications, although it is a reasonable starting point in reaction studies of the DGT strength at high excitation energies. The goal of the present work is to deduce $B_{\rm target}$ from the experimental cross section. $\hat{\sigma}_{\rm DGT}$, $F(q, \omega)$, and $B_{\rm projectile}$(DGT) are deduced as follows.

The $B_{\rm projectile}$(DGT) is obtained by taking as the product of the B(GT) in $^{12}\mathrm{C}_{\rm gnd}(0^+) \rightarrow {}^{12}\mathrm{B}_{\rm gnd}(1^+)$= 0.979 ± 0.006 [94] and $^{12}\mathrm{B}_{\rm gnd}(1^+) \rightarrow {}^{12}\mathrm{Be}(0^+_2)$ = 0.214 ± 0.051 [54], leading to $B_{\rm projectile}$(DGT) = 0.21 ± 0.05.

The unit cross section $\hat{\sigma}_{\mathrm{DGT}}$ was deduced from the calculated cross section at 0° for four patterns of (p,h) combinations. The calculation is carried out for a transition density, $Z = 1$, in each case. The corresponding B(GT) values are summarized in Table 4.1. B_{target}(DGT) are calculated as products of B(GT) in each step, as shown in the last column in the Table 4.1. If possible it is better to show the calculated values of the cross section. The correlation of the calculated cross section at 0° and $Q = 0$ MeV, and corresponding B(DGT) are shown in Fig. 4.6. Deviation from the proportionality relation is expected to be due to differences in the absorption effects between $f_{7/2}$ and $f_{5/2}$ orbits. Except for the small deviations, the relation is approximately proportional and $\hat{\sigma}_{\mathrm{DGT}}$ is obtained as the linear coefficient.

Table 4.1: (p,h) configuration and B(DGT)

(p,h)$_{^{48}\mathrm{Ca}\to^{48}\mathrm{Sc}}$	(p,h)$_{^{48}\mathrm{Sc}\to^{48}\mathrm{Ti}}$	B(GT)$_{^{48}\mathrm{Ca}\to^{48}\mathrm{Sc}}$	B(GT)$_{^{48}\mathrm{Sc}\to^{48}\mathrm{Ti}}$	B_{target}(DGT)	Calculated cross section [μb/sr]
$(f_{7/2}, f_{7/2}^{-1})$	$(f_{7/2}, f_{7/2}^{-1})$	10.3	10.3	106	6.92
$(f_{7/2}, f_{7/2}^{-1})$	$(f_{5/2}, f_{7/2}^{-1})$	10.3	13.7	141	10.46
$(f_{5/2}, f_{7/2}^{-1})$	$(f_{7/2}, f_{7/2}^{-1})$	13.7	10.3	141	10.49
$(f_{5/2}, f_{7/2}^{-1})$	$(f_{5/2}, f_{7/2}^{-1})$	13.7	13.7	188	16.04

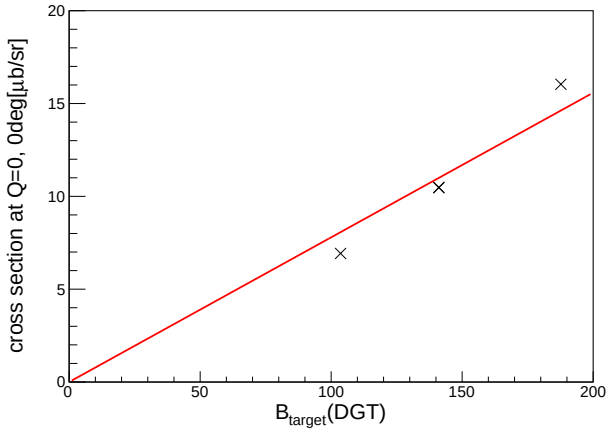

Figure 4.6: Calculated cross section against the B(DGT) assumed in the calculation.

The cross section of $\Delta L_{\mathrm{DCX}} = 0$ can depend on the Q-value through the change of q and ω with the Q-value. The q- and ω-dependence of $F(q,\omega)$ was evaluated with the calculated cross section as

$$F(q,\omega) = \frac{d\sigma(q,\omega)/d\Omega}{d\sigma(q=0,\omega=0)/d\Omega}. \tag{4.24}$$

Figure 4.7 shows the ratio of the cross section at 0° to the one at $Q = 0$ for each (p,h) configuration. Here $E_{\mathrm{ex}} = 0$ corresponds to $-Q = 23.1$ MeV. There is no strong dependence of the (p,h) combinations and the averaged value over four configurations is used for the analysis.

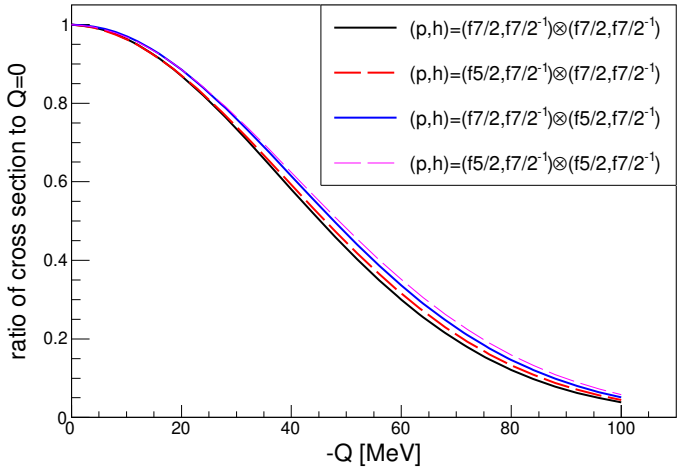

Figure 4.7: Excitation energy dependence of the DGT cross section for DCX.

4.6 Comparison with data of single charge exchange

The calculation was validated by comparing the calculated angular distribution for the single charge exchange (SCX) reaction of ^{48}Ca(^{12}C, ^{12}B)^{48}Sc(1^+, 2.5 MeV) with the experimental data. The experimental angular distribution is shown as the points in Fig. 4.8 by integrating the measured cross section over $1.6 < E_{\mathrm{ex}} < 3.6$ MeV (See the inset of Fig. 4.8). The experimental angular distribution was compared with a superposition of the calculated cross sections of the $\Delta L = 0$ and $\Delta L = 2$ transition. In the calculations, the (p,h) configurations of $(f_{7/2}, f_{7/2}^{-1})$ are taken for the target transitions and the calculated angular distributions are smeared by the experimental angular resolution. The data are described mainly by the $\Delta L = 0$ distribution with an additional $\Delta L = 2$ component up to $\theta_{\mathrm{cm}} \sim 1^\circ$. The normalization for the $\Delta L = 0$ component corresponds to a B(GT) value of 1.4, which is close to the transition strength of 1.09 ± 0.01, observed in an independent (^{3}He, t) measurement [98].

4.7 Uncertainty in calculation

The systematic errors in the calculation are checked by performing the calculation with changing parameters. The effective interaction at 250 MeV instead of 270 MeV. The change in the shape of the angular distribution is negligible in the decomposition analysis as described in the next chapter. The absolute value of the calculated cross section at 0° increases 27%.Another possible uncertainty comes from the strength of the projectile, $B_{\mathrm{projectile}}$(DGT) $= 0.21 \pm 0.05$, which means the uncertainty of 24% relatively.

In the present situation, the only available experimental reference is the single charge exchange reaction measured in this work. The reproducibility of the angular pattern seems

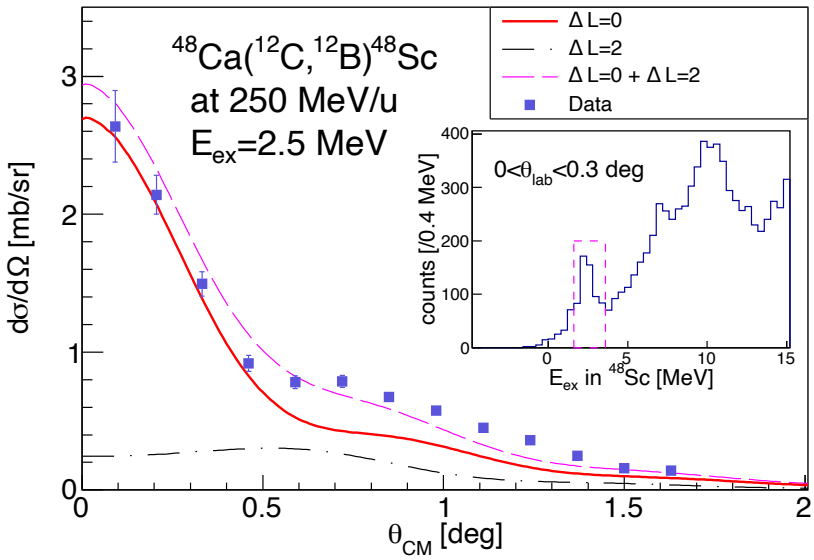

Figure 4.8: Angular distribution for the SCX reaction of ^{48}Ca(^{12}C, ^{12}B)^{48}Sc around E_{ex} = 2.5 MeV. Red and black curves are calculated angular distributions using ECIS for $\Delta L = 0$ and $\Delta L = 2$, respectively. Magenta curve is the sum of $\Delta L = 0$ and $\Delta L = 2$. The inset shows the observed counts at $\theta_{lab} = 0°$–$0.3°$ against the excitation energy in ^{48}Sc.

to be within 10% while the reproducibility of the strength of SCX is 30%. In addition, another uncertainty is expected to arise in the two-step calculation. Further studies on the double charge exchange reaction from both experimental and theoretical sides are needed.

Chapter 5

Discussion

The DGT components are extracted by decomposing the experimental angular distributions into those with different ΔL_{DCX} using the calculated angular distributions (multipole decomposition analysis, MDA). As different ΔL_{DCX} components have characteristic angular distributions, as shown in Chapter 4, the observed cross sections can be decomposed by fitting with the sum of each component. Especially, the feature that $\Delta L_{\mathrm{DCX}} = 0$ component has a peak at 0° makes possible to extract it more robustly than other components.

The Gamow–Teller transition strength B(DGT) is also evaluated with the extracted cross section. The excitation energy distribution of B(DGT) are compared to the expectation by the harmonic picture or the shell model calculation. The future perspectives are given based on the discussion.

5.1 Multipole Decomposition Analysis (MDA)

The experimentally obtained angular distributions at each excitation energy bin $\sigma^{\mathrm{exp}}(\theta_{\mathrm{cm}}, E_{\mathrm{ex}})$ were fitted, by means of the maximum likelihood method, by the sum of the calculated angular distributions $\sigma^{\mathrm{calc}}_{\Delta L_{\mathrm{DCX}}}$ weighted with fitting coefficients $a_{\Delta L_{\mathrm{DCX}}}$ as

$$\sigma^{\mathrm{exp}}(\theta_{\mathrm{cm}}, E_{\mathrm{ex}}) = \sum_{\Delta L_{\mathrm{DCX}}=0,\ 1,\ 2} \left\{ a_{\Delta L_{\mathrm{DCX}}} \cdot \sigma^{\mathrm{calc}}_{\Delta L_{\mathrm{DCX}}}(\theta_{\mathrm{cm}}, E_{\mathrm{ex}}) \right\} + \sigma_{\mathrm{BG}}(\theta_{\mathrm{cm}}, E_{\mathrm{ex}}). \tag{5.1}$$

Here the accidental coincidence backgrounds with room-background γ-rays are take into account explicitly, and their cross sections are expressed as $\sigma_{\mathrm{BG}}(\theta_{\mathrm{cm}}, E_{\mathrm{ex}})$ which are evaluated in Sec. 3.6.2.

The parameters were determined so as to maximize the log likelihood. The Poisson distribution is assumed. The likelihood is calculated as

$$L = \prod_{\theta_i=0}^{\theta_{i\mathrm{max}}} P(a_0 n_{0,\theta_i} + a_1 n_{1,\theta_i} + a_2 n_{2,\theta_i} + \lambda_{\mathrm{BG},\theta_i};\ X_{\theta_i}), \tag{5.2}$$

where $P(n;X)$ is the Poisson distribution, $P(n;X) = n^X e^{-n}/X!$. $n_{\Delta L,i}$ is the expected counts from the calculation at the energy and the ith angle. $\lambda_{\mathrm{BG},i}$ is the expected counts of the background. We used the cross section data at five angles in the most forward region: $i_{\max} = 4$, $\theta_0 = [0.0^\circ, 0.3^\circ]$, $\theta_1 = [0.3^\circ, 0.5^\circ]$, $\theta_2 = [0.5^\circ, 0.7^\circ]$, $\theta_3 = [0.7^\circ, 0.9^\circ]$, and $\theta_4 = [0.9^\circ, 1.1^\circ]$. The coefficients of a_0, a_1, and a_2 are determined by minimizing the $-\ln L$.

5.2 Decomposed results

The experimental angular distributions are fitted for every 4-MeV bin of the excitation energy in ^{48}Ti. Figure 5.1 gives the decomposed angular distributions. The histograms with navy lines represent experimental cross sections in which the accidental backgrounds are not subtracted. The hatched histograms with cyan color are the cross sections of the accidental backgrounds. The error bars show only the statistical uncertainty. The dots show the results of the MDA; Red squares, blue triangles, and black inverted triangles are $\Delta L_{\mathrm{DCX}} = 0,\ 1$, and 2 components, respectively. The magenta circles show the sum of the strengths of $\Delta L_{\mathrm{DCX}} = 0,\ 1,\ 2$, and the cross sections of backgrounds, which are directly comparable to the experimental cross sections (histograms with navy lines). Though only the five points ($\theta_{\mathrm{CM}} < 1.1^\circ$) are used for the fitting, the overall trend of the angular dependence of the cross sections up to 1.8° is described well by the results of the MD analysis. At the energy bins of $18 < E_{\mathrm{ex}} < 22$ MeV, $26 < E_{\mathrm{ex}} < 30$ MeV, and $34 < E_{\mathrm{ex}} < 38$ MeV, where prominent structures are found at the most forward angle in Fig. 3.31, 30–60% of the cross sections at the most forward angle are attributed to $\Delta L_{\mathrm{DCX}} = 0$ components.

The excitation energy distribution of the decomposed spectra is shown in Fig. 5.2. The dots show the observed cross sections while the results of the MD analysis are shown as stacking histograms of the background (cyan), $\Delta L_{\mathrm{DCX}} = 0$ (red), $\Delta L_{\mathrm{DCX}} = 1$ (blue), and $\Delta L_{\mathrm{DCX}} = 2$ (black).

5.2.1 Evaluation of the error

The evaluation of the $\Delta L_{\mathrm{DCX}} = 0$ components has a large uncertainty in the division of the cross sections to each ΔL_{DCX} component. The strengths cannot be independently determined and have a correlation with each other. The statistical errors were evaluated by drawing an envelope of $-\ln L_{\min}$ + constant in the parameter space with the constant = 1.765 corresponding to the one standard deviation in the three-parameter fitting [99, 100] (see detail for Appendix C.1).

The systematic uncertainty of the extracted cross sections arises from the experimental systematical error, the analysis of the decomposition, and the uncertainty of the calculated angular distribution. The experimental error is 36% as described in Sec. 3.6.1. The uncertainty of the analysis was checked by performing the fitting with four points instead of

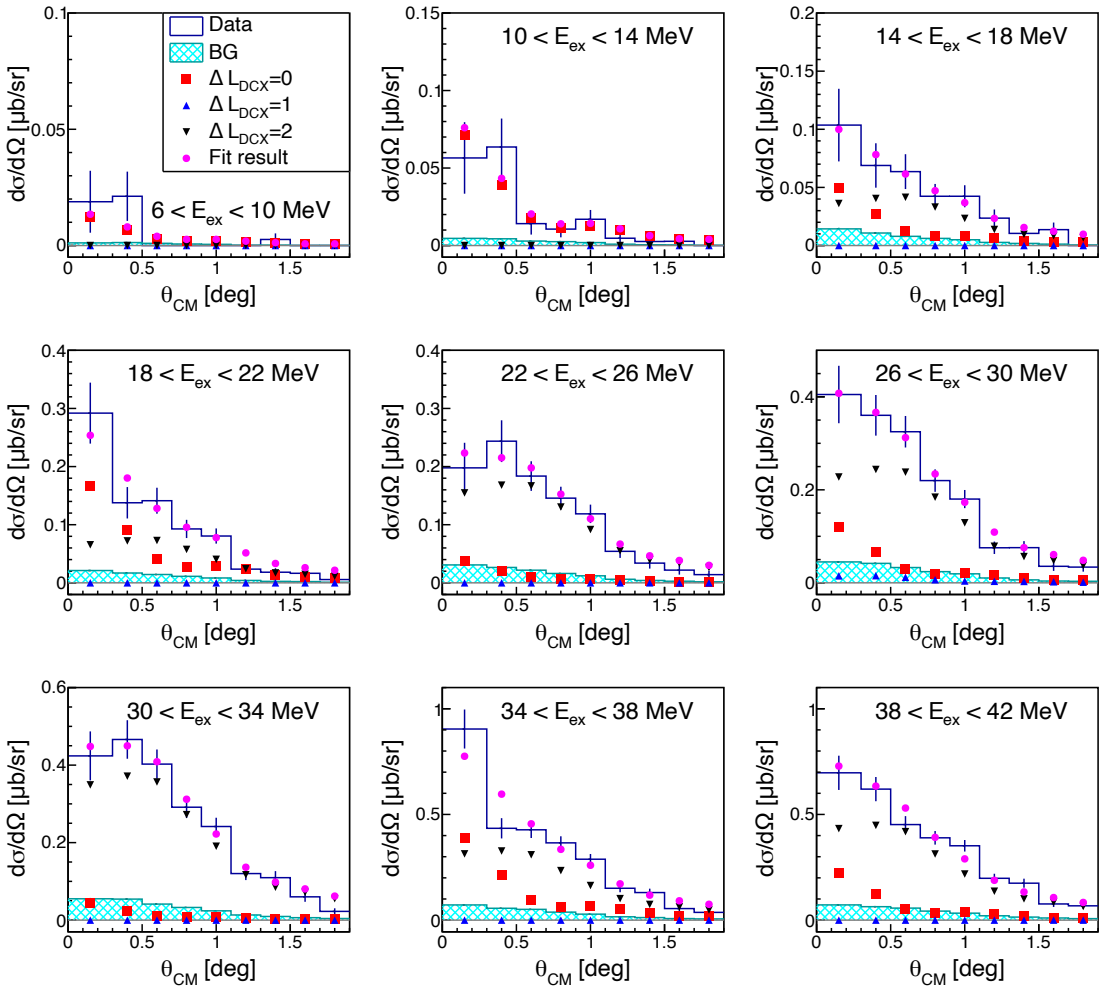

Figure 5.1: The histograms with blue outline shows the experimental angular distribution at each energy bin. The hatched histograms show the accidental coincidence background. The decomposed results are shown in dots (See text for detail).

five points, or by changing the angular binning. The trend of the energy distribution of the fitted results is not changed and the variation for the strength of the points at 18–22 MeV is within 10%. The uncertainty of the expected angular distribution obtained from the calculation is checked by changing the effective interaction. The difference in the angular distribution contributes 1% to the results of the fitting.

5.2.2 Cross section integrated over E_{ex} =0–34 MeV

The extracted $\Delta L_{\mathrm{DCX}} = 0$ cross sections at 0° are integrated over 0 to 34 MeV. The integration is calculated as

$$\sum_{E_{\mathrm{ex}}=8\ \mathrm{MeV}}^{E_{\mathrm{ex}}=32\ \mathrm{MeV}} \frac{d\sigma}{d\Omega}_{L_{\mathrm{DCX}}=0}(E_{\mathrm{ex}}), \tag{5.3}$$

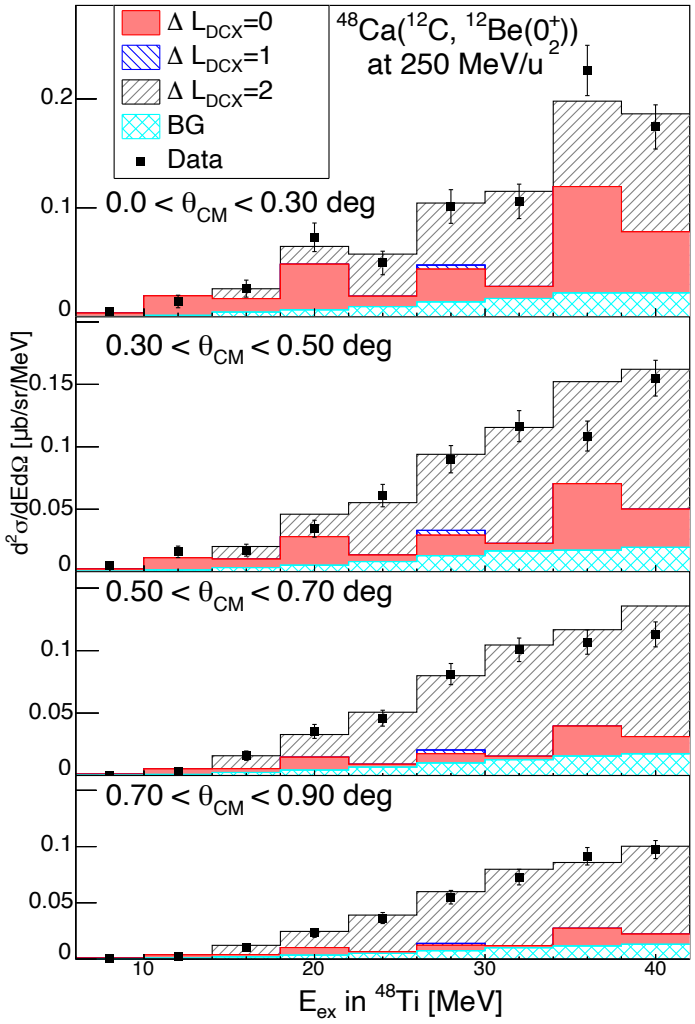

Figure 5.2: The decomposed cross section spectra of the ^{48}Ca(^{12}C, ^{12}Be(0^+_2))^{48}Ti reaction at forward angles.

which is the sum of the points in Fig. 5.3. The obtained value with error is $0.50^{+0.35}_{-0.11}$ μb/sr. The error is evaluated using the Monte Carlo method. The cross sections are generated with Gaussian distributions by each energy bin. The integrated cross section was calculated with eq. 5.3 by each generated event. The upper and lower limit of the range of the error were determined so that the number of events within the error to be determined is 68.3% of the total events. The detail is described in Appendix C.2.

5.3 DGT transition strength

The DGT transition strength B(DGT) was obtained from the cross section of the extracted $\Delta L_{\mathrm{DCX}} = 0$ components. It is assumed that the all of the extracted $\Delta L_{\mathrm{DCX}} = 0$ components

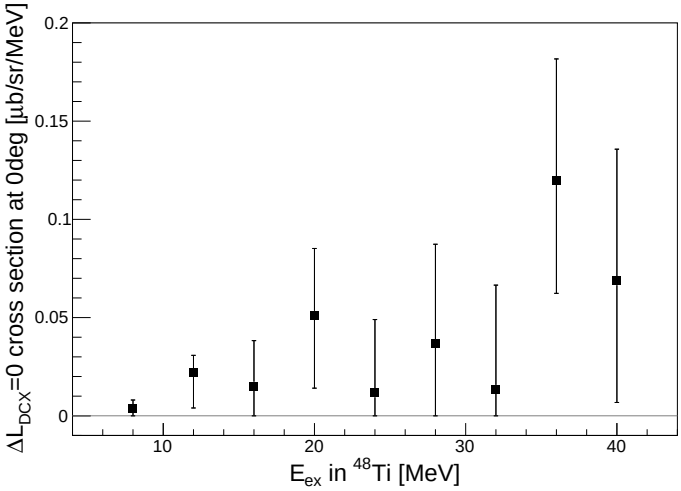

Figure 5.3: The extractted cross section spectra of the ^{48}Ca(^{12}C, ^{12}Be(0^+_2))^{48}Ti reaction at the most forward angles of $0 < \theta_{CM} < 0.3°$.

are attributed to the DGT transition. The validity of the assumption is discussed in the next section. The experimental B_{target}(DGT) was derived by applying the extracted $\Delta L_{\text{DCX}} = 0$ cross sections to Eq. (4.23) described in Sec. 4.5. Figure 5.4 shows the B(DGT) distribution. The errors denoted here are those from the determination of the $\Delta L_{\text{DCX}} = 0$ cross section at each energy.

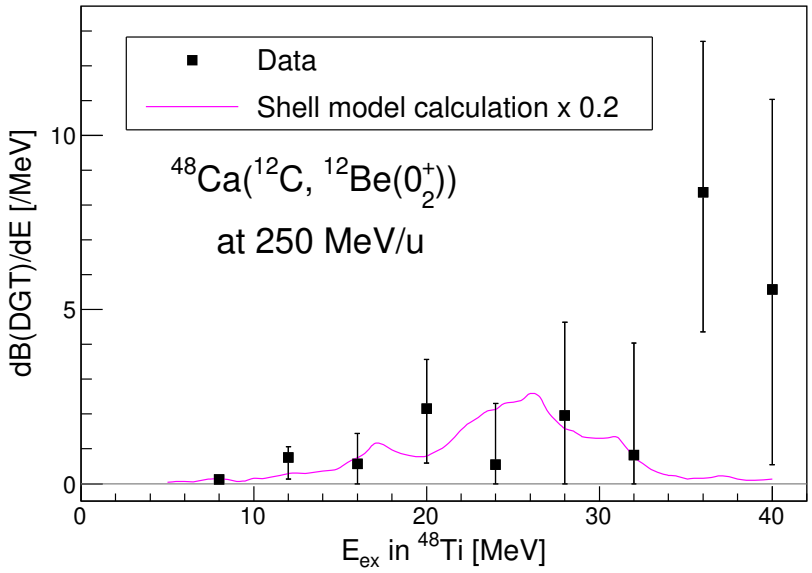

Figure 5.4: The double Gamow–Teller transition strength B(DGT) obtained by MD analysis of the ^{48}Ca(^{12}C, ^{12}Be(0^+_2)) spectra. The prediction by the shell model calculation [8] with the effective interaction of GXPF1B is shown by the magenta curve, which is scaled by 0.2.

5.4 Comparison with expectation for the structure below 34 MeV

The deduced distribution of B(DGT) is discussed. The shell model calculation using GXPF1B interaction [8] for the $J^\pi = 0^+$ final state is presented by the magenta curve in Fig. 5.4.

In the extraction of $\Delta L_{\rm DCX} = 0$ components, other transitions with similar angular distributions to DGT are not excluded. Here it should be reminded that the (^{12}C, ^{12}Be(0^+_2)) reaction induces only isovector spin-flip transitions (See discussion in Sec. 1.6). Transitions that could be taken into consideration is an excitation of GT on top of an isovector spin monopole (IVSM) resonance or double spin dipole ($[\Delta L = 1] \otimes [\Delta L = 1]$) excitation. IVSM is a $2\hbar\omega$ excitation with the same spin parity as the GT transition. ($[\Delta L = 1] \otimes [\Delta L = 1]$) excitation could show the peak at most forward angle as a transition is possible with $\Delta L = 0$ from initial to final state in total. They are indistinguishable from each other by their angular distribution. However, these transitions can be excluded by considering their expected centroid energies. Assuming the simple superposition of their individual processes, we can estimate the energies where those double resonances lie. The centroid energy of the single GT resonance is ~ 12 MeV from the ground state of ^{48}Ca with the width of 5 MeV [60, 61], thus we expect that the DGTGR lies around $12 \times 2 \sim 24$ MeV, which corresponds to $E_{\rm ex} = 28$ MeV in ^{48}Ti, with the width of $5 \times \sqrt{2} \sim 7$ MeV. As the energy of IVSM is estimated to be 27 MeV [101] from the g.s. of ^{48}Ca, the position of IVSM $\otimes$ GT resonance is expected to be around 39 MeV. Double spin dipole would appear around 30 MeV according to the empirical formula in Ref. [102]. Thus the components below 34 MeV is mainly discussed as they are considered to be primarily attributed to DGT transitions. On the other hand, the enhancement at 34–42 MeV has a possibility to be attributed to other transitions. This is discussed later (in Sec. 5.5).

For the quantitative discussion, the observed total strength S, the centroid energy E_c, and the width Γ was calculated from the deduced distribution. The sum of the measured B(DGT) below 34 MeV is

$$S = \sum_i B_i(\mathrm{DGT}), \tag{5.4}$$

where i denotes the energy bin of the ^{48}Ti.

The centroid energy is

$$E_c = \frac{\sum_i E_i B_i(\mathrm{DGT})}{\sum_i B_i(\mathrm{DGT})}, \tag{5.5}$$

and the standard deviation is

$$\Gamma = \frac{\sum_i (E_i - E_c) B_i(\mathrm{DGT})}{\sum_i B_i(\mathrm{DGT})}. \tag{5.6}$$

We calculated these values over $0 < E_{\rm ex} < 34$ MeV. The errors were evaluated in the same way as in the evaluation of the integrated $\Delta L_{\rm DCX} = 0$ cross section. The obtained values are $S = 28^{+22}_{-7}$, $E_c = 23 \pm 3$ MeV, and $\Gamma = 6 \pm 1$ MeV.

5.4.1 Centroid energy and width

First of all, the observed centroid energy and the width are compared to the expectation from the harmonic picture. The single GT energy of ^{48}Ca $\rightarrow$ ^{48}Sc is 12 MeV and the width is $\sim$ 5 MeV. Considering the simple superposition of each transition, the centroid energy of the DGT becomes $12 \times 2 \sim 24$ MeV from the ground state of ^{48}Ca, which corresponds to $\sim$ 28 MeV in the excitation energy in ^{48}Ti. On the other hand, the width is $\sqrt{2}$ larger than that of the single GT in the same picture, thus is expected to be $5 \times \sqrt{2} \sim 7$ MeV. The measured centroid energy of B(DGT) distribution below 34 MeV, $E_c = 23 \pm 3$ MeV seems to be smaller than that of the simple picture. It might be that there is some anharmonicity. While, the width, $\Gamma = 6 \pm 1$ MeV, is consistent to the harmonic picture.

The centroid energy and the width can also be compared with the shell model predictions. The deduced energy is also slightly smaller than the shell model calculation of 24 MeV, while the trend of the data points of B(DGT) and the predicted curve appears to be similar. The experimental data show two peaks at 20 MeV and 28 MeV as is seen in Fig. 5.4, (or more clearly seen in Fig. 3.31), which may correspond to peaks in the shell model prediction at 17 MeV and 26 MeV. Although the statistical uncertainty does not allow us to draw a clear conclusion, it is indicated that the experimental energy distribution is pushed out by 2–3 MeV, to the higher direction rather than the lower direction. Figure 5.5 shows other two expectations in Ref. [8] with different effective interactions. The similar trends appear but the relative height is different, so correspondence is unclear. As the number of the data points are limited due to the statistics, the fit would not work as a quantitative discussion.

In Ref. [8], the correlation of the centroid energy and the isovector paring interaction is pointed out. The centroid energy shifts approximately 5 MeV accordance with changing the isovector paring strength G^{01} from +0.5 MeV to −0.5 MeV. The direct comparison with the predicted curve to the present results is difficult because of the statistical errors. More high-statistics measurement will make it possible to directly compare of the observed distribution to the calculation by the shell model.

5.4.2 Total strength

The shell model calculation in Ref. [8] predicts the integrated transition strength for $J^\pi_f = 0^+$ is 127.4, while the approximated sum rule gives $2(N - Z)(N - Z + 1) = 144$ [103, 104]. The integrated B(DGT) below 34 MeV obtained in this work is 22^{17}_{-6}% of the total value of the shell model calculation (127.4). This factor of $\sim$ 0.2 is comparable to the

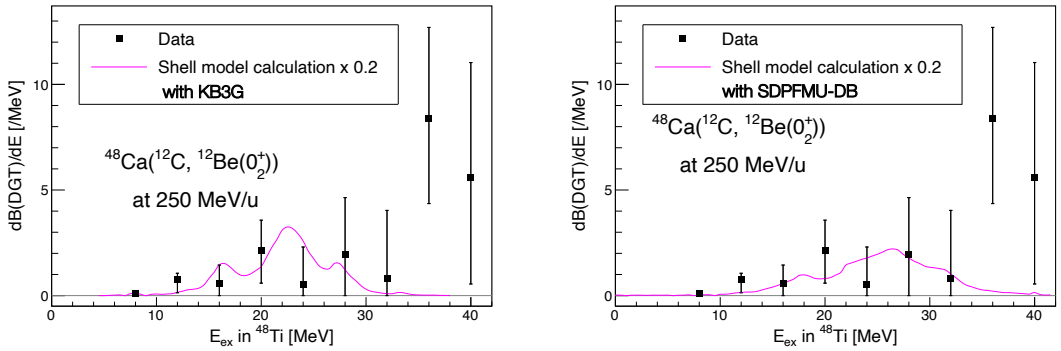

Figure 5.5: Same as Fig. 5.4 but the prediction by the shell model with different effective interactions [8]. Left: KB3G interaction, Right: SDPFMU-DB interaction.

typical quenching factor of ~ 0.6 known for the single GTGRs. In the single GTGRs, the quenching is understood as excitations to p-h configurations beyond the model space or excitations of non-nucleonic degrees of freedom [27, 26]. If the same quenching occurs in each of the two steps, the quenching factor in DGTGR might be $0.6 \times 0.6 = 0.36$. Thus the present value does not contradict this provisional counting. Still, further studies are required for qualitative discussion on the possible quenching since the current value suffers from uncertainties in both measurement and analysis.

5.4.3 Constraint on the NME of $0\nu\beta\beta$

Shimizu *et al.* pointed out that the nuclear matrix element (NME) of $0\nu\beta\beta$ can be calibrated by the observables of the DGTGR [8]. Figure 5.6 shows the correlation between the centroid energy of the DGTGR in ^{48}Ca and $0\nu\beta\beta$ NME. If we apply the present results for this correlation, NME would be $\sim 0 \pm 2$.

The current experimental constraint to the $0\nu\beta\beta$ is $T^{0\nu}_{1/2} = 2.3 \times 10^{26}$ year at 90% confidence level obtained in KamLAND-Zen experiment [10]. The present status of the experimental upper limits are shown in the Fig. 5.7 with the correlation of the effective Majorana neutrino mass $\left\langle m_{\beta\beta} \right\rangle$ and the lightest neutrino mass [10]. The relation between the neutrino mass and the half life of $0\nu\beta\beta$ $[T^{0\nu}_{1/2}]^{-1}$, and NME $M_{0\nu}$, is $[T^{0\nu}_{1/2}]^{-1} = G_{0\nu}|M_{0\nu}|^2 \left\langle m_{\beta\beta} \right\rangle^2$, where the $G_{0\nu}$ is the phase space factor [105]. The determination precision of $\left\langle m_{\beta\beta} \right\rangle$ is proportional to that of the inverse of NME. If the demand for the precision of the determination of the NME is relative 50% to the value, it corresponds to the determination of the centroid energy with 0.7-MeV precision. The present results is not sufficient and further study is needed. In order to determine the centroid energy by the resolution of 0.7 MeV, the statistics should be 50 times. The future prospects will be discussed in Sec. 5.6.

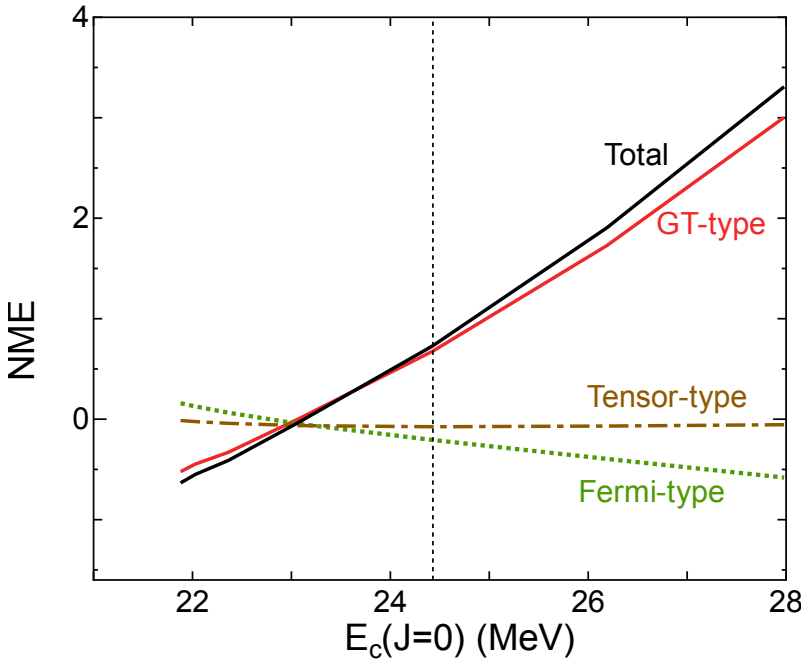

Figure 5.6: Correlation between NME and centroid energy of DGTGR for $J_f = 0^+$ [9].

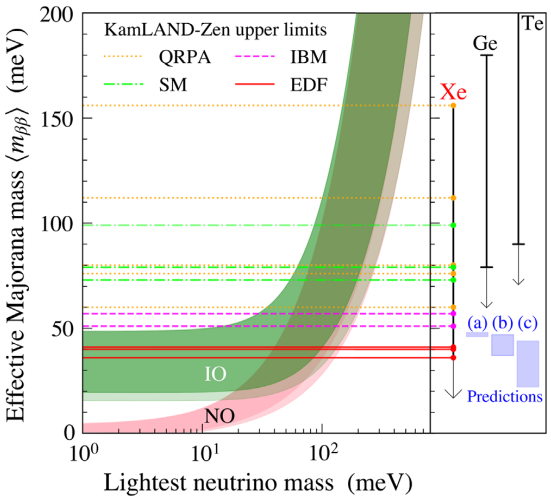

Figure 5.7: Current status of measurement of double β decay and neutrino mass [10].

5.5 Structure above 34 MeV

The structure above 34 MeV, especially the distinct strength with a width of $\sim$ 5 MeV in the region of $34 < E_{\rm ex} < 38$ MeV, is not accounted for by the shell model calculation. The contribution from the ^{12}C(^{12}C, ^{12}Be(0^+_2))^{12}O$_{\rm g.s.}$ reaction accounts for approximately 6$\pm$2% of the observed strength. The possible interpretations of this structure are that the DGT strength distribution is pushed to higher energy, or that it should be attributed to transitions other than DGT. The expectation of the energy of IVSM $\otimes$ GT, 39 MeV, is close to the

observed enhancement. The double spin dipole excitation could also be taken into consideration with the expectation on 30 MeV. Nevertheless the above mentioned resonances have rather broad energy distributions in the SCX spectra [102, 101, 29]. Considering the observed width, the peak might not be attributed to these excitations without some novel mechanism. Further studies are needed to establish and interpret the enhancement at 36 MeV.

5.6 Future perspective

The present work provides the first experimental information on the DGT transition at high excitation energies which is important for understanding of previously unknown features of two-phonon excitations in spin-isospin channels. The quantitative evaluation of the DGT strength was performed for the first time by comparing the experimental angular distributions with the calculated ones. These studies made a path for the research of DGT transition at high excitation energy.

In the present work, the large uncertainty of the results does not allow to getting the clear picture of the DGTGR. Further studies from both of the experimental and theoretical side will contribute to a better understanding of the nature of DGTGR and the anharmonicity in the spin-isospin channel, and to further constrain the theoretical calculations of the nuclear matrix elements of $0\nu\beta\beta$. The future prospects are discussed in the following section.

The present results also provide the opportunity to discuss not only the DGT mode but also other multi-phonon modes such as the double spin dipole or GT⊗IVSM. Future studies on these other modes will lead to an inclusive understanding of the collectivity in the spin-dependent space.

5.6.1 Experimental prospect

The limited statistics in this work cause the large uncertainty in the quantitative evaluation of the observed structure. In the present work, data is accumulated for 1.5 days, and obviously a longer beamtime will result in data with higher statistics. In addition, considering that the contribution of the target thickness to the energy resolution is not dominant, the target thickness can be increased by three times.

One solution is the optimization of the setup. One of the main loss of the statistics is the survival ratio of the isomeric state of ^{12}Be(0^+_2) with a lifetime of 330 ns. The flight length from F0 to F8 is 89.5 m which corresponds to a time of flight of 488 ns. The alternative possibility is to analyze the momentum of the ^{12}Be in F0–F3 and detect γ-rays at F5. The flight length will be shortened to 55 m (TOF$\sim$ 300 ns), and the survival ratio will be twice.

Another solution is the choice of the target. The B(DGT) strength is roughly speaking in proportion to $(N-Z)^2$ of the target nucleus considering the sum rule ([104]. On the other hand, the unit cross section $\hat{\sigma}_{\mathrm{DGT}}$ is expected to decrease as in the case of the single GT investigated by (p,n) reaction [24]. A larger strength is expected for ^{208}Pb, for example. Assuming the unit cross section is 1/10 of that of ^{48}Ca, the expected yield is almost same as in ^{48}Ca target in the condition of the energy loss in the target to be retained. Considering the availability of the target, ^{208}Pb is more favorable than ^{48}Ca. ^{208}Pb also has the doubly closed shell nucleus which would enable the detailed nuclear structure studies.

In the sense of providing information to $0\nu\beta\beta$ NME, ^{136}Xe is one of the flagship nucleus. The neutron number is 82, so the strength will be 12 times of ^{48}Ca, and assuming the $\hat{\sigma}_{\mathrm{DGT}}$ is 1/3 with extrapolating the mass-number dependence in the single GTR [24], cross section will be four times of ^{48}Ca. The project of the installation of the gas target to F0 is now ongoing in cooperation with the group of pionic atoms spectroscopy in which they are planning to use deuteron gas for $(d,{}^3\mathrm{He})$ reaction with inverse kinematic measurement [106]. The target thickness of 90 mg/cm^2 is expected to be realized and the yield will be 12 times.

Given that the beamtime is twice, the efficiency of the data taking is twice, and the gain by changing the target is 10 times, the yield would be 40 times than the present result. With this improved statistics, one will be able to determine the centroid energy with the precision of 0.8 MeV and the width with 0.3 MeV when applying the present result. The sum of B(DGT) will be determined with the relative precision of 10% for the sum value (means $S = 27 \pm 3$, for example).

The study on the structure above 34 MeV is also interesting. The present data has the uncertainty of the evaluation of the contamination from ^{12}C. How they are observed in other targets also helps to understand the physics origin.

5.6.2 Theoretical prospect

The studies of the reaction mechanism of heavy ion double charge exchange are not sufficient at present. The uncertainty is large in the correspondence of the absolute value of the B(DGT) and the cross section. The validity of the optical potential is not well examined. The systematic studies of elastic scatterings of heavy ion reactions would help to validate the optical potentials or tuning them. There is another possibility to utilize DIAS for the calibration of the unit cross section in order to relate the cross section to B(DGT) [104]. DIAS is well studied. As the GT transition changes the nuclear isospin by $\Delta T = 1$, single GT-transitions from ^{48}Ca ($T = 4$) lead to states with $T = 3,\ 4,\ 5$. Similarly, the DGT transitions lead to $T = 2,\ 3,\ 4,\ 5$ and 6 states in ^{48}Ti. Thus the DIAS in ^{48}Ti ($E_{\mathrm{ex}} = 17$ MeV, $T = 4$, $J^\pi = 0^+$) is accessible by the DGT transitions.

In the case of ^{48}Ca target, the initial isospin is $T = 4$. Figure 5.8 shows the shell

model calculation in which each component of isospin of the final state is shown. The transition to double isobaric analogue state with the DGT transition is buried under the main component of $T = 2$. Study on other targets, e.g. less neutron-rich nucleus like ^{42}Ca might be used for the calibration study. It is known that the single GTGR from ^{42}Ca is less developed than ^{48}Ca and there is more chance of observing the peak of the transitions of DIAS in the double charge exchange spectrum.

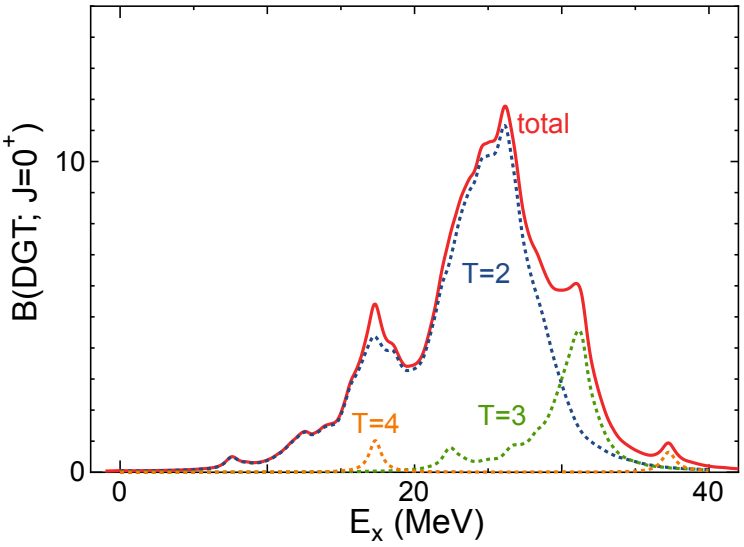

Figure 5.8: Shell model calculation for ^{48}Ca and its isospin break down [9].

From the viewpoint of providing information on the spin-isospin involved interaction, it would be useful to interpret the experimental result with $\pi + \rho + g'$ model. In the analysis of single GTGR and quasi elastic scattering, the short-range repulsive term of the effective interaction (g') was obtained as 0.5-0.7 [26]. Based on the discussion of the determination of the centroid energy of the DGTGR using double and quartic commutator relations [107], the centroid energy of the DGTGR should be formulated by using g' in a similar manner as in the case of the single GTGR. It is interesting to see the prediction on the centroid energy, which should be rather sensitive to the value of g'. This discussion will lead to the inspection of the model.

The transitions other than DGT discussed in this thesis, for example, double spin dipole or GT⊗IVSM, have never been examined theoretically. More detailed expectations of the centroid energy or width than the simple superposition of the single processes would be effective to subtract such components from the observed structure.

Chapter 6

Conclusion

The experimental observation of the double Gamow–Teller giant resonance (DGTGR) is essentially important to understand the collective modes of nucleus. The experimental observation of DGTGR can open a way to examine whether the harmonic picture holds or not in the oscillation in such a purely quantum mechanical coordinate of spin. Not only DGTGR, but any high excited states with DGT transition have not been known. The information on the DGTGR is desired as it would provide constraints on the nuclear matrix element of neutrino-less double β decay.

The experimental technique to access the double Gamow-Teller strengths in the highly excited state using the heavy-ion double charge exchange (^{12}C, ^{12}Be(0^+_2)) reaction was devised. In the present work, this method was applied for the first time to the measurement on a ^{48}Ca target using a high-intensity 250-MeV/nucleon ^{12}C primary beam at RIBF. Introduction of the dispersion matching technique resulted in the energy resolution of 1.5 MeV which is high enough to investigate DGTGR. The identification of ^{12}Be(0^+_2) in the final state through delayed γ-ray detection were successfully demonstrated. The reduction of background particle, mainly consisting of tritons and ^{6}He, using degraders and the magnetic system worked satisfactorily, which resulted in the achievement of the signal-to-noise ratio of 9:1. It is a factor of 9 improvement from the pilot experiment at RCNP.

The double charge exchange cross section with double spin and isospin flips has been identified at the energy region which cannot be accessed by the double β decays. In the cross section data, enhancements at the most forward angle of 0–0.3° are found in the energy regions of 14–22, 26–30, and 34–42 MeV. The forward peaking angular distributions suggest that the $\Delta L = 0$ transition components, namely the DGT transitions, exist in the region. The cross section of ^{48}Ca(^{12}C, ^{12}Be(0^+_2)) integrated over 0–34 MeV was obtained at 0–0.3° as 1.33 ± 0.12 μb/sr. This is the first identification of double spin and isospin flip transitions at energy $>$ 100 MeV/nucleon where the nucleon-nucleon interaction is weakest and isospin flip transitions are most strongly induced.

The possible DGT components in the observed cross section are analyzed by means

of the two-step DWBA framework using ECIS97. The (^{12}C, ^{12}Be(0^+_2)) cross section is calculated with the global optical potential in Ref. [7] and the transition form factor obtained by double folding the projectile and the target transition densities. The validity of the calculations is confirmed for the case of the single charge exchange ^{48}Ca(^{12}C, ^{12}B)^{48}Sc reaction. The multipole decomposition analysis based on the calculation is applied to the measured cross sections of ^{48}Ca $\rightarrow$ ^{48}Ti(0^+) transition. It shows that 38^{+26}_{-8}% of the $\theta \leq 0.3^\circ$ cross section observed in the $E_{\rm ex} \leq 34$ MeV is likely to be attributed to the DGT transition, which corresponds to the DGT strength of 28^{+22}_{-7}.

The quantitative evaluation of the centroid energy E_c and width Γ of the B(DGT) was performed. The deduced values of $E_c = 23 \pm 3$ MeV and $\Gamma = 6 \pm 1$ MeV are the first benchmark. The discussion on the anharmonicity is not clear in the present result, but the future high-statistics experiment will give more clear insight.

The enhancement in the spectrum around 36 MeV is not accounted for in our current framework. It might indicate that our current understanding of the reaction mechanism is insufficient. Further studies from both experimental and theoretical sides are needed for a better assessment of the DGTGR.

The present work clearly demonstrates that the new experimental method with the (^{12}C, ^{12}Be(0^+_2)) is a promising approach to DGT transitions at high excitation energies. However, the limited statistics do not allow us to draw sufficiently quantitative conclusions. A future high-statistics experiment will enable a more quantitative discussion on the DGTGR. Based on the experiences in the present work, possible improvement of 40-times higher statistics with the optimization of the experimental conditions and the selection of the target nucleus is conceived. It will enable the determination of the centroid energy of the DGTGR by 0.8 MeV precision, which would make possible to provide information on the nuclear process in the DGT transition, including the neutrino-less double β decay.

Acknowledgements

The present work would not have been completed without the kind supports from many people. First of all, I would like to thank Prof. Tomohiro Uesaka who is the spokesperson of the experiment. He provided me the opportunity to work on this experiment, and supported me to achieve the conduction of the experiment and the analysis of the data. I would like to thank Prof. Kentaro Yako who is my supervisor in CNS. He gave many fruitful advice to me continuously and I learned many through the discussion with him. I would like to thank Prof. Shinsuke Ota, who greatly contributed to the conduction of the experiment. I did not know anything as this was my first experiment at RIBF, and it would not have been completed without his dedication. He also helped me with the data analysis.

I would also like to thank Prof. Kenta Itahashi, the spokesperson of the pionic atoms spectroscopy, who introduced me to Prof. Uesaka. Because this experiment was performed with collaborating the group of the pionic atoms spectroscopy, I was also supported by him at the stage of the planning and the preparation of the experiment. I would like to thank Mr. Shota Matsumoto who dedicated himself with me to the preparation and the conduction of the series of experiments of DGTGR and pionic atoms.

For the reaction calculation and the interpretation of the result, I was helped by Prof. Noritaka Shimizu. The discussion with him helped greatly to enhance the result of this work.

I'm grateful to all of the collaborators: H. Baba, T. Chillery, P. Doornenbal, M. Dozono, N. Ebina, N. Fukuda, N. Fukunishi, T. Furuno, S. Hanai, T. Harada, S. Hayakawa, Y. Hijikata, K. Horikawa, S. W. Huang, N. Imai, N. Kobayashi, Y. Kondo, J. Li, Y. Maeda, T. Matsui, R. Matsumura, S. Michimasa, N. Nakatsuka, T. Nishi, K. Sakanashi, M. Sasano, R. Sekiya, N. Shimizu, Y. Shimizu, S. Shimoura, T. Sumikama, D. Suzuki, H. Suzuki, M. Takaki, S. Takeshige, H. Takeda, J. Tanaka, Y. K. Tanaka, Y. Togano, R. Tsuji, Z. H. Yang, K. Yoshida, M. Yoshimoto, and J. Zenihiro.

Besides the collaborators, I was helped by Dr. Tomoo Hasebe for providing the graphene sheet, Prof. Tomokazu Suzuki for transporting the ^{48}Ca target from RCNP, Prof. Atsushi Tamii and Prof. Kenjiro Miki for advising on the preparation of the article.

As members of Exotic Nuclear Reaction group in CNS, I was helped by Dr. Fumitaka Endo and Mr. Keita Kawata. The discussion with them stimulated my work and I was

encouraged by their work.

I would like to thank the people who supported me when I was in Kyoto University. First, I would like to thank Prof. Tomofumi Nagae who was the chief of the Nuclear and hadronic physics laboratory. I was helped by him since I was an undergraduate student and was given many fruitful advice. I would like to thank Prof. Hiroyuki Fujioka who was my supervisor in Kyoto, when I was involved in the project of pionic atoms spectroscopy at RCNP. I learned many basic things which are necessary elements to conduct research, and I am on the basis of them. I would like to thank Prof. Takahiro Kawabata who was also my supervisor in Kyoto. I was greatly helped in the experiment at RCNP. In addition to that, he gave me continuous spiritual support and fruitful discussions. I would like to thank Prof. Megumi Naruki who provided many advice in the daily discussion and helped me greatly in the completion of the thesis.

I greatly enjoyed my life at Kyoto as well as at Wako. I would like to thank all the members in the Nuclear and hadronic physics laboratory, Nuclear dynamics research group at RIKEN Nishina Center, and CNS. Especially, I was greatly helped by Dr. Reiko Kojima in daily life at CNS. I always enjoy working with her and I was also encouraged by her many times.

Finally, I would like to thank my family who supported me in all aspects of my life.

Appendix A

Analysis of 1/3-cell staggered MWDCs at F5

A.1 Configuration of MWDCs at F5

The MWDCs have configurations with sets of 1/3-cell staggered three-layer structures, X-X'-X" (the axis vertical to the wire direction is 0° against x axis), U-U'-U" (30°), and V-V'-V" ($-30°$). See Fig. 3.8 in Sec. 3.2.1 for details. This configuration was devised in order to lessen the bias which appears with the usual configuration in high statistics. Comb-like structures are seen in every 5 mm which correspond to the wire structures of the MWDCs [108]. The redundant configuration was adopted in which the discarding of information is possible if it is in unfavorable condition, for example, the hit position is close to the wires.

A.2 Correction of the wire placement

The origin of the wire position is corrected. In order to lessen the bias due to the concerned plane itself, the position is used which is determined by a tracking using all planes except three planes that have the same direction to the concerned plane in the same chamber. The left panel of Fig. A.1 shows an example of the correlation between the measured drift time and the position projected to the plane. Here the data in MWDC2 (downstream one) U" plane is shown. The vertical axis shows the position which is projected to the u_3 axis (See Fig. 3.8 in Sec. 3.2) obtained by the tracking with 15 planes, without U, U', and U" plane in MWDC2. The horizontal axis shows the drift time measured at U" in MWDC2. The central position of the distribution is determined with Gaussian fits for sliced distributions. The right panel of Fig. A.1 shows the extracted position against the timing. The position is fitted by a quadratic and the obtained vertex corresponds to the offset of the position. The obtained offsets are listed in Table A.1.

The obtained offsets seem to systematically deviate from the origin:

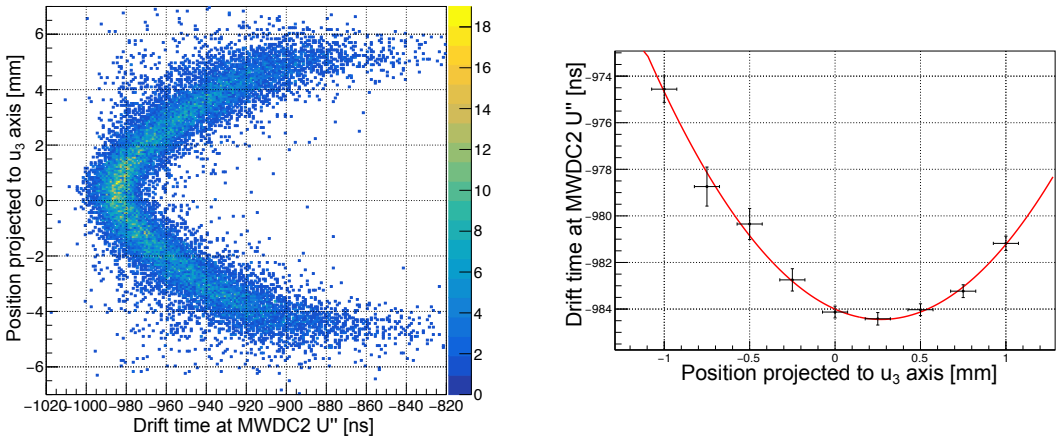

Figure A.1: Left: The position which is projected to u_3 axis against the drift time in U" plane. Right: the distribution of the left panel was fitted by quadratic.

- The offsets in X, X', and X" planes are all negative and others are positive.
- The offsets among the planes which have the same wire direction are similar with each other.

For these reasons, the offsets are supposed to be attributed to misplacement during the manufacturing of the MWDCs. The correction was adopted such that the offset for X_i planes is 0.152 mm which is the average value among the evaluated offset of X_i, and $0.152 \times \cos(30°) = 0.1316$ mm for U_i and V_i planes.

The deviations from the origin evaluated after the correction of the offset are summarized in Table. A.2. The values have been improved and are sufficiently close to 0.

A.2.1 Position resolution in each plane

The position resolution was evaluated by $\sqrt{\sigma_{\rm in} \cdot \sigma_{\rm ex}}$, where σ_{in} and σ_{ex} are the standard deviations of the position distribution determined by tracking with and without the concerned plane [109]. The $\sigma_{\rm in}$ were evaluated from the standard deviation of the distributions of residues of the hit position from the position determined by the tracking with 18 planes. The $\sigma_{\rm ex}$ were evaluated in the same way as $\sigma_{\rm in}$ but the tracking with 17 planes except the concerned plane. The position resolution at each plane is evaluated by $\sqrt{\sigma_{\rm in} \cdot \sigma_{\rm ex}}$. The obtained values are listed in Tables A.3 and A.4. The typical resolution is 0.3 mm.

Table A.1: The offset evaluated by the tracking with 15 planes.

Plane	Offset [mm]
MWDC1 x1	−0.170
MWDC1 x2	−0.186
MWDC1 x3	−0.131
MWDC1 u1	0.232
MWDC1 u2	0.298
MWDC1 u3	0.444
MWDC1 v1	0.282
MWDC1 v2	0.348
MWDC1 v3	0.363
MWDC2 x1	−0.161
MWDC2 x2	−0.162
MWDC2 x3	−0.102
MWDC2 u1	0.235
MWDC2 u2	0.197
MWDC2 u3	0.270
MWDC2 v1	0.234
MWDC2 v2	0.258
MWDC2 v3	0.237

Table A.2: The offset evaluated by the tracking with 15 planes after the correction of offset.

plane	Offset after correction [mm]
MWDC1 x1	−0.007
MWDC1 x2	−0.007
MWDC1 x3	0.024
MWDC1 u1	−0.005
MWDC1 u2	0.011
MWDC1 u3	−0.0006
MWDC1 v1	−0.060
MWDC1 v2	0.034
MWDC1 v3	0.010
MWDC2 x1	0.008
MWDC2 x2	−0.016
MWDC2 x3	0.043
MWDC2 u1	−0.010
MWDC2 u2	−0.098
MWDC2 u3	0.092
MWDC2 v1	0.067
MWDC2 v2	−0.040
MWDC2 v3	−0.030

Table A.3: The standard deviation of the residual distribution at each planes in MWDC1.

Plane	σ_{in} [mm]	σ_{ex} [mm]	$\sqrt{\sigma_{in}\sigma_{ex}}$ [mm]
x1	0.245	0.281	0.262
x2	0.242	0.281	0.261
x3	0.247	0.287	0.266
u1	0.204	0.286	0.241
u2	0.205	0.274	0.237
u3	0.029	0.295	0.248
v1	0.203	0.287	0.241
v2	0.198	0.277	0.234
v3	0.202	0.284	0.240

Table A.4: The standard deviation of the residual distribution at each planes in MWDC2.

Plane	σ_{in} [mm]	σ_{ex} [mm]	$\sqrt{\sigma_{in}\sigma_{ex}}$ [mm]
x1	0.290	0.351	0.319
x2	0.282	0.335	0.307
x3	0.289	0.344	0.315
u1	0.265	0.379	0.317
u2	0.262	0.365	0.310
u3	0.273	0.379	0.321
v1	0.265	0.374	0.314
v2	0.272	0.378	0.321
v3	0.270	0.368	0.315

A.3 Bias in the usual analysis

Fig. A.2 shows the distribution of the position projected to the V' axis, which is determined in usual analysis. The comb-like structure appears at every 5 mm, which corresponds to the interval between the sense wires and potential wires. This is attributed to the conversion between the observed drift time *dt* and the drift length *dl* having a bias.

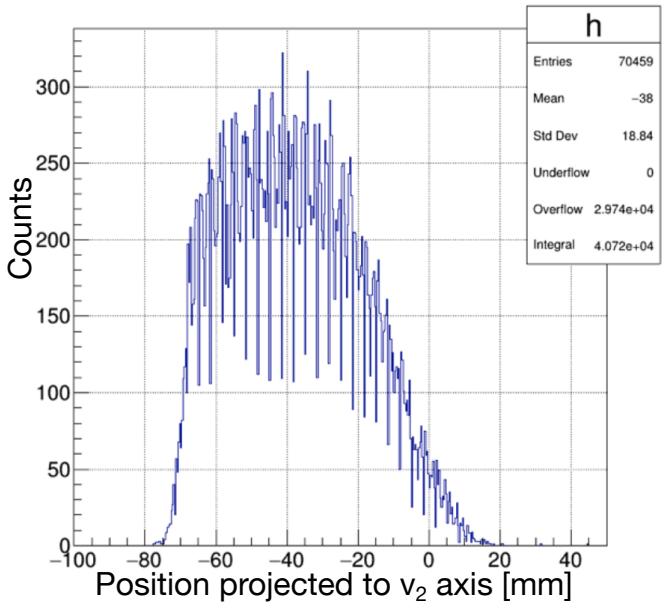

Figure A.2: The tracking result at MWDC2 V' plane which is projected to v_2 axis with usual analysis.

In the usual analysis, the drift time to distance (*dt-dl*) conversion was obtained by assuming that the particle number in a cell is distributed uniformly by averaging the distribution of all wires in one plane. This function suffers from a bias coming from the resolution of the drift time. Figure A.3 shows the correlation between the position (cell size of 5 mm is scaled to 1 in the figure) in a plane and the drift time. The position is determined with the tracking using the 17 planes except the concerning plane and with the *dt-dl* conversion obtained in the first trial. The red curve in the figure shows the *dt-dl* conversion determined with the conventional method. The conversion curve overestimates the position as a whole. It is understood that the bias arises from the assumption that the start and the end of the *dt* distribution correspond to the *dl* of 0 mm and 5 mm, respectively. Considering the timing resolution, the maximum *dl* should be over 5 mm. The spread out of the events are compressed in the cell size in making the conversion function. In addition, the resolution is poor at the *dl* is short region, and the drift time is degenerated for 0–~0.5 mm. The determination of the conversion is also difficult in the *dl* is long region.

In order to avoid these troubles, the following analysis is adopted:

- *dt-dl* conversion is refined for middle region of the drift length
- The information of *dl* is not used which is close to wires

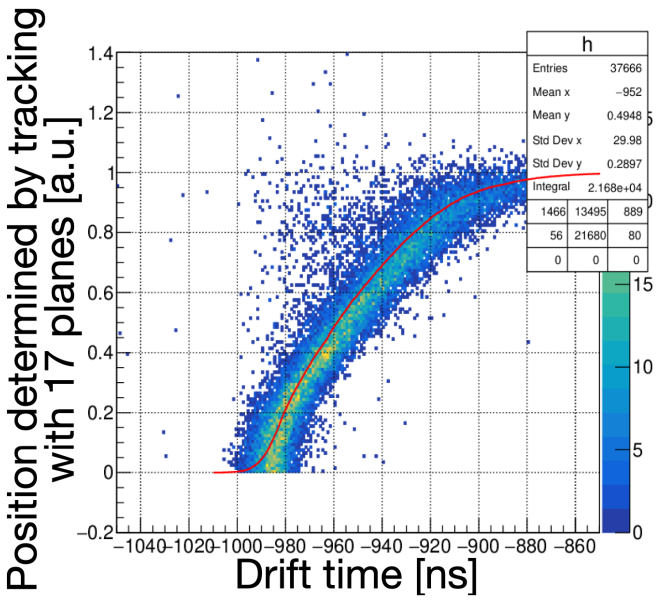

Figure A.3: The position determined by the tracking with 17 planes against the drift time. Red line shows the *dt-dl* conversion determined with the conventional way.

A.4 Refining the *dt-dl* conversion

The drift time to distance (*dt-dl*) conversion is obtained by iterative analysis. The first function is obtained in the conventional way described above. This first *dt-dl* conversion is refined by making the correspondence between the observed time and the position determined using the tracking without the concerned plane. Figures A.4 and A.5 show the correlation between the position and the drift time in each plane. The positions are determined with the tracking using 15 planes except the planes which have the same direction and the same chamber to the concerned plane. Here we excluded 3 planes from the tracking, not only one plane, in order to lessen the bias.

The conversion functions are obtained by fitting the correlation with suitable functions. For MWDC1,

$$\frac{5.2}{1+\exp\{(-p_0(x-p_1))\}} + p_2 \sin\left(p_3(x-p_4)\right). \tag{A.1}$$

For MWDC2,

$$p_0 + p_1\sqrt{x-p_2} + p_3 x + p_4 x^2. \tag{A.2}$$

The fitted results are also shown in the figures by the red curves.

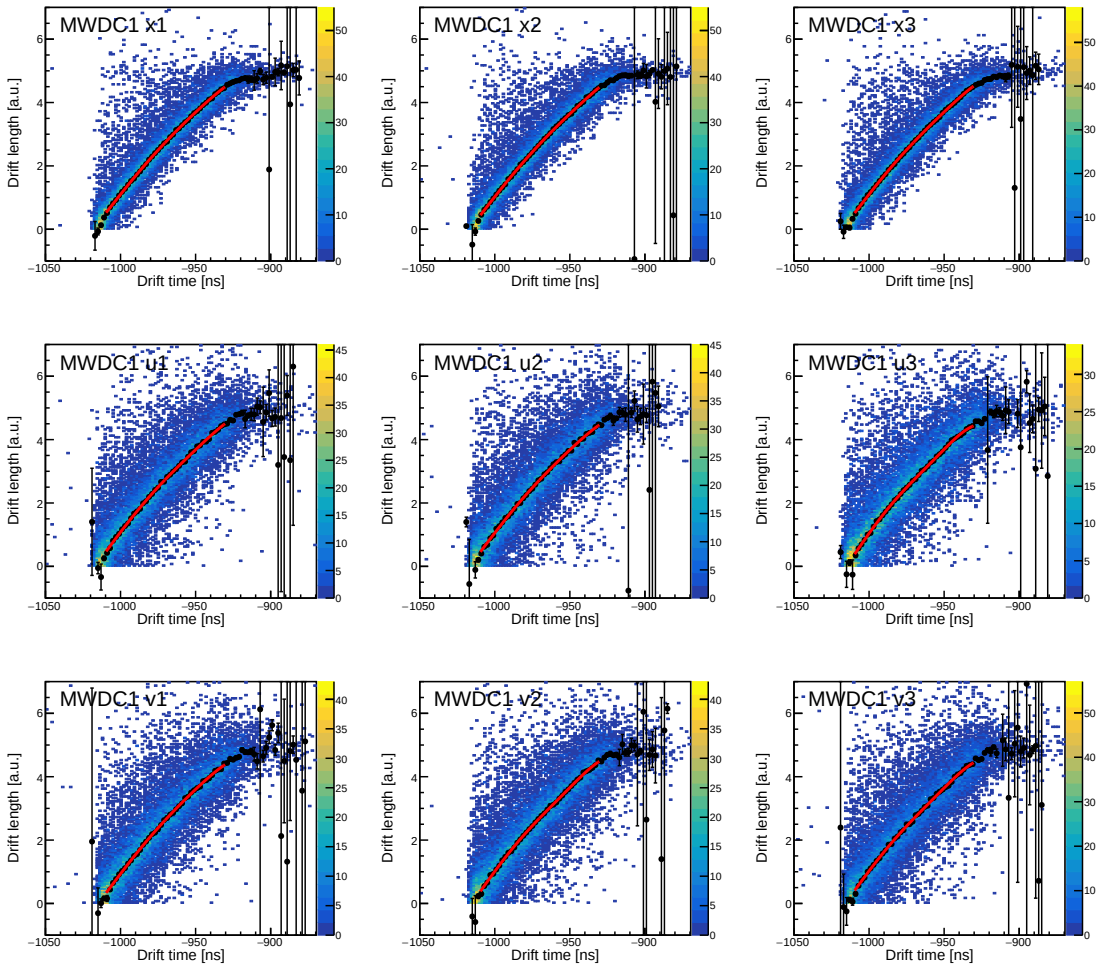

Figure A.4: The drift time and the position determined by the tracking using 15 planes. The newly obtained *dt-dl* curves are overlaid with red lines. This figures show the data for MWDC1.

A.5 Rejection of the hit which is close to wires

In order to lessen the bias arising from the closeness to the wire, we adopted the tracking without the planes in which the hit position is close to the wires.

The trajectory of the particle was determined by the least squares method. The position in each plane X_i is determined so that the following χ^2 is minimized,

$$\chi^2 = \sum_i^N \frac{(X_i - x_i)^2}{\sigma_i^2}, \tag{A.3}$$

where $N = 18$ is the number of planes used in the analysis. X_i is the position to be determined. The set of X_i is linear as a function of z. x_i is the observed position along the axis. σ_i expresses the resolution in ith plane. The contribution of the plane which we

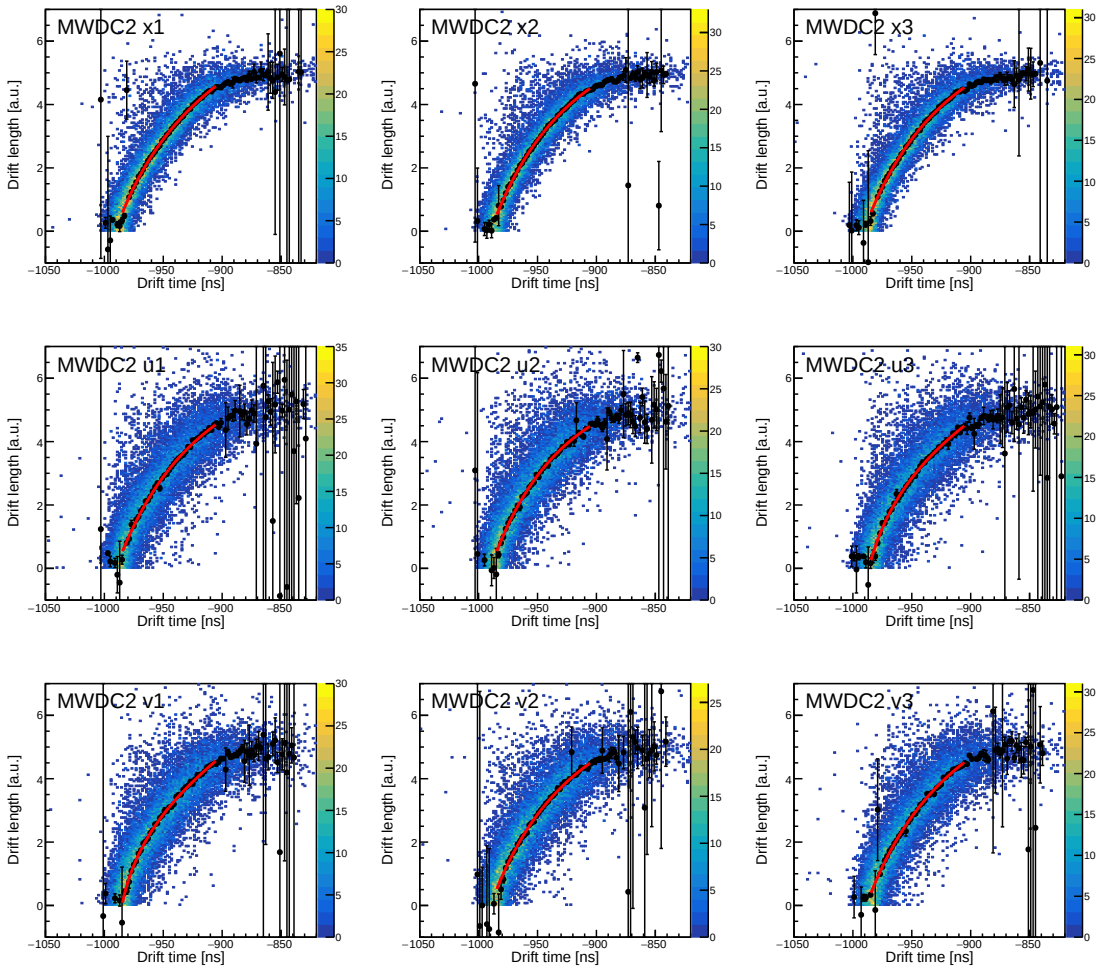

Figure A.5: Same as Fig. A.4 but the data for MWDC2.

want to exclude is effectively reduced by increasing the σ_i. σ_i = 0.3 mm was applied for the hit in which 0.6 < dl < 4.4 mm. This value corresponds to the evaluated resolution in each plane. For the planes dl < 0.6 mm and dl < 4.4 mm, σ_i = 2.0 mm was applied. Figure A.6 shows a schematic diagram of the placement of the planes and wires. The worse resolution was adopted for the colored region. In the example in the figure, the incident particle makes signals at the wires of (i + 1)th of X plane, (i + 1)th of X' plane, and (i + 1)th of X" plane. For the particle with the incident angle of < 47 mrad, two planes within three are active. In the region we are interested in, the event with > 47 mrad is negligible.

The worse resolution of 2.0 mm was determined so as to provide information about left-right ambiguity even though it does not contribute to the tracking.

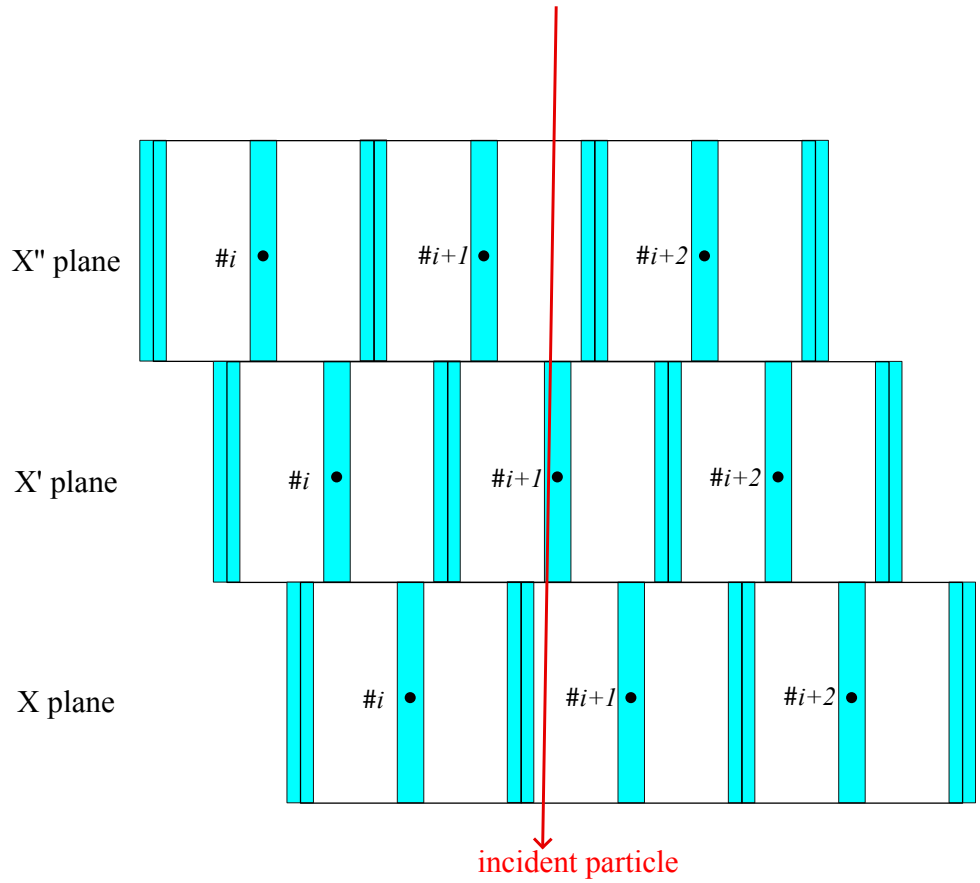

Figure A.6: Schematic diagram of the placement of the wires in cells of the MWDC. Blue regions indicate the insensible region.

A.6 Evaluation of the tracking resolution

The position and angular resolutions for the tracking results are evaluated by assuming that the position resolution at each plane is 0.3 mm, as evaluated in Sec. A.3. In the determination of the track by the least squares method, the result of the tracking, X, Y, a, and b are expressed as the linear combinations of the hit position at each plane. The resolution of the position and the angle, ΔX, ΔY, Δa, and Δb are evaluated by multiplying the resolution in a plane, 0.3 mm, and the quadratic sum of the coefficients. The number of the planes which effectively contribute to the tracking is typically 12. The coefficients are when using 12 planes of X, X", U, U", V, V" in MWDC1 and MWDC2. The resolutions for tracking are $\Delta X = 0.1$ mm, $\Delta Y = 0.2$ mm, $\Delta a = 0.3$ mrad, and $\Delta b = 0.7$ mrad.

Appendix B

Supplements of the reaction calculation

B.1 Angular smearing

The calculated angular distributions were smeared with experimental angular resolution and re-binned to the angular region used in the MDA. The angular resolutions were evaluated as the amounts which are projected to the horizontal or vertical direction, i.e. a and b. The experimental resolutions were $\Delta a = 0.15^\circ$ and $\Delta b = 0.17^\circ$ in the laboratory system, which correspond to $\Delta a = 0.20^\circ$ and $\Delta b = 0.22^\circ$ in the center of mass frame. We obtained the smeared distribution using the Monte-Carlo method.

The expected counts in an infinitesimal solid angle are

$$dn = \frac{d\sigma}{d\Omega}(\theta) \cdot d\theta \cdot d\phi \cdot \sin(\theta). \tag{B.1}$$

The events are generated dn times in a grid of θ and ϕ with the interval of $d\theta$ and $d\phi$. Here $d\theta = 0.01^\circ$ and $d\phi = 0.01^\circ$ are taken. Each θ and ϕ are converted to a and b, and a and b are smeared with the resolution of Δa and Δb by the Gaussian distribution. The smeared a and b are converted to θ and ϕ again, and the distribution of the counts on θ is obtained.

In order to perform the MDA, the smeared distribution of the cross section is re-binned to the angular region of 0–0.3°, 0.3–0.5°, and in 0.2° intervals for large angles up to $\theta_{\mathrm{CM}} = 1.9^\circ$. These are obtained by integrating the smeared cross section within each angular region and divided by the solid angle. The lines in Fig. B.1 show the angular distributions of the calculated cross sections before smearing. The dots are smeared and re-binned points, which are used as the reference of the MDA calculation.

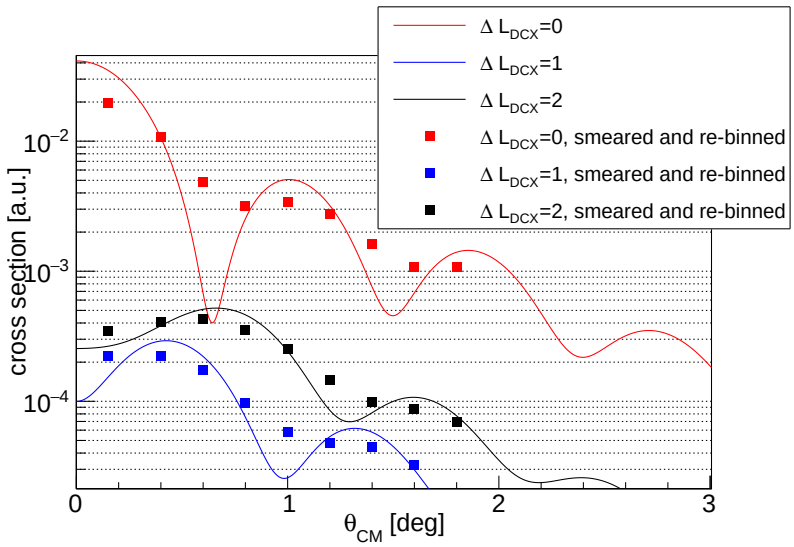

Figure B.1: Calculated angular distribution of $\Delta L_{\mathrm{DCX}} = 0,\ 1,\ 2$ (before smearing) and re-binned points for angular region used in MDA after smearing. Red, blue, and black lines and points correspond to $\Delta L_{\mathrm{DCX}} = 0,\ 1$, and 2 transition, respectively.

B.2 One body transition densities in projectile system

In the calculation of the form factors (Sec. 4.2), one body densities for the projectile system are calculated using the shell-model code NuShellX [91]. The obtained one body densities are listed in Table B.1 for the transition of ^{12}C $\rightarrow$ ^{12}B and Table B.2 for the transition of ^{12}B $\rightarrow$ ^{12}Be(0^+_2).

Table B.1: One body densities for ^{12}C $\rightarrow$ ^{12}B.

final orbit	initial orbit	Z
$0p1/2$	$0p1/2$	−0.08582
$0p1/2$	$0p3/2$	−0.71873
$0p3/2$	$0p1/2$	−0.23149
$0p3/2$	$0p3/2$	−0.07582
$0d5/2$	$0d5/2$	−0.00880
$0d5/2$	$0d3/2$	0.00030
$0d3/2$	$0d5/2$	−0.00404
$0d3/2$	$0d3/2$	−0.00214
$0d3/2$	$1s1/2$	−0.00100
$1s1/2$	$0d3/2$	−0.00042
$1s1/2$	$1s1/2$	−0.00068

Table B.2: One body densities for ^{12}B $\rightarrow$ ^{12}Be(0^+_2).

final orbit	initial orbit	Z
$0p3/2$	$0p3/2$	−0.08781
$0p3/2$	$0p1/2$	−0.04186
$0p1/2$	$0p3/2$	−0.28331
$0p1/2$	$0p1/2$	−0.07911
$0d5/2$	$0d5/2$	0.00391
$0d5/2$	$0d3/2$	−0.00125
$0d3/2$	$0d5/2$	0.00061
$0d3/2$	$0d3/2$	−0.00147
$0d3/2$	$1s1/2$	−0.00175
$1s1/2$	$0d3/2$	0.00189
$1s1/2$	$1s1/2$	0.01229

B.3 Q dependence of the angular distribution

Figures B.2, B.3, and B.4 show the angular distributions calculated with different Q-values, $-Q$ =0, and from 24 (correspond to the excitation energy in ^{48}Ti of 1 MeV) to 60 MeV at intervals of 8 MeV. For the $\Delta L_{\mathrm{DCX}} = 1$ and $\Delta L_{\mathrm{DCX}} = 2$ components, the diffraction patterns become slightly less sharp as the Q-value increased. The MDA was performed by each energy bin by considering the change in the angular distributions.

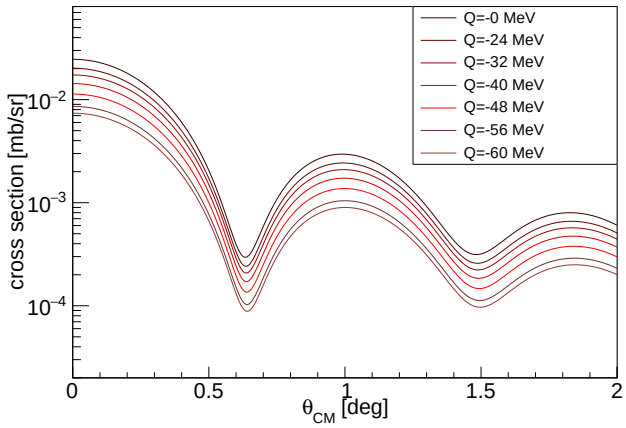

Figure B.2: Angular distributions of $\Delta L_{\mathrm{DCX}} = 0$ calculated with different Q-values.

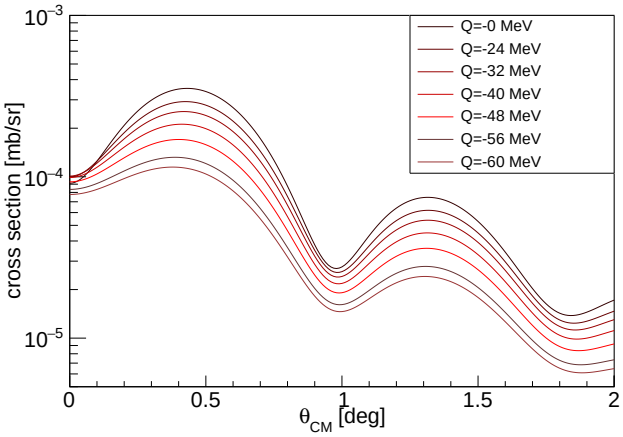

Figure B.3: Angular distributions of $\Delta L_{\mathrm{DCX}} = 1$ calculated with different Q-values.

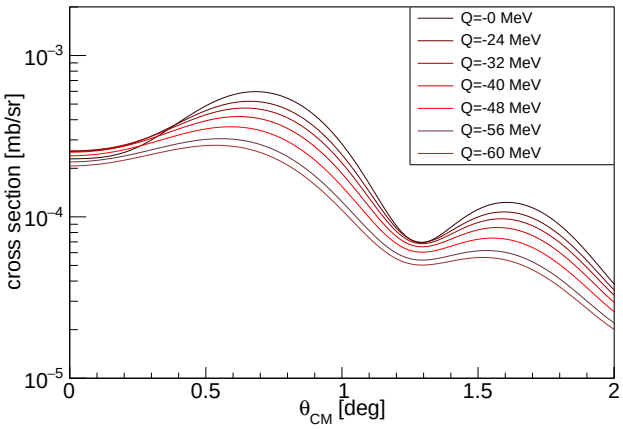

Figure B.4: Angular distributions of $\Delta L_{\mathrm{DCX}} = 2$ calculated with different Q-values.

Appendix C

Evaluation of errors in MDA

C.1 Error of the fit

The determination of the parameters are accompanied by the correlation. When the log likelihood is calculated for a set of parameters $\boldsymbol{\theta}$, The confidence region $\ln L(\boldsymbol{\theta}) \geq \ln L_{\max} - \Delta \ln L$, For three parameters, $2\Delta \ln L$ of 3.53 corresponds to the confidence region is 68.27% [100]. The widths of the contour in the parameter space were evaluated by the Minuit processor of MINOS [110].

Figure C.1 shows the example of the contour plots of $-\ln L$ projected to the two-dimensional parameter spaces. This example shows the fit for the energy bin of $34 < E_{\mathrm{ex}} < 38$ MeV. The vertical and horizontal axes correspond to the parameters of the fit, $L0$, $L1$, and $L2$, for $\Delta L_{\mathrm{DCX}} = 0$, $\Delta L_{\mathrm{DCX}} = 1$, and $\Delta L_{\mathrm{DCX}} = 2$, respectively. The black points show the contour of $\ln L_{\max} - \Delta \ln L$ where $\Delta \ln L = 3.53/2$. The red triangles denote the maximum points of $\ln L(\boldsymbol{\theta})$. The bars extended from the triangles denote the errors evaluated by MINOS and correspond to the width of the contour plots.

C.2 Estimation of the error for the sum of extracted strengths

The cross section of $\Delta L_{\mathrm{DCX}} = 0$ components and B(DGT) were evaluated with errors at each energy bin. The errors of the integrated values were evaluated by randomly generating sets of values and summing them by each event.

The distributions of the probability of the value of the cross sections which are determined by the fit are assumed to be Gaussian distributions. The standard deviations of the distribution were assumed to be the upper errors evaluated by MINOS. Nine values are generated independently. In the present case, the values have a physical boundary at 0. If the generated value has a negative value, the value was set to 0. Figure C.2 shows the generated events. Each panel corresponds to the value at each energy bin. The blue histograms show the generated events whose mean is the fit result and the standard deviation

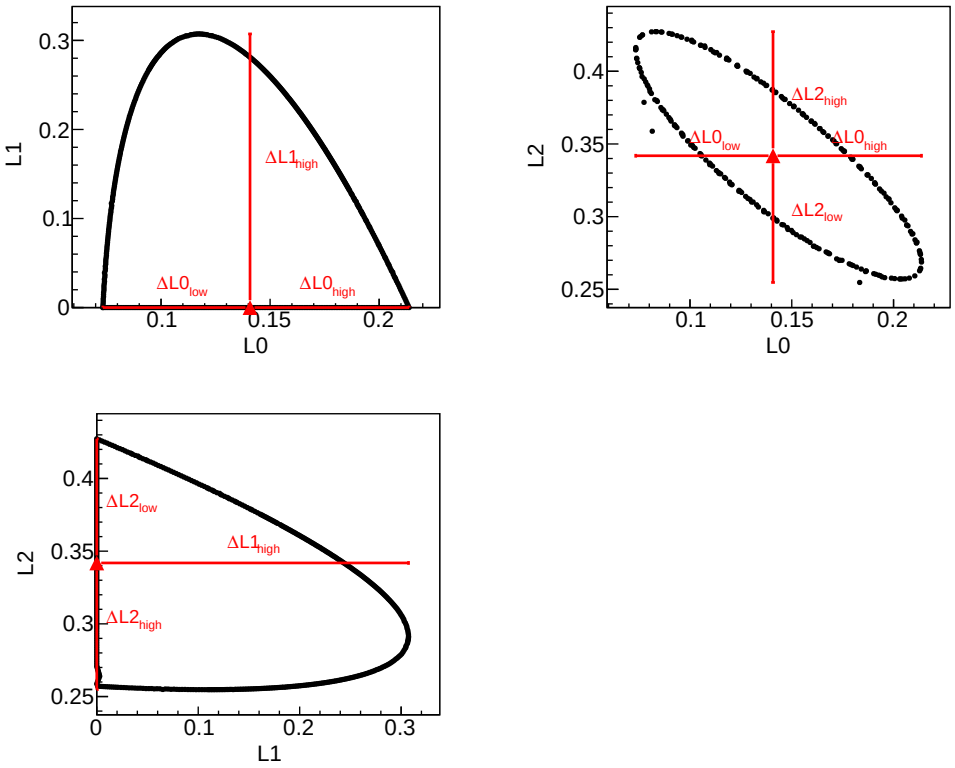

Figure C.1: Example of the contour plots of $\ln L$ in the parameter spaces for the data of $34 < E_{\rm ex} < 38$ MeV. $L0$, $L1$, and $L2$ are the fit parameters for $\Delta L_{\rm DCX} = 0$, 1, and 2, respectively. Each panel shows the space of $L0$ and $L1$ (top left), $L2$ and $L0$ (top right), and $L2$ and $L1$ (bottom).

is the upper error. The red histograms show the events in which negative values in the blue histograms are put into 0. The left panels show the distributions of the summed value for the blue histograms in Fig. C.2. The right panels shows the distribution of the summed value for the red histograms in Fig. C.2. The error of the summed value corresponding to 1σ was evaluated from the area of the distribution in the right panel of Fig. C.3. The upper limit of the summed value, $c_{\rm up}$ is determined so that the integrated number of event over $[c_{\rm up}, \infty)$ is 16% of the total events, shown as the filled area on the right side in the right panel of Fig. C.3. Similarly, the lower limit $c_{\rm low}$ is determined so that the integrated number of events over $(0, c_{\rm low}]$ is 16% of the total events.

The upper and lower limits of the sum ($S_{\rm up}$ and $S_{\rm low}$), centroid energy ($E_{\rm up}$ and $E_{\rm low}$), and width ($\Gamma_{\rm up}$ and $\Gamma_{\rm low}$) of B(DGT) are evaluated in the same way. Figure C.4 shows the distributions of sum (top panel), centroid energy (middle), and width (bottom) of B(DGT) calculated using the generated events. The upper and lower limits of these quantities are determined from the generated distributions.

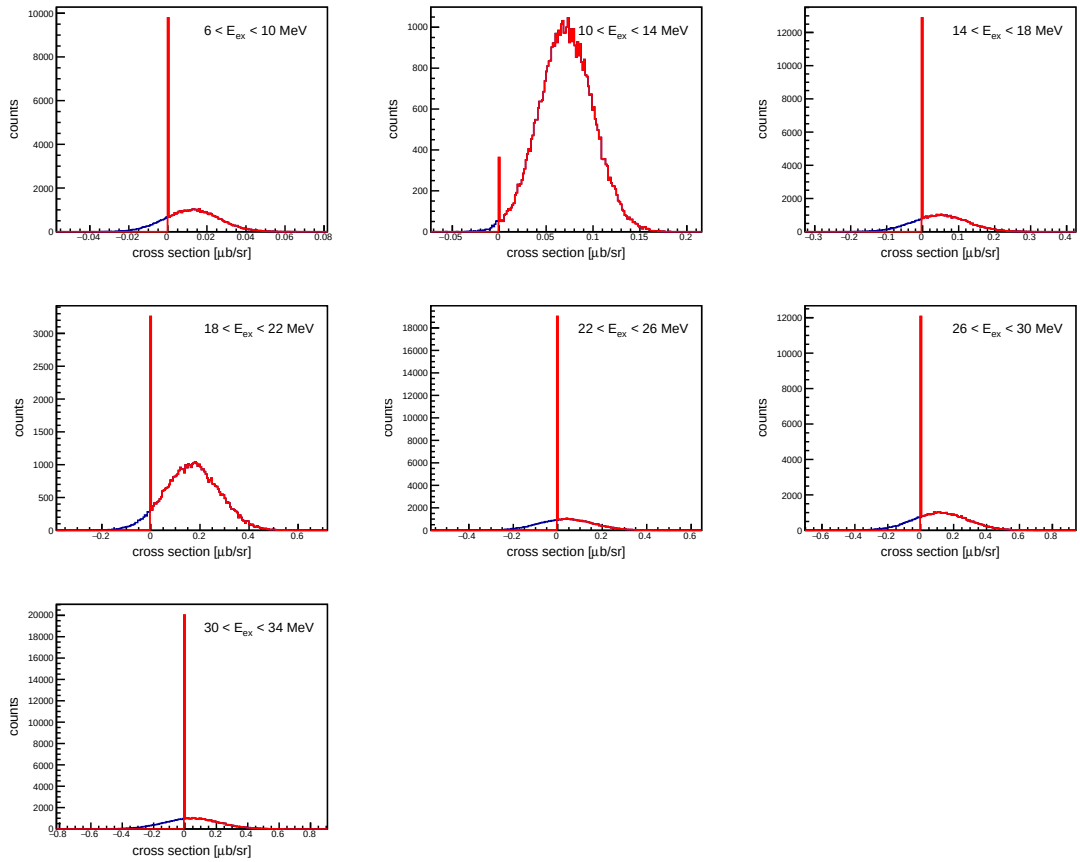

Figure C.2: Generated events at each energy bin. Blue histograms show the generated events without the limit by 0. Red histograms show the generated events with the limit by 0.

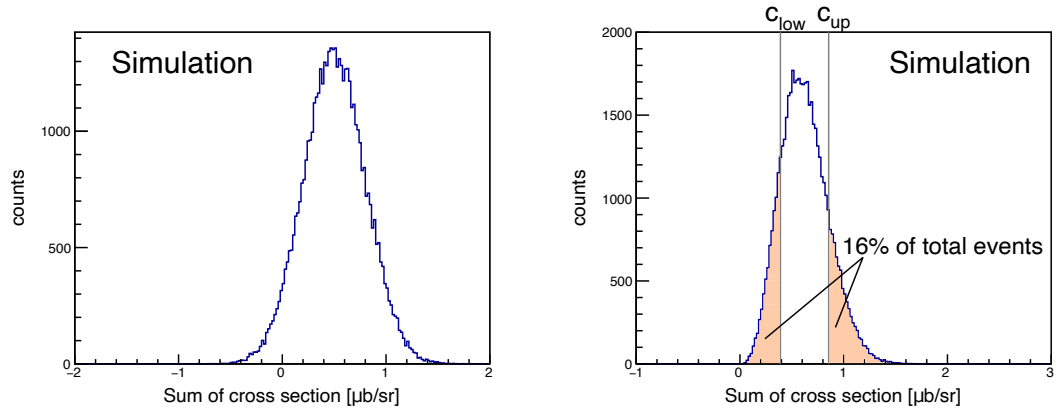

Figure C.3: Distributions of the sum of the generated cross sections. Left: Generated events are not limited by 0. Right: Generated events are limited by 0. The vertical lines shows the upper and lower errors. Each filled area corresponds to 16% of the area of the whole distribution.

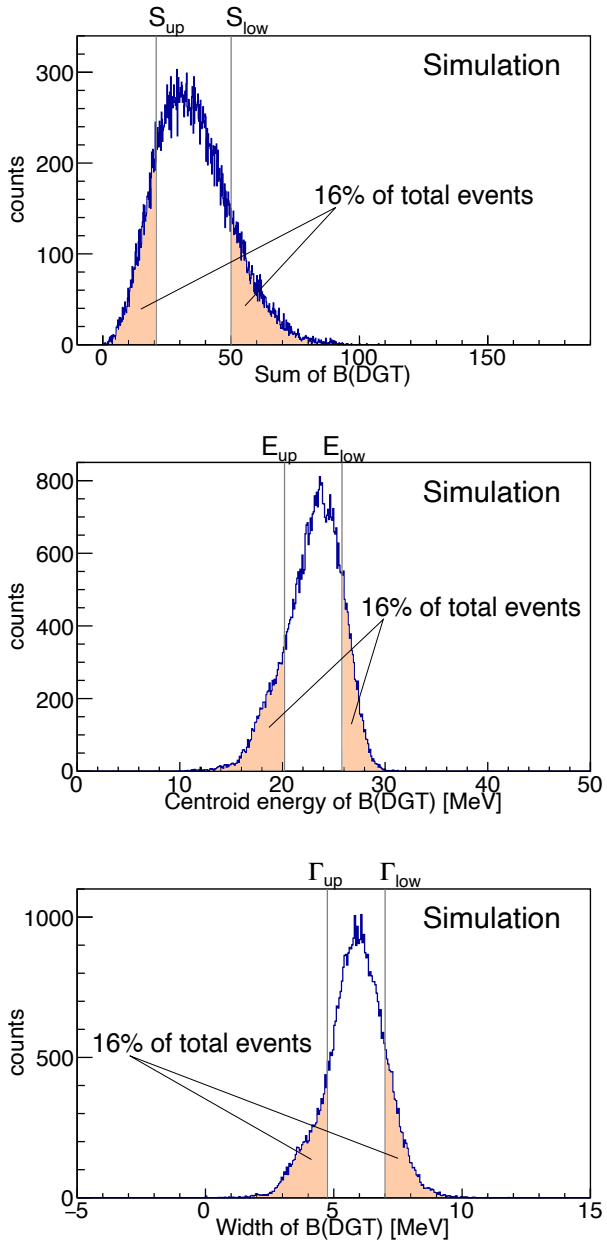

Figure C.4: Distributions of the sum (top panel), centroid energy (middle), and width (bottom) of B(DGT) calculated using the generated events.

References

[1] S. Mordechai *et al. Nature*, 352:393, 1991.

[2] H. Matsubara *et al. Few-Body Systems*, 54:1433, 2013.

[3] M. Takaki *et al. CNS Annual Report 2014*, 94:9, 2016.

[4] H. Okuno, N. Fukunishi, and O. Kamigaito. *Prog. Theor. Exp. Phys.*, 2012:03C002, 2012.

[5] H. Okuno, T. Dantsuka, M. Fujimaki, N. Fukunishi, H. Hasebe, Y. Higurashi, E. Ikezawa, N. Ikoma, H. Imao, O. Kamigaito, M. Kidera, M. Komiyama, K. Kumagai, T. Maie, M. Nagase, T. Nagatomo, T. Nakagawa, M. Nakamura, J. Ohnishi, K. Ozeki, N. Sakamoto, K. Suda, U. Uchiyama, S. Watanabe, T. Watanabe, Y. Watanabe, K. Yamada, and H. Yamasawa. *Journal of Physics: Conference Series*, 1401, 2020.

[6] T. Nishi *et al. Nucl. Instrum. Methods Phys. Res. B*, 317:290, 2013.

[7] T. Furumoto, W. Horiuchi, M. Takashina, Y. Yamamoto, and Y. Sakuragi. *Phys. Rev. C*, 85:044607, 2012.

[8] N. Shimizu, J. Menéndez, and K. Yako. *Phys. Rev. Lett.*, 120:142502, 2018.

[9] N. Shimizu. Private communication. unpublished.

[10] S. Abe *et al. Phys. Rev. Lett.*, 130:051801, 2023.

[11] M. N. Harakeh and A. van der Woude. *Giant Resonances Fundamental High-Frequency Models of Nuclear Excitation*. Oxford Science Publications, 2001.

[12] J.P. Blaizot, D. Gogny, and B. Grammaticos. *Nuclear Physics A*, 265:315, 1976.

[13] P. Carlos, H. Beil, R. Bergère, A. Leprêtre, A. De Miniac, and A. Veyssière. *Nucl. Phys. A*, 225:171, 1974.

[14] G. E. Brown and M. Bolsterli. *Phys. Rev. Lett.*, 3:472, 1959.

[15] D.J. Thouless. *Nuclear Physics*, 22:78, 1961.

[16] A. B. Migdal. *Rev. Mod. Phys.*, 50:107, 1978.

[17] J. Meyer-Ter-Vehn. *Physics Reports*, 74:323, 1981.

[18] T. Suzuki. *Nucl. Phys. A*, 379:110, 1982.

[19] T. Wakasa, M. Ichimura, and H. Sakai. *Phys. Rev. C*, 72:067303, 2005.

[20] T. Wakasa, M. Okamoto, M. Dozono, K. Hatanaka, M. Ichimura, S. Kuroita, Y. Maeda, H. Miyasako, T. Noro, T. Saito, Y. Sakemi, T. Yabe, and K. Yako. *Phys. Rev. C*, 85:064606, 2012.

[21] J. Yasuda *et. al*. *Physical Review Letters*, 121:132501, 2018.

[22] K. Ikeda *et al. Phys. Lett.*, 3:271, 1963.

[23] C. Gaarde, J.S. Larsen, M.N. Harakeh, and M. Igarashi. *Nucl. Phys. A*, 369:258, 1980.

[24] T. N. Taddeucci *et al. Nucl. Phys. A*, 469:125, 1987.

[25] C. Gaarde. *Nucl. Phys. A*, 396:127, 1983.

[26] M. Ichimura, H. Sakai, and T. Wakasa. *Prog. Part. Nucl. Phys.*, 56:446, 2006.

[27] F. Osterfeld. *Rev. Mod. Phys.*, 64:491, 1992.

[28] S. Nakayama, H. Akimune, I. Daito, H. Fujimura, Y. Fujita, M. Fujiwara, K. Fushimi, T. Inomata, K. Ishibashi, H. Kohri, N. Koori, K. Takahisa, A. Tamii, M. Tanaka, H. Toyokawa, and T. Yamagata. *Phys. Rev. C*, 60:047303, 1999.

[29] S. Noji *et al. Phys. Rev. Lett.*, 120:172501, 2018.

[30] S. Nakayama, T. Yamagata, M. Tanaka, M. Inoue, K. Yuasa, T. Itahashi, H. Ogata, N. Koori, and K. Shima. *Phys. Rev. Lett.*, 67:1082, 1991.

[31] Ph. Chomaz and N. Frascaria. *Physics Reports*, 252:275, 1995.

[32] D. Brink. *Ph.D. thesis*, 1955.

[33] P. Axel. *Phys. Rev.*, 126:671, 1962.

[34] S. Mordechai *et al. Phys. Rev. Lett.*, 60:408, 1988.

[35] S. Mordechai *et al. Phys. Rev. Lett.*, 61:531, 1988.

[36] J. Bar-Touv and S. Mordechai. *Phys. Rev. C*, 45:197, 1992.

[37] M. Fallot, Ph. Chomaz, M.V. Andres, F. Catara, E.G. Lanza, and J.A. Scarpaci. *Nucl. Phys. A*, 729:699, 2003.

[38] T. Aumann, P. F. Bortignon, and H. Emling. *Annu. Rev. Nucl. Part. Sci.*, 48:351, 1998.

[39] M. Fallot *et al. Phys. Rev. Lett.*, 97:242502, 2006.

[40] N. Auerbach, L. Zamick, and D. C. Zheng. *Annals of Physics*, 192, 1989.

[41] W. G. Love and M. A. Franey. *Phys. Rev. C*, 24:1073, 1981.

[42] J. Blomgren *et al. Phys. Lett. B*, 362:34, 1995.

[43] F. Cappuzzello *et al.* [NUMEN collaboration]. *Prog. Part. Nucl. Phys.*, 128 :103999, 2023.

[44] J. L. Ferreira, J. Lubian, F. Cappuzzello, M. Cavallaro, and D. Carbone. *Phys. Rev. C*, 105:014630, 2022.

[45] J. I. Bellone, S. Burrello, M. Colonna, J.A. Lay, and H. Lenske. *Physics Letters B*, 807:135528, 2020.

[46] E. Santopinto, H. García-Tecocoatzi, R. I. Magana Vsevolodovna, and J. Ferretti [NUMEN Collaboration]. *Phys. Rev. C*, 98:061601, 2018.

[47] C. Eke, I. Ciraldo, F. Cappuzzello, D. Carbone, M. Cavallaro, V. Soukeras, A. Spatafora, C. Agodi, I. Boztosun, G.A. Brischetto, D. Calvo, A. Hacisalihoglu, G. Lanzalone, R. Linares, N.H. Medina, J.R.B. Oliveira, A. Pakou, L. Pandola, O. Sgouros, S. Tudisco, and V.A.B. Zagatto. *Results in Physics*, 67:108037, 2024.

[48] K. Takahisa, H. Ejiri, H. Akimune, H. Fujita, R. Matumiya, T. Ohta, T. Shima, M. Tanaka, and M. Yosoi. arXiv:1703.08264 [nucl-ex], https://arxiv.org/abs/1703.08264, 2017.

[49] D. Ashery, M. S. Zisman, G. W. Goth, G. J. Wozniak, R. B. Weisenmiller, and Joseph Cerny. *Phys. Rev. C*, 13:1345, 1976.

[50] H. T. Fortune and R. Sherr. *Phys. Rev. C*, 74:024301, 2006.

[51] F. C. Barker. Technical report, 1976. J. Phys. G : Nucl. Phys Volume: 2 Issue: 4.

[52] A. Navin *et al. Phys. Rev. Lett.*, 85:266, 2000.

[53] S. D. Pain *et al. Phys. Rev. Lett.*, 96, 2006.

[54] R. Meharchand *et al. Phys. Rev. Lett.*, 108:122501, 2012.

[55] A. Bohr and B. R. Mottelson. *Nuclear Structure*, volume II. New York, 1975.

[56] I. Hamamoto and S. Shimoura. *Journal of Physics G: Nuclear and Particle Physics*, 34:2715, 2007.

[57] S. Shimoura *et al. Physics Letters B*, 560:31, 2003.

[58] S. Shimoura *et al. Physics Letters B*, 654:87, 2007.

[59] S. Novario, P. Gysbers, J. Engel, G. Hagen, G. R. Jansen, T. D. Morris, P. Navrátil, T. Papenbrock, and S. Quaglioni. *Phys. Rev. Lett.*, 126:182502, 2021.

[60] B. D. Anderson, T. Chittrakarn, A. R. Baldwin, C. Lebo, R. Madey, P. C. Tandy, J. W. Watson, B. A. Brown, and C. C. Foster. *Phys. Rev. C*, 31:1161, 1985.

[61] K. Yako *et al. Phys. Rev. Lett.*, 103:012503, 2009.

[62] M. Redshaw, G. Bollen, M. Brodeur, S. Bustabad, D. L. Lincolnd, S. J. Novario, R. Ringle, and S. Schwarz. *Phys. Rev. C*, 86:041306, 2012.

[63] T. Kishimoto. *International Journal of Modern Physics E*, 18:2129, 2009.

[64] K. Tetsuno *et al.* [CANDLES collaboration]. *Journal of Physics: Conference Series*, 1468:012132, 2020.

[65] M. Takaki *et al. CNS Annual Report 2017*, 97:23, 2019.

[66] Y. Yano. *Nucl. Instrum. Methods Phys. Res. B*, 261:1009, 2007.

[67] T. Kubo. *Nucl. Instrum. Methods Phys. Res. B*, 204:97, 2003.

[68] T. Nishi *et al. Phys. Rev. Lett.*, 120:152505, 2018.

[69] S. Takeuchi, T. Motobayashi, Y. Togano, M. Matsushita, N. Aoi, K. Demichi, H. Hasegawa, and H. Murakami. *Nucl. Instrum. Methods Phys. Res. A*, 763:596, 2014.

[70] N. Fukuda, T. Kubo, T. Ohnishi, N. Inabe, H. Takeda, D. Kameda, and H. Suzuki. *Nucl. Instrum. Methods Phys. Res. B*, 317:323, 2013.

[71] H. Takeda *et al. Nucl. Instrum. Methods Phys. Res. B*, 463:515, 2020.

[72] GICOSY. based on M. Berz, H.C. Hoffmann, H. Wollnik, *Nucl. Instr. Meth. A* 258:402, 1987. https://web-docs.gsi.de/ weick/gicosy/.

[73] S. A. Martin *et al. Nucl. Instrum. Methods*, 214:281, 1983.

[74] A. Sakaue *et al. RIKEN Accelerator Progress Report 2020*, 54:86, 2021.

[75] H. Miya *et al. Nucl. Instrum. Methods Phys. Res. B*, 317:701, 2013.

[76] S. Y. Matsumoto. *Master thesis*, 2017.

[77] S. Y. Matsumoto, A. Sakaue, K. Itahashi, T. Moriguchi, T. Nishi, R. Sekiya, R. Tsuji, T. Uesaka, K. Yako, and J. Zenihiro. *UTTAC Annual Report 2020*, UTTAAC-90:12, 2021.

[78] H. Kumagai, T. Ohnishi, N. Fukuda, H. Takeda, D. Kameda, N. Inabe, K. Yoshida, and T. Kubo. *Nucl. Instrum. Methods Phys. Res. B*, 317:717, 2013.

[79] H. Baba, T. Ichihara, T. Ohnishi, S. Takeuchi, K. Yoshida, Y. Watanabe, S. Ota, and S. Shimoura. *Nucl. Instrum. Methods Phys. Res. A*, 616:65, 2010.

[80] H. Baba *et al. RIKEN Accelerator Progress Report 2013*, 47:235, 2014.

[81] I. Kipnis *et al. IEEE Trans. Nucl. Sci.*, 44, 1997.

[82] H. Baba, T. Ichihara, T. Isobe, T. Ohnishi, K. Yoshida, Y. Watanabe, S. Ota, H. Shimizu, S. Shimoura, S. Takeuchi, D. Nishimura, J. Zenihiro, A. O. Tokiyasu, and R. Yokoyama. *IEEE Trans. Nucl. Sci.*, 68(8):1841, 2021.

[83] Y. Arai, M. Ikeno, S. Iri, T. Sofue, M. Sagara, and M. Ohta. *IEEE Trans. Nucl. Sci.*, 49(3):1164, 2002.

[84] H. Nishino, K. Awai, Y. Hayato, S. Nakayama, K. Okumura, M. Shiozawa, A. Takeda, K. Ishikawa, A. Minegishi, and Y. Arai. *Nucl. Instrum. Methods Phys. Res. A*, 610:710, 2009.

[85] S. Y. Matsumoto *et al. RIKEN Accelerator Progress Report 2021*, 55:10, 2022.

[86] J. G. Johansen *et al. Phys. Rev. C*, 88:044619, 2013.

[87] O.B. Tarasov and D. Bazin. *Nucl. Instrum. Methods Phys. Res. B*, 266:4657, 2008.

[88] J. Raynal. Coupled channel code ECIS97. unpublished.

[89] J. Cook and J. Carr. computer program FOLD. unpublished.

[90] M. A. Franey and W. G. Love. *Phys. Rev. C*, 31:488, 1985.

[91] B. A. Brown and W. D. M. Rae. *Nuclear Data Sheets*, 120:115–118, 2014.

[92] Y. Utsuno and S. Chiba. *Phys. Rev. C*, 83:021301, 2011.

[93] T. N. Taddeucci, R. R. Doering, Aaron Galonsky, and Sam M. Austin. *Phys. Rev. C*, 29:764, 1984.

[94] F. Ajzenberg-Selove. *Nucl. Phys. A*, 506:1, 1990.

[95] R. D. Woods and D. S. Saxon. *Phys. Rev.*, 95:577, 1954.

[96] T. Furumoto, Y. Sakuragi, and Y. Yamamoto. *Phys. Rev. C*, 78:044610, 2008.

[97] T. Furumoto, Y. Sakuragi, and Y. Yamamoto. *Phys. Rev. C*, 80:044614, 2009.

[98] E.-W. Grewe *et al. Phys. Rev. C*, 76:054307, 2007.

[99] P. R. Bevington and D. K. Robinson. *Data Reduction and Error Analysis for the Physical Sciences, 3rd ed.* McGraw-Hill, New York, 2003.

[100] S. Navas *et al.* Review of particle physics. *Phys. Rev. D*, 110:030001, 2024.

[101] K. Miki *et al. Phys. Rev. Lett.*, 108:262503, 2012.

[102] D. J. Horen *et al. Phys. Lett. B*, 99:383, 1981.

[103] P. Vogel, M. Ericson, and J. D. Vergados. *Phys. Lett. B*, 212:259, 1988.

[104] T. Sagawa and T. Uesaka. *Phys. Rev. C*, 94:064325, 2016.

[105] S. Stoica and M. Mirea. *Phys. Rev. C*, 88:037303, 2013.

[106] K. Itahashi and Y. K. Tanaka. Proporsal for RI Beam Factory, Spectroscopy of pionic atoms in $d(^{136}\mathrm{Xe},^{3}\mathrm{He})$ nucelar reactions, 2022.

[107] X. Roca-Maza, H. Sagawa, and G. Colo. *Phys. Rev. C*, 101:014320, Jan 2020.

[108] T. Nish. *Ph.D. thesis*, 2015.

[109] R.K. Carnegie, M.S. Dixit, J. Dubeau, D. Karlen, J.-P. Martin, H. Mes, and K. Sachs. *Nucl. Instrum. Methods Phys. Res. A*, 538:372, 2005.

[110] ROOT TMinuit Class Reference. https://root.cern.ch/doc/master/classtminuit.html.